**University of Bath**

**PHD**

# Theory Of Current-Driven Domain Wall Motion In Artificial Magnetic Domain Structures

Curtis, Ryan

*Award date:*
2015

*Awarding institution:*
University of Bath

Link to publication

## Alternative formats
If you require this document in an alternative format, please contact:
openaccess@bath.ac.uk

Copyright of this thesis rests with the author. Access is subject to the above licence, if given. If no licence is specified above, original content in this thesis is licensed under the terms of the Creative Commons Attribution-NonCommercial 4.0 International (CC BY-NC-ND 4.0) Licence (https://creativecommons.org/licenses/by-nc-nd/4.0/). Any third-party copyright material present remains the property of its respective owner(s) and is licensed under its existing terms.

**Take down policy**
If you consider content within Bath's Research Portal to be in breach of UK law, please contact: openaccess@bath.ac.uk with the details. Your claim will be investigated and, where appropriate, the item will be removed from public view as soon as possible.

Download date: 05. May. 2023

# THEORY OF CURRENT-DRIVEN DOMAIN WALL MOTION IN ARTIFICIAL MAGNETIC DOMAIN STRUCTURES

**Ryan Curtis**

A thesis submitted for the degree of Doctor of Philosophy

University of Bath
Department of Physics

July 2015

**COPYRIGHT**

Attention is drawn to the fact that copyright of this thesis rests with its author. This copy of the thesis has been supplied on the condition that anyone who consults it is understood to recognise that its copyright rests with its author and that no quotation from the thesis and no information derived from it may be published without the prior written consent of the author.

This thesis may be made available for consultation within the University Library and may be photocopied or lent to other libraries for the purposes of consultation with effect from .....

Signed on behalf of the Faculty of Science .....

# Summary

This thesis concerns the combination of two overlapping fields in physics: condensed matter and electromagnetism. Specifically the problem posed of simulating the movement of magnetic domains by applied magnetic, and electric, fields. In this investigation electronic structure methods are used in an attempt to parametrise longer length-scale micromagnetic simulations. Previous works in the field have relied upon suitable experiments having been conducted, whereas this work can stand alone - albeit with its own propagation of systematic errors. Modelling is undertaken to predict the applicability of cobalt platinum multilayers as a new type of computer memory. Although results are promising, features not in the remit of this thesis, such as practicality, are noted to be major obstacles that would need to be overcome. Ab initio methods are used with varying success to predict the saturation magnetisation, Gilbert damping parameter, and anisotropy parameter of cobalt platinum systems.

# Dedication

To my mother.

I wish you were here to see the beautiful family I have. The twins have just started saying names and I imagine the look on your face.

Thank you.

# Declaration

The author wishes to vouch for the authenticity and originality of work not otherwise referenced in this thesis.

# Conference Presentations

Extracts from the chapter entitled *Ab Initio Modelling of Cobalt Platinum Systems* were presented at the Joint European Magnetic Symposia 2012 (JEMS-2012) held in Parma, Italy between 15:45 and 16:00 on Monday 10th September 2012. The presentation was entitled *First-principles calculations for the anisotropy and Gilbert parameter in cobalt systems*. Ryan Curtis and Simon Crampin authored the work, and Ryan Curtis was the presenter.

# Acknowledgements

The author wishes to thank Dr. Simon Crampin and Prof. Simon Bending for supervising me during my time at Bath. He would also like to thank Nigel Wilding for being a very supportive personal tutor during his undergraduate degree, and encouraging him to pursue science.

He must also thank his wife for all of her support while he has been trying to write a thesis at home after work for the last year. He is extemely thankful that his twin boys are strong and healthy, having arrived 2 months early toward the end of his full-time study period. Thomas and Maxwell Curtis have made some additions (typos) in this LaTeX, that is the author's excuse anyway.

# Contents

# List of Figures

# List of Tables

# Chapter 1

# Introduction

## 1.1 Foreword

Spintronics is an up and coming field in physics, as groups investigate the opportunities to use not only the intrinsic charge of an electron, but also its intrinsic *spin* angular momentum. This thesis primarily contains theoretical investigations to aid in the understanding of spintronic systems. Specifically, the motion of a magnetic domain via an applied electric field. These devices are of particular modern interest due to their possible applications in computer hardware. Advances in experimental methods have led to the ability to manufacture devices with specific and defined properties on the nanometre scale.

Magnetism, however, has intrigued for millennia. A formalism only began in the early twentieth century, describing magnetic interactions on the microscopic scale. With the discovery of quantum mechanics came a deeper understanding. Using these new ideas the rudimentary magnetic recording systems developed at the end

of the nineteenth century were improved, and magnetic tape was developed. This in turn opened the door for the audio tape recorder in the mid twentieth century.

Magnets are used in many areas of modern life. Motors in refrigerators, cars, washing machines and tumble driers have changed everybody's lives. Medical science has utilised magnetism in MRI machines, and the tape drive has been modified and redesigned in to the hard drive. However, this technology is nearing its pinnacle, and will soon need replacing - which will be discussed further in section 1.4.

## 1.2 Objectives

## 1.3 Overview of the Thesis

### 1.3.1 Chapter 1

Chapter 1 introduces the thesis. The motivation for the thesis is discussed. Applications of magnetic domains, and artificial magnetic domains in cobalt platinum are introduced.

### 1.3.2 Chapter 2

Chapter 2 discusses the key tenets of magnetism and micromagnetics, first presenting the necessary basics of magnetism. Following this is a demonstration of micromagnetics and its reliance on microscopic and macroscopic length-scale physics. The phenomenology of the Landau-Lifshitz-Gilbert equation is presented, and extensions

of the equation regarding spin-torque terms. Finally, micromagnetic simulation results' reliance on parameters obtained from experiment is discussed.

### 1.3.3 Chapter 3

Chapter 3 introduces the background and theory of electron scale simulations utilised in this thesis. The density functional theory formalism is briefly discussed, and its extension for relativistc effects. Density functional theory implementations in two code packages, ELK and CASTEP, are then described.

### 1.3.4 Chapter 4

Chapter 4 implements the methods discussed in chapter 3. First, methodology for predicting micromagnetic parameters from first-principles is presented/derived, with references to alternative methods and previous works. The methods used are verified and converged for the pure crystalline systems. Using the criterion for convergence as a starting reference, results of calculations for cobalt platinum alloys are presented. Where possible, the methods are then used to predict properties of idealised cobalt platinum multilayer systems. Comparisons are presented between simulated parameters and experimentally obtained values.

### 1.3.5 Chapter 5

Chapter 5 contains the results from micromagnetic simulations for idealised nanowires. Most previous micromagnetic simulations concentrated on in-plane magnetisation materials, this chapter intends to verify the applicability of many key results in the

out-of-plane cobalt platinum systems. Time-of-flight measurements are performed in Hall crosses using extraordinary Hall effect measurements. The effect of device geometry on spin-polarised current flow is investigated, and then the result from this is used to parametrise current-driven domain wall motion (CDDWM) in the Hall cross. Extraordinary Hall effect estimates are discussed, with time-of-flight measurements extrapolated from the performed simulations. Work is then presented on the demonstration of the use of artificial magnetic domains for applications such as racetrack memory.

### 1.3.6 Chapter 6

Chapter 6 concludes this thesis. The overall story of the thesis is analysed, with avenues for future work, alternative methods, and key results discussed.

## 1.4 Applications of Magnetic Domains

### 1.4.1 Hard Disk Drives

Hard disk based devices were initially utilized in 1956 in IBM; the first gadget had a capacity of more than 100 000 characters on each of fifty 60 cm circular platters and were developed from iron oxide and aluminium. The plates exhibited an areal thickness of generally a 600 bits every square centimetre. In 1973 IBM revealed the first 'modern' hard circle drive. The innovation was a minuscule read/wrote head that stayed inside 100 nm of the surface of plate. The density rapidly expanded to 256 kilobits every square centimetre. In 1980 Seagate Storage Technology developed the principle hard disk drive designed for desktop computers utilizing comparable technology. The 5 MB storage capacity limit was paltry by today's standards, and

of the same order of magnitude as the 1956 IBM design. The astonishing idea was fitting the greater part of the innovation into a 5.25 inch structure component fenced in area. Most desktop PCs utilize the 3.5 inch structure element, and limit per layer has expanded to over 3 TB. One straightforward, yet successful, procedure to expand hard drive capacity has been to incorporate two magnetic disks in the drive. With current manufacturing techniques and the miniaturisation of segments this has been conceivable, however the author is uninformed of any arrangements to extend this number. A combination of storage media in a single hard drive also opens up issues with information storage, for example, the documents needing to compass the disk, as the operating system would by and large not have any visibility of the underlying data storage architecture.

Manufacturers are particularly interested in ways to increase the areal memory density of the hard disk drive. The specific aim pertaining to increasing the overall capacity. However this ideally needs to be performed *without* a decrease in read/write accessibility times. The largest areal density today is almost 100 million times greater than the 1950s, and up until 2008 was doubling annually. This trend could not continue, the spinning disks in 3.5 inch drives can only be 3.5 inches, and the areal density approaches its technological limit. The profit margins in old-style hard disk drives have shrunk, driving efforts in research to unearth new storage technologies.

As the capacity has stagnated, demands for speed have escalated. Solid-State-Drives (SSDs) have underlying flash architecture similar to USB and SD card memory. They have no moving parts, so a rotating magnetic disk is not a performance bottleneck. The write speeds are typically 50% more performant than ordinary disks, but read speeds can be quadruple the old values. The new devices are exorbitantly expensive for large densities, although areal densities in the new technology has progressed well in the last few years. From 32 MB to 512 GB in the last 10 years, and a 1 TB version will be available soon. The longevity of these devices is not guaranteed, with many high-speed devices only being available with a one year guarantee of data retention, not applicable to many business requirements. It is also anticipated that, without another major technological breakthrough, the areal

density of SSDs will not surpass the existing technology.

### 1.4.2 Giant Magnetoresistance

The phenomenon first discovered in the late 1980's and used to sense the state of the magnetic disk in a hard drive is giant magnetoresistance (GMR). An example of a multilayer spin-valve system containing two types of ferromagnet is shown in figure 1-1. The schematic attempts to illustrate how a polarisation change of the central 'free' layer can be used to change the resistance, and therefore the current. Figure 1-1 illustrates a ferromagnet with a low coercive field is sandwiched in between two ferromagnets with a high coercive field, separated spacers that are not magnetic. The spacer regions exist to prevent short-range interactions between the alternate ferromagnetic layers. The device is engineered to be in an antiferromagnetic state through magnetostatic interactions. One layer is generally pinned by providing a neighbouring 'bulk' region with parallel magnetisation. Electrons travelling through the material are scattered by the abrupt change in spin dependent band structures. The application of a magnetic field will cause the ferromagnet with the lower coercitivity will more easily align with it. With this layer aligned there will be less scattering, leading to a drop in the resistance of the current perpendicular to the plane. As a sensor, the principle widely used is to detect an external field's presence by observing the corresponding decrease in resistance.

### 1.4.3 Current Driven Domain Wall Motion

If every action has an equal and opposite reaction, then a domain wall affecting the spin-polarised current propagation also means that the converse must also be true, that is, a current can influence a domain wall. True enough [1, 2, 3], magnetic domains can be translated via the application of a spin-polarised current. Although, technically, it is the separation region, the domain wall, that is moved. This effect

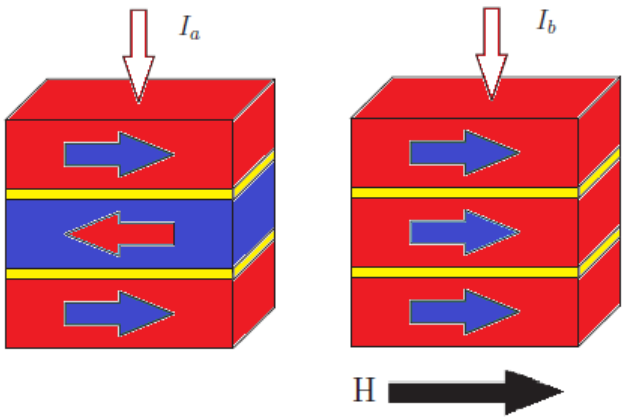


Figure 1-1: The GMR principle. In this simple example there are three ferromagntic layers. A central soft layer sandwiched by two hard layers with a non-magnetic spacer in between. The arrows denote local magnetisation direction, and the colours the material character.

can be used to move a multitude of domains simultaneously. There has been a concentration of efforts in predicting and analysing the resistance of a domain wall [4, 5]. A schematic showing a current in the plane device is shown in figure 1-2. The device differs from a GMR device as the domain wall represents a continuous change in magnetisation, opposed to a discontinuous spacer region. The presence, chirality, and other general characteristics of the domain wall alters resistivity within a local region. Application of an external field, or current, would move the domain wall and eventually remove it. The change in resistance can be identified as the intrinsic contribution, and those from external factors such as anisotropic magnetoresistance [5]. This effect could be used in magnetic sensors to replace GMR.

This thesis, instead of looking at the resistance caused by the domain wall, is concerned with methods of moving the domain walls, and how to measure their positions. This is a different viewpoint to a GMR-like picture, although GMR could still be used in a device exhibiting current-driven motion: to read the domain state. The following section introduces a type of memory that would use the position and polarity of the magnetic domains as a measurable quantity, instead of measurable electrical resistances.

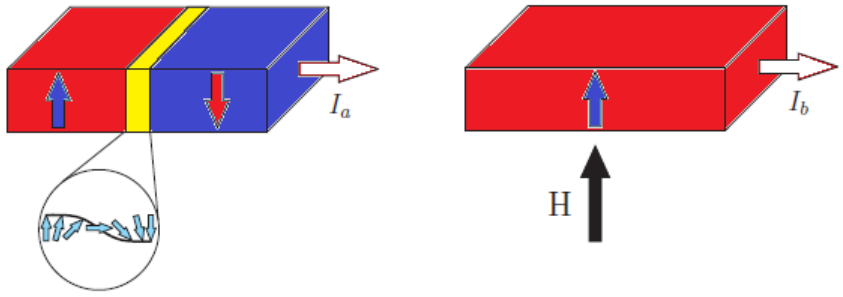


Figure 1-2: Analogous use of domain walls similar to the GMR effect seen in figure 1-1. The left-hand figure shows two opposite polarity domains separated by a single domain wall. The application or presence of a magnetic field perpendicular with a sample will lead to the alignment of all of the moments by moving the domain wall towards the end of the sample. The domain wall disappearing, being absorbed or annihilated directly affects the electrical properties: current through the left-hand figure would be different to that in the right-hand figure.

### 1.4.4 Novel Computer Memory

One group has proposed the idea of magnetic racetrack memory [6], in which the width and size of regions of magnetisation in a ferromagnetic material *are* the information. These domains can then be shifted along by the means of an applied spin-polarised current, an idea first theoretically postulated by Berger in the 1970's [2, 3, 1]. The idea was at first considered a theoretical nicety, but with the realisation of true nanoscale engineering and device manufacturing, there came renewed interest in current-driven domain wall motion (CDDWM).

This new type of computer memory was conceptualised by Stuart Parkin at IBM [6]. It was estimated that using novel device (three-dimensional) patterning methods, devices with the density of current hard-drives ( $\approx 5$ TB) would be able to match the performance of DDR RAM ( $\approx 5$ ns latency). Figure 1-3 is an extract from Parkin's concept paper, and figure **??** shows a comparison table populated by Parkin to compare and contrast it against current technologies. Racetrack memory revolves around the use of current-driven domain wall motion to move, within reason, any type of magnetic domains back-and-forth past read and write heads. The RAM controller would need to be able know how many domains to push along, and which

ones to read and write. The challenges that immediately presented themselves were: how would one ensure domains are of equal size?, how would one know how long to apply a current for?, and, how would one ensure the domains are in their expected location?.

The first proposition for racetrack memory was in Permalloy. This nickel iron alloy, when in a thin film state has in-plane magnetisation. Therefore, patterning small nicks in the sides of any nanowires could be used to hold magnetic domains in position. However, making the domain walls with greater energy barriers to movement would lead to the requirement of stronger currents to move them [7, 8, 6]. The anticipated current required was bordering a magnitude of approximately $3 \times 10^{12}$ A/m$^2$ [4]that could cause the sample to become paramagnetic due to Joule heating - raising the ferromagnet above its Curie temperature.

A simple two-dimensional structure using Permalloy nanowire has been fabricated, and the principle of racetrack memory demonstrated [9]. However, these devices were custom ion milled on substrates (expensive), wider than envisaged (low areal density), and two-dimensional (lower density). The requirement to mill on a substrate in order to make the device reliably makes the three-dimensional geometry envisaged by Parkin intractable. Would some of these problems be alleviated if a change in material was put forward?

Cobalt platinum multilayers could be an answer. The high perpendicular anisotropy [10] means that the domain walls would be narrow, and the magnetisation would only be up or down away from the domain wall. The layers of cobalt could be used independently, as investigations could be performed to understand what structure would be required to decouple the layers. This could make three-dimensional memory devices, will there be a requirement on *volumetric* memory density? The narrow domain walls could also mean that more domains could be put in to the system. Cobalt platinum systems are discussed in the next section, and in Chapters 3 and 4.

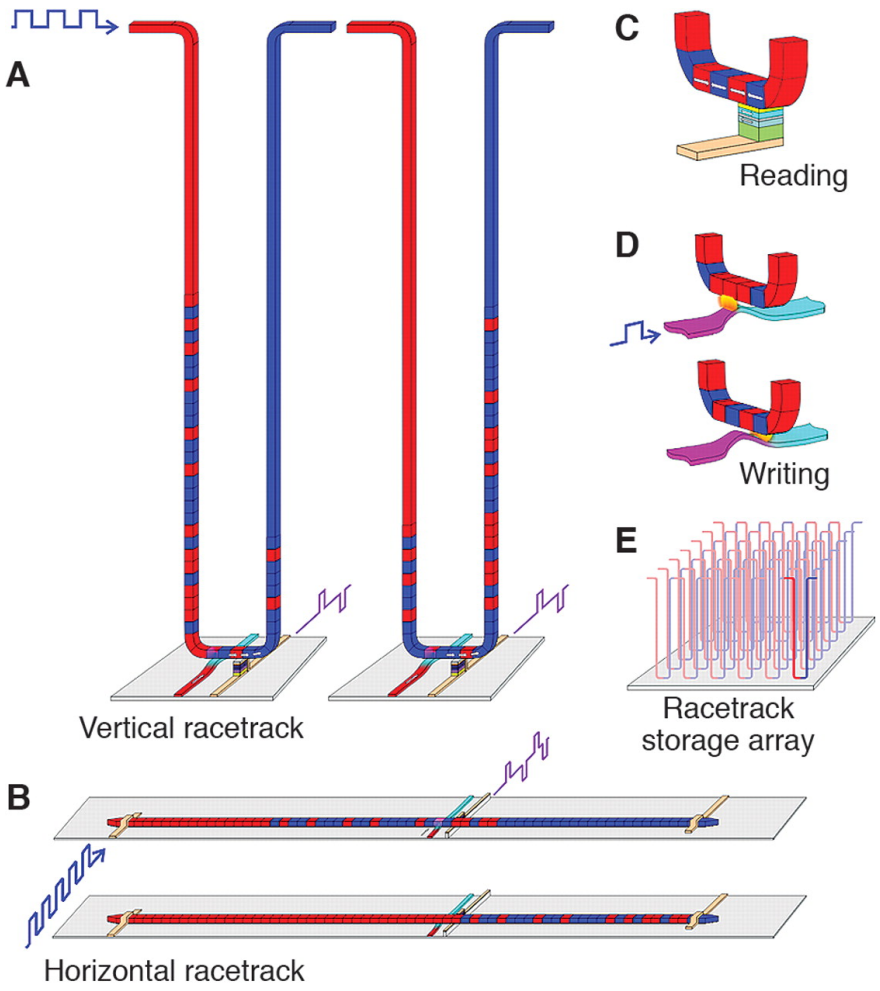


Figure 1-3: Diagram of Parkin *et al.*'s racetrack memory concept. A shows the possible vertical racetrack memory, this 3D memory, if fabricatable, would be a breakthrough with fantastically high areal densities. B shows the 2D form, which Parkin's group reports could have a similar areal density of hard disks but the speed of DRAM. C and D depict the write process using the self-field of an applied current. Reproduced from Parkin [6] as motivation for thesis.

## 1.5 Cobalt Platinum Multilayers

### 1.5.1 Motivation

Cobalt platinum systems have attracted much research interest in the last few years [11, 12, 13, 14]. Thin film, disordered alloys and multilayer systems are all under active investigation. Cobalt has a high Curie temperature, and retains this when alloyed with platinum. Ideal if the application of extremely high current densities will still be a requirement to move domains. The alloys themselves are highly chemically stable, and reasonably simple to manufacture. However, it is the system's large tunable magnetic anisotropy [12] and easily identifiable magneto-optical Kerr effect (MOKE) signal that make them truly interesting candidates for recording material. High anisotropy leads to narrow domain walls. Ordered alloys, disordered alloys, and multilayer cobalt platinum have been studied in the literature extensively [15, 16, 17, 18, 19, 20, 21, 22, 23, 24, 25, 26, 27, 28, 12, 29, 30, 31, 32, 33, 34]. This thesis concerns itself with utilising and extending ab-initio methods to extract structural and magnetic parameters from multilayer systems.

The multilayers can be idealised to be ordered crystals. Platinum is the main component of the multilayer, and thus we would expect the thinner cobalt layers to extend their intraplanar seperation to enable the surfaces to be commensurate. The intraplanar seperation of the platinum layers will broadly not be effected by the cobalt layer, as the lattice constant of elements is difficult to decrease: it would be energetically favourable for the cobalt to mimic the platinum configuration. Platinum's lowest-energy configuration is that of an face-centred-cubic (FCC) crystal, with a lattice constant of 3.92 Å. At surfaces between species and crystal structures there is usually a breaking of symmetry, specifically a surface relaxation. Two cobalt layers sandwiched between platinum crystals would match the intraplanar lattice constant of platinum, but the extraplanar distance between the cobalt layers would expect to be similar to that of bulk FCC cobalt. Further discusses in chapters 3 and 4, surface relaxations lead to interesting effects on the electronic structure.

When considering FCC structures with surfaces, the plane of cleavage needs to be understood. Either the (100) or (111) stacking arrangements are typically studied. The Miller index notation [35] is simply a representation of a plane when the FCC crystal is considered in the simple cubic arrangement. A diagram depicting the configurations can be seen in figure 1-4. Most multilayered systems are created using dc magnetron sputtering. This involves depositing atoms on the surface for a certain time, with experience and measurements forming a feedback loop to be able to design the required device. Experimentalists claim that smooth layers of platinum can be laid with smooth layers of cobalt. For most ab-initio calculations to be undertaken, disorder can be taken in to account by using a large unit cell. This can be extremely computationally expensive. If we assume that the multilayers have been laid in a near-perfect manner, then the structure and other material properties could be analysed using density functional theory. Although a considerable amount of the dynamical work in this thesis is on the trilayer system, many of the concepts can readily be extended to multilayers. Conversely, the multilayer geometry is simpler to simulate in density functional theory, as it uses periodicity in supercells.

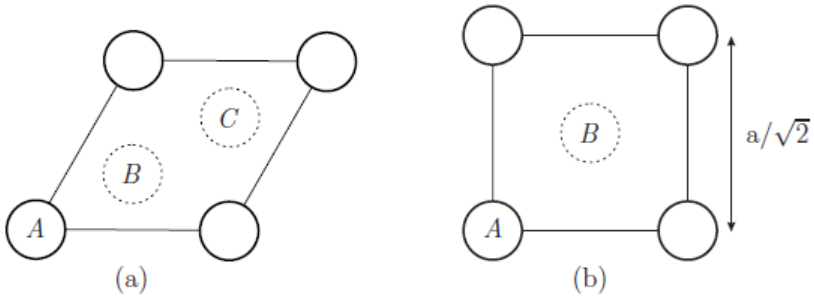


Figure 1-4: Stacking of layers in FCC crystals in the $x, y$ plane, for which the intra-planar lattice is shown in solid lines, and the lattice constant $a$. (a) represents (111) stacking, and (b) illustrates (100) stacking. FCC crystals are typically modelled from a (100) or (111) orientation. The FCC crystal can be entirely rebuilt from the simple diagrams by populating the A, B (and C) lattice sites under the following rules and using the solid lines as intraplanar crystallographic lattice vectors. In (111) stacking the A sites would first be inhabited at $z = 0$, followed by the B site at $z = dz_1$, followed by the C site at $z = 2dz_1$, then A at $z = 3dz_1$, etc. In (100) stacking of FCC layers the A site would be designated first at $z = 0$, and then followed by the B site at $z = dz_2$, and then A at $z = dz_2$ etc. Note that the interplanar distance in the two stacking arrangements is not consistent.

Other groups have decided to use disordered alloys of cobalt and platinum to con-

duct experiments. A larger MOKE signal is reported [36] to be present in the disordered alloys. However, ensuring locality of magnetic domains is not as straightforward, and computationally more difficult to model in many regimes.

### 1.5.2 Artificial Magnetic Domains

Artificial magnetic domains are, in the following work, real magnetic domains. They are termed artificial as their location and nucleation points are atypical, i.e. not random. A magnetic domain in perfect material would be metastable equilibrium, preferring no particular location over another. By making a small region of a nanowire narrower the chance of a domain wall being at the change is higher than other locations. Systemic properties of the magnet can also be changed locally to create the desired effect. Researchers have bombarded the magnetic samples with gallium ions in order to reduce the anisotropy, making an energy barrier between the irradiated and non-irradiated sections [37, 4, 5, 38]. This energy barrier is a likely place to collect domain walls, to which other experiments can be conducted upon. That is, the lower anisotropy region will typically be softer than the higher anisotropy region. This means that more energy is required to change the polarisation of the higher anisotropy region. This provides experimentalists a method of ensuring the locality of magnetic domains. The entire sample is first magnetised to saturation. Enough energy can then be provided to switch the magnetisation in the lower anisotropy region. This ensures that the regions would have differing polarities, ensuring the existence of some type of magnetic domain wall. The use of artificial magnetic domains makes racetrack memory all the more feasible. Controlling the position of magnetic domain walls and their velocities will be important for the technological development of racetrack memory and similar domain wall based devices.

# Chapter 2

# Micromagnetics: Background, Phenomenology, and Parameterisation

## 2.1 Introduction

A range of magnetic materials exhibit current-driven domain wall motion (CD-DWM). The original investigations by Berger [39, 40, 41, 1, 2, 3] exhibited the effect in multilayer structures. Parkin *et. al.*[6] utilised permalloy (Py) - a nickel-iron alloy of which thin films have no magnetocrystalline anisotropy. In Py nanowires they have demonstrated the translation of magnetic domains via current densities in excess of $1 \times 10^{12}$ A/m$^2$ [6].

In order to understand the operation of this memory a suitable theoretical basis should be laid. Micromagnetics is a theory that combines quantum effects and classical mechanics in to a continuum model. An introduction to micromagnetics, its

energy representations, and its use for modelling magnetic domains is explored. In this chapter the Landau Lifshitz Gilbert equation is presented. Further discussions include extensions to the original equation representing spin-polarised currents and applicability to current-driven domain wall motion.

## 2.2 Magnetism

In this section the basics of magnetism relative to the content of this thesis will be described. The relationship between atomic magnetic moments and the macroscopic magnetisation behaviour of materials provides the physical background required to interpret the discussion presented in subsequent chapters. Firstly, the electronic contributions to the total atomic magnetic moment are described. Following on from this an understanding of ferromagnetism is gained through a discussion of the exchange interaction which includes a description of Heisenberg theory and Stoner band theory.

### 2.2.1 Definition and Units

Readers unfamiliar with the field of magnetism might not be aware of the complications involved with results often being presented in differing units sets. This section exists to aid in disambiguation.

The magnetic induction vector, $\mathbf{B}$, by definition can be written as combination of the magnetic field and magnetisation:

$$\mathbf{B} = \mu_0 \left( \mathbf{H} + \mathbf{M} \right) . \tag{2.1}$$

In this equation $\mu_0$ is a universal physical constant, the "permeability of free space" [35]; being identified in the literature as equal to $4\pi \times 10^{-7}$ henry/m in S.I. units, and **M** is the volume magnetisation within the sample. The magnetic response of a material to an applied field **H** causes $\mathbf{B}/\mu_0$ to differ from **H** inside the material. The magnetic induction vector is a field that includes both the external field and the material response, ergo **H**, the applied field, is the cause and **M**, the magnetisation, is the material effectThe **B** field is used for the magnetic field when microscopic currents contribute to the flux density, specifically for situations in which the contribution of the magnetisation is important.

It should be noted that when presenting comparisons to older and/or experimental prior published works it is difficult to avoid the alternate units. The units of key properties in both systems of measurements are presented in Table 2.1.

| Quantity | Symbol | S.I. | C.G.S. |
|---|---|---|---|
| Field | $H$ | A/m | oersteds |
| Magnetisation | $M$ | A/m | emu/cm$^3$ |
| Induction | $B$ | tesla | gauss |
| Moment | $\mu_m$ | Am$^2$ | emu |
| Field equation | - | $B = \mu_0 (H + M)$ | $B = H + 4\pi M$ |

Table 2.1: Principal S.I. and C.G.S. units currently used in magnetism and within this thesis. Conversion factors between the two systems are defined within the text in the section on Definition and Units.

All equations and relations presented in this thesis will generally be given in S.I. units. However, the literature extensively uses measurements in the C.G.S. system, so the relations between the two unit systems are briefly compared here. The conversion factors between the unit systems are as following:

$$1 \text{ oersted} = (1000/4\pi) \text{ A/m} = 79.58 \text{ A/m (2.d.p)}$$
$$1 \text{ gauss} = 10^{-4} \text{ tesla}$$
$$1 \text{ emu/cm}^3 = 1000 \text{ A/m}$$
$$1 \text{ emu} = 10^{-3} \text{ Am}^2$$

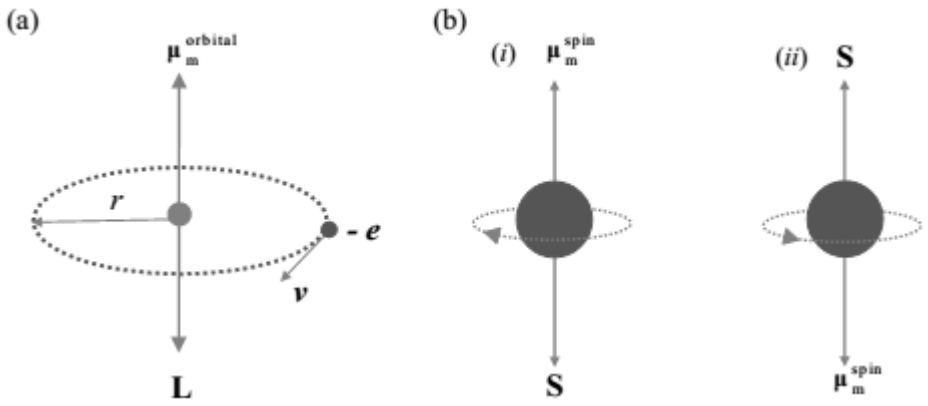


Figure 2-1: Visualisation of the two kinds of magnetic moments associated with an electron in an atom. Figure adapted from [42]. (a) orbital motion about the nucleus gives rise to an orbital magnetic moment with associated angular momentum, **L**. (b) spin of the electron about its own axis resulting in a spin magnetic moment with associated angular momentum, **S**. The spin of the electron is limited to two directions only (i) clockwise and (ii) counter-clockwise allowing the electron can be visualised as a bar magnet.

### 2.2.2 Magnetic Moments in Atoms

Magnetic dipole moments exhibited in mass matter emerge from the precise energy connected with the movement of electrons as depicted in 2-1. Whilst the core displays an magnetic moment it is roughly 1000 times less than the electron's moment and can therefore be ignored when evaluating the total magnetic moment[35]

### 2.2.3 Ferromagnetic Exchange

#### Introduction

The exchange interaction is the effect that differentiates between ferromagnetic and paramagnetic atoms and solid. In this context, the exchange interaction is the

energy which is related to the arrangement of spins within individual or coordinated atoms. Electron spins in an incomplete orbital generally align parallel so as to reduce the exchange energy within the atom, as predicated by Pauli's exclusion principle. This exchange contribution is also minimised between coordinating atoms when the spin are in a parallel arrangement.

Two models are commonly utilised in order to provide an insight in to ferromagnetic materials. Heisenberg postulated local moments [43]. Enlightening contributions to band theory were documented by Slater and Stoner in an array of seminal papers [44, 45, 46, 47, 48, 49]The main premise of the local moment theory was that quantity of ground state unfilled electron orbitals would influence the mangetic moment. Conversely, the band theory model suggested itinerancy, that the electrons were a crystal property rather than an atomic property. Band theories branched in to other forms such as the Friedel model [50], which samples components from both local moment and Stoner band theory. Physically, it seems that neither extreme is correct. Electrons in the 3d transition metals that exhibit ferromagnetism in particular are neither atomic in form or fully itinerant in form. The exchange energy will be further discussed as it is a major energetic component in the process of domain formation [51]

**Orbital Moment Suppression**

The 3d electrons culpable for the demonstrated magnetic moment are subject to influence by the crystal field. For clarity, the crystal field is that is introduced by the presence of the coordinated atoms and their cohesive electronic structureTypically, the orbital moment is fully suppressed by the crystal field. [35]Note that even with the suppression of the orbital momenta that the quantum mechanical spin-orbit interaction leads spin momenta and orbital momenta being coupled, and thus a change in the spin can lead to an effect on the effective orbital momentumResulting from the magnetic field that the electron 'perceives' as it moves about the nu-

cleus, the spin orbit interaction is the coupling of a $H$-field with the electron's spinFundamentally, the motion of the electron is directly dependent and coupled with the magnetic moment through the spin orbit interaction. It is worth noting that when there are approximately balanced spin directions in a material the spin-orbit coupling is negligible, as the system is non-magnetic. The quantum mechanical spin-orbit interaction is critical in systems like ferromagnets with differing electron spin populations[35].

### Field Theory

In 1906 Weiss developed molecular field theory [52, 53]. An overview, analysis, or introduction to the exchange interaction would be incomplete without the primary effort to understand spontaneous magnetisation. Firstly, it is worth noting that the theory is not quantum mechanical in nature, and that therefore is unable to fully explain exchange phenomena.

A field $H_{molecular}$, the molecular field, was understood to exist that would lead to the parallel spin moment arrangement of atomic dipoles that were not paired. Below a critical temperature, it was predicted that an intrinsic molecular field could be the cause of the spontaneous magnetisation. The field's intensity, however, was assumed to be inversely dependent on temperature. Therefore, as the temperature rose to the Curie temperature, $T_c$, the kinetic energy associated with the increased temperature would break the alignment. Mathematical analyses deriving an estimate of the Weiss field were deduced by performing a comparison of the dipole energetics with the thermal energetics. A formulated equation reads:

$$k_B T_c = \mu_B H_{molecular} \tag{2.2}$$

where the Boltzmann constant $k_B$, the Bohr magneton $\mu_B$ are the standard physical constants. Iron has an approximate Curie temperature of one thousand Kelvin. The above equation can then be simply used to estimate the magnitude of the molecular field in this circumstance: $10^7$ Oersteds. Note that this value is higher than the

fields that are used in most experiments. This field is also three orders of magnitude larger than that which would be obtained via dipole-dipole interactions. Therefore, a key finding of molecular field theory was that magnetisation must be contributed to by more than interacting dipoles. The nature of the molecular field was not elucidated within the discussion[52, 53]. Research by Weiss in molecular field theory was the first to theorise the potential of small regions with similar magnetisation, the foundation of domain theory. A seminal paper produced by Lev Landau and Evgeny Lifshitz in 1935 [**?** ] corroborated the theory of magnetic domains and led to research such as this thesis today.

### Heisenberg Theory

Heisenberg [43] demonstrated that the origin of the exchange interaction that underpins ferromagnetism is quantum mechanical. The proof considered that the parallel configuration of spins of electrons of coordinating atoms can actually be lead to a lower energy configuration than the typical antiparallel configuration. This was a rigorous proof that explained the predictions made by Weiss with his field theory. Critically, the origin and explanation of the exchange interaction is purely quantum mechanical with no explicable analogue in classical physics. Further discussions of the exchange interaction can be found in the following sources by Aharoni, Hubert and O'Handley [54, 55, 56]. Presently in this thesis a qualitative discussion of exchange is presented and followed by its implementation in Stoner's Band Theory.

$H_2$ can be simply regarded as a two proton, two electron system with each electron orbiting its respective proton. Electron A(B) with proton A(B) will exhibit attraction. The electrons and protons, A and B, will also exhibit repulsion between themselves. As the electrons have considerable freedom in their positional status one would expect electrons to stay further apart. A fundamental requirement of electrons in quantum mechanics is that they are indistinguishable. Particularly, the effect of the *exchange* of electron and proton labels should be quantified - the exchange interaction. The Pauli exclusion principle must be adhered to, and thus

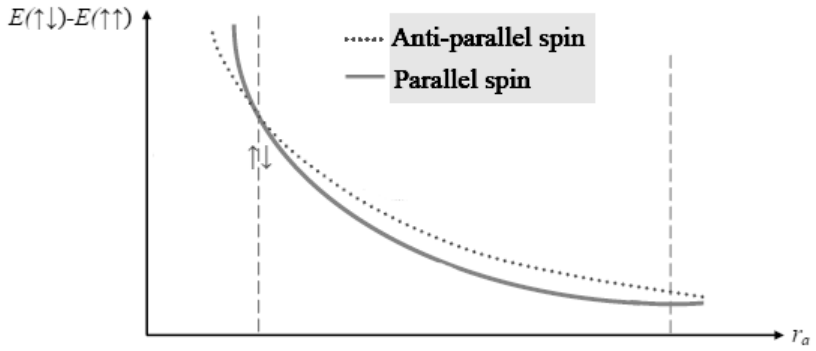


Figure 2-2: This graph shows the typical relationship between the exchange energy for parallel (anti-parallel) spin configurations and the interatomic separation $r_a$. When the interatomic spacing decreases the orbitals overlap, forcing the spins to inhabit the same spatial coordinates. Consequently, the Pauli exclusion principle states that the spins should align anti-parallel. Adapted from [51].

a schematic of the exchange energy can be seen in figure 2-2. Simply, the exchange energy can be quantified through the change in energy associated with the different parallel and antiparallel configurations of the spin.

Anti-bonding is the when electrons are spatially separate but have the same wave-function. In this instance it is favourable for the spins to align parallel. Forming a crystalline structure usually decreases the distance between the atoms, which means that system's that exhibit favourable antibonding will could have spatial overlap. However, within the exclusion principle the electrons could not have the same spin and location. This means that to decrease the distance and minimise the global energy a spin flip would be required. Note that as the distance between atoms is increased, the Coulombic interaction would decay by the distance squared. Thus the parallel and antiparallel configurations of start to become minute with increasing distance. So, technically the exchange energy is quantum mechanical in origin, the Coulombic classical force is augmented through the spin configurations.

### Stoner Band Theory

Heisenberg theory assumed the electrons involved in ferromagnetism are not itinerant. When considering the ferromagnetic transition metals it is easy to interpret that the conduction electrons would not be entirely localised. When considering the electronic structure of crystals band theory is popular. The development of this theory was undertaken in 1933-1936 by Slater and Stoner [44, 45, 46, 47, 48, 49]. The original aims of the work was to find an explanation how there could values of the number of Bohr magnetons in ferromagnetic systems that were not whole numbers.

The main premise of band theory is that the overlap of spatial wavefunctions of the individual orbitals leads to range of allowable energies, instead of one allowable energy - and energy band. That is to say that when a specific number of atoms are bonded in to a crystal a specific number of levels must be split from the levels of the individual atom. Therefore, within a system of relatively few atoms a continuous range starts to form. The 3d and 4s electrons have similar energies and are conduction electrons within the 3d ferromagnets. When constructing a crystal from the ferromagnet's atoms it is the highest energy electrons that form the bands, of which there is a schematic detailing the filling and exchange in figure 2-3.

An assumption often used when discussing the prior principles that the band shape is not consistent across all elements. By studying the shapes of the energy bands in figure 2-3 an understanding of exchange in band theory should be visible. The 3d band has a maximum occupancy of ten electrons due to quantum numbers and therefore has a high density of electrons. Note that the 3d band is rarely full within the 3d transition metals and in some cases the 4s states has a lower energy, thanks to its much lower orbital momentum. The 4s band due to its much lower orbital momentum is preferentially screened over the 3d electrons. Compared to the 3d band in the ferromagnet, the 4s band is much wider with a low electron density - only a maximum of two electrons can inhabit the band.

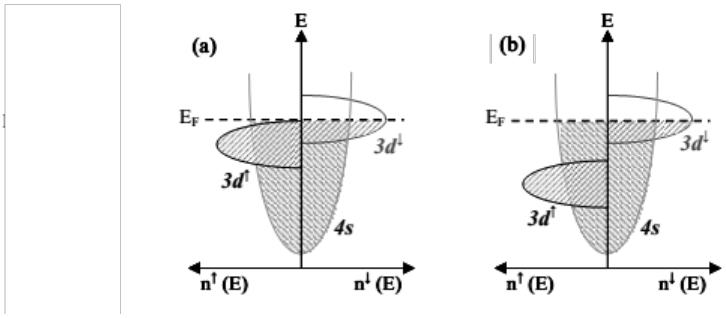


Figure 2-3: The density levels in the 3d and 4s bands for, (a) with exchange splitting, and (b) with large exchange splitting in the 3d energy band. Exchange splitting means that the spins will preferentially align parallel prior to filling the antiparallel channel. The Fermi level is defined typically as the highest occupied state in the valence band at zero temperature and separates filled electronic states from vacant electronic states at zero temperature.

### 2.2.4 Magnetic Domains

#### Introduction

Weiss postulated that in order for molecular field theory to be applicable to experimental observations, there had to be ferromagnetic domains [52, 53]. The existence of many small regions in the ferromagnet would allow for the formation of the demagnetised state. He suggested that in each individual magnetic domain the magnitude of the magnetisation would be constant, a saturation value. Further to this, the direction vectors adjacent to each other would sum to zero. This was conjecture in attempt to explain experiments, but actually turns out to be extremely accurate based on our current understanding of ferromagnetic domains. However, no explanation as to why domains form, or why they exhibit behaviour such as hysteresis was provided.

### Experimental Evidence

The first credible experiments in to the process of magnetising a sample were conducted by Barkhausen [57]. By attaching a loudspeaker and amplifier to the sample that was being magnetised, audible domain changes were heard, termed Barkhausen jumps. This is usually considered to be the first experiment observing and explaining domain switching [58]. Further investigations by suggested that the jumps are caused by the movement domains of opposing magnetisation - domain walls [59].

Almost concurrently, other experimental work was being conducted on crystals and their magnetisation. Extremely noteworthy experimental work was conducted by Honda and Kaya in 1926 [60, 61]. They were the first group to determine that the magnetisation has preferred cystallographic directions: the discovery of magnetocrystalline anisotropy. This discovery was observered by overlaying magnetisation loops for magnetic fields applied of differing directions, and observing the magnetisation response. It was also discovered that mechanical stress and deformation affected the magnetocrystalline anisotropy direction. These experiments form the foundations of much research in magnetic anisotropy. Finally, it is worth recording that these properties were not predicted by Weiss' magnetic field theory - they are material dependent.

Nowadays, the existence or presence of magnetic domains is typically measured using the magneto-optic Kerr effect (MOKE)[62, 63, 27, 64, 65]. Only certain magnetic materials can be used to view the Kerr rotation of laser light caused by the orientation of a magnetic domain. In material samples where it is not straightforward to use MOKE, devices can be patterned that look like Hall bars. Time of flight measurements can be undertaken, the signal changes that are considered to be a trace of a moving magnetic domain between two Hall contacts can be recorded.

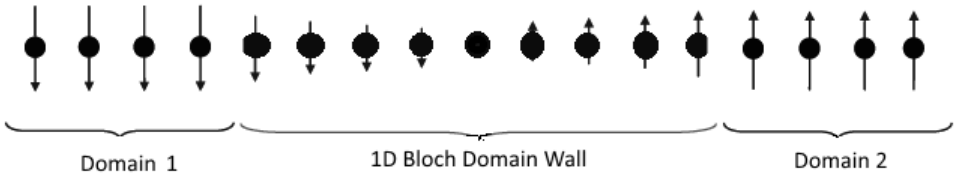


Figure 2-4: Schematic of a domain wall separating two distinct magnetic domains. The spin at the middle of the domain wall represents pointing out of the plane of the page.

**Micromagnetics**

A key tenet of micromagnetics is that the magnitude of the magnetisation is fixed in a material. The direction changes in order to minimise the total energy: the internal magnetic structure of a disk rearranges into a vortex to alleviate the cost of creating opposing magnetic surface poles (see figure (2-7)). Regions of differing magnetisation are called *domains*, and the transition itself is termed a *domain wall*, and is not abrupt. Furthermore, there are many types of domain walls, and the exact nature is dependent on the material's properties and geometry. Controlling the sizes and types of domain wall in ferromagnetic materials is essential to realising novel spintronic devices.

## 2.3 Energetics

The following sections describe the energetics of micromagnetic systems. Theories from different length scales, quantum and macroscopic, are applied to the micromagnetic regime to derive equations for energy densities.

### 2.3.1 Exchange

The exchange interaction is the basic effect which leads to magnetic ordering in ferromagnetism, and is quantum mechanical in origin. To examine this contribution it is essential to revisit the work of Heisenberg, and write the Pauli exclusion principle of two electrons at arbitrary coordinates $(\mathbf{r}_A, \mathbf{r}_B)$:

$$\Psi(\mathbf{r}_A, \mathbf{r}_B) = -\Psi(\mathbf{r}_B, \mathbf{r}_A)\,, \tag{2.3}$$

as the wavefunction is antisymmetric under exchange. But, in addition, the total wavefunction of the electron can be assumed to be composed of a spin wavefunction, and a spatial one. Therefore if the spatial wavefunction is symmetric then due to the Pauli exclusion principle it follows that the spin wavefunction consequently is antisymmetric, and this distinct coupling is the origin of the exchange interaction. The simplest derivation for the exchange energy can be found from considering a 2 electron system with electrons at $\mathbf{r}_A$ and $\mathbf{r}_B$ [66]. Combinatorial arrangements of the individual states $\psi_a$ and $\psi_b$ can be determined to be the singlet and triplet states:

$$\Psi_S = \frac{1}{\sqrt{2}}[\psi_a(\mathbf{r}_A)\psi_b(\mathbf{r}_B) + \psi_a(\mathbf{r}_B)\psi_b(\mathbf{r}_A)]\phi_S \tag{2.4}$$

$$\Psi_T = \frac{1}{\sqrt{2}}[\psi_a(\mathbf{r}_A)\psi_b(\mathbf{r}_B) - \psi_a(\mathbf{r}_B)\psi_b(\mathbf{r}_A)]\phi_T\,, \tag{2.5}$$

where $\phi$ denotes the (normalised) spin part of the wavefunction. The energies of each state are

$$W_S = \int \Psi_S^* \hat{H} \Psi_S \,\mathrm{d}\mathbf{r}_1\,\mathrm{d}\mathbf{r}_2 \tag{2.6}$$

$$W_T = \int \Psi_T^* \hat{H} \Psi_T \,\mathrm{d}\mathbf{r}_1\,\mathrm{d}\mathbf{r}_2\,, \tag{2.7}$$

where the Hamiltonian $\hat{H}$ encapsulates the interrelationship between the two electrons. A further deduction of the singlet and triplet states quantifies the difference in energy between the two and can be written

$$W_S - W_T = 2\int \psi_a^*(\mathbf{r}_1)\psi_b^*(\mathbf{r}_2)\hat{H}\psi_a(\mathbf{r}_2)\psi_b(\mathbf{r}_1)\,\mathrm{d}\mathbf{r}_1\,\mathrm{d}\mathbf{r}_2\,. \tag{2.8}$$

The eigenstates of the singlet and triplet states lead to the relations $\mathbf{S}_1 \,.\, \mathbf{S}_2 = -3/4$ and $\mathbf{S}_1 \,.\, \mathbf{S}_2 = 1/4$ respectively [35]. Hence an effective Hamiltonian can be written

$$\hat{H} = \frac{1}{4}(W_S + 3W_T) - (W_S - W_T)\mathbf{S}_1 \,.\, \mathbf{S}_2 \,, \tag{2.9}$$

a sum of a constant and a spin-dependent term. The Hamiltonian's spin term can finally be written as

$$\hat{H}_{spin} = -J\mathbf{S}_1 \,.\, \mathbf{S}_2 \,, \tag{2.10}$$

where $J$ is the exchange integral defined by

$$J = W_S - W_T = 2 \int \psi_a^*(\mathbf{r}_1)\psi_b^*(\mathbf{r}_2)\hat{H}\psi_a(\mathbf{r}_2)\psi_b(\mathbf{r}_1)\, \mathrm{d}\mathbf{r}_1\, \mathrm{d}\mathbf{r}_2 \,. \tag{2.11}$$

A method for generalising this equation to a many-bodied system was suggested by Heisenberg, leading to the Heisenberg model:

$$\hat{H} = -\sum_{i>j} J_{ij}\mathbf{S}_i \,.\, \mathbf{S}_j \,, \tag{2.12}$$

where $i > j$ eliminates double-counting, and the exchange integral is spin dependent, but is often approximated as a constant. From this we can deduce a necessary condition for magnetic ordering in a ferromagnet, that if the corresponding spins are aligned then the exchange integral must be positive. Due to the straightforward nature of this nearest neighbour interaction, this type of exchange interaction is called direct exchange. It will be the only one covered in this thesis, as other exchanges such as the RKKY interaction are typically prevalent in rare-earth metals. In cobalt, nickel, and iron, the direct exchange interaction can be viewed as interactions between the $d$ orbitals (those with angular momentum quantum number $l = 2$). These orbitals are highly localised, so the theoretical approximation of nearest neighbour interactions is usually implemented.

The Heisenberg model as it stands is not entirely useful for micromagnetics, as it intrinsically is discrete in nature. The continuum approximation is used to transform the problem into one of magnetisation. In this model the exchange interaction is assumed to be only a nearest neighbour phenomenon, and the spins are considered classically with the angle between nearest neighbours defined as $\phi_{ij}$. Further to

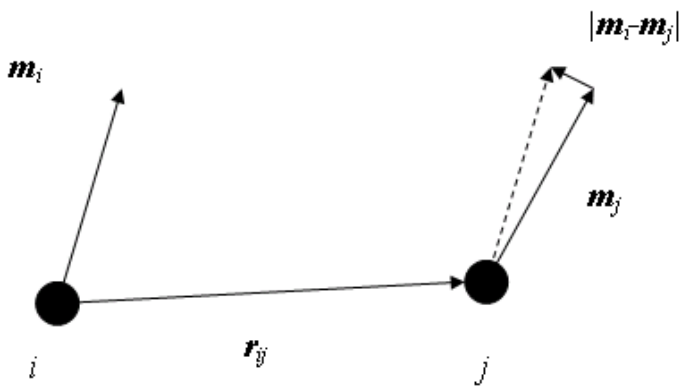


Figure 2-5: Representation of magnetic moments by reduced moments in the continuum approximation.

this, the angles between each neigbouring spin is assumed to be small, so that the small angle approximation can be used [35]. The energy, after Heisenberg [67], is

$$W = -JS^2 \sum_{<ij>} \cos\phi_{ij} = -\text{constant} + \frac{JS^2}{2} \sum_{<ij>} \phi_{ij}^2 \,, \tag{2.13}$$

where the constant can be neglected as it is the energy of the fully aligned state. The magnetisation unit vector $m$ can be used to approximate the spins at lattice points $\mathbf{r}_{ij}$. Using the notation of figure 2-5:

$$|\phi_{ij}| \approx |\mathbf{m}_i - \mathbf{m}_j| \approx |(\mathbf{r}_{ij} . \nabla)\mathbf{m}| \,, \tag{2.14}$$

leading to the energy to be represented as

$$W = JS^2 \sum_{<ij>} \left((\mathbf{r}_{ij} . \nabla)\mathbf{m}\right)^2 \,. \tag{2.15}$$

In the continuum limit the sum will become an integral as the discreteness of the lattice is ignored, yielding [68]

$$W = A \int_V [(\nabla m_x)^2 + (\nabla m_y)^2 + (\nabla m_z)^2] \mathrm{d}^3 r \,, \tag{2.16}$$

. Here $z$ is the coordination number and $a$ is the nearest neighbour distance. In addition, A is the *exchange stiffness*, defined by $A = 2JS^2 z/a$. The energy equa-

tions will usually be in the form of a density. The micromagnetic exchange energy density is thus:

$$E = A[(\nabla m_x)^2 + (\nabla m_y)^2 + (\nabla m_z)^2]\,. \tag{2.17}$$

### 2.3.2 Anisotropy

Magnetocrystalline anisotropy is the intrinsic preference of the magnetisation of a ferromagnet to point along one its easy axes. For the 3d ferromagnets these are standard crystallographic directions, e.g. for HCP cobalt the easy axis is <0001> [35]. This anisotropy can be deduced from first principles [69], but is usually determined experimentally, and characterised by the anisotropy constants $K_n$. To find the resulting anisotropy energy, one could align the magnetisation along a direction, and calculate the energy difference to that of another.

Iron and Nickel in the FCC phase exhibit cubic magnetocrystalline anisotropy. In terms of directional cosines $\alpha_i$, the cubic anisotropy can be written [56]:

$$E_K = K_1\left(\alpha_1^2\alpha_2^2 + \alpha_2^2\alpha_3^2 + \alpha_3^2\alpha_1^2\right) + K_2\alpha_1^2\alpha_2^2\alpha_3^2 + K_3\left(\alpha_1^2\alpha_2^2 + \alpha_2^2\alpha_3^2 + \alpha_3^2\alpha_1^2\right) + \ldots\,. \tag{2.18}$$

Directional cosines are used to quantify the directional difference between the magnetisation and the easy axes of the material, and the anisotropy constants determine the amplitude of the energy cost.

Any material that has a single preferred axis of magnetism has uniaxial anisotropy [35]. Examples in nature are HCP Cobalt, in which the anisotropy axis points perpendicularly to the (111) plane. Other systems that exhibit this kind of behaviour are thin films, in which the breaking of the crystal symmetry perpendicular to the surface leads to it becoming the preferred magnetisation axis. Considering the imagined system in which $\theta$ defined as the angle between the axes or easy magnetisation vector and magnetic response in the material (the magnetisation), then the associated energy will be at a minimum for $\theta = 0°$ and 180°, and at a maximal

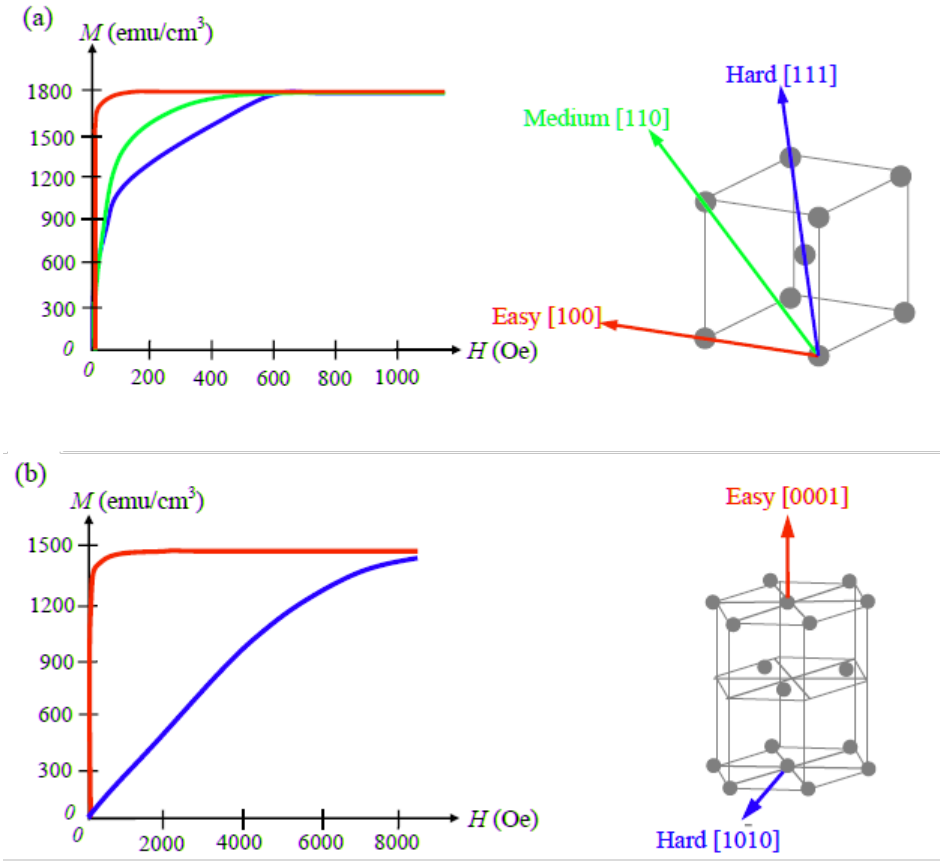


Figure 2-6: Summary of magnetocrystalline anisotropies seen in iron, cobalt, and nickel. The magnetisation curves are for (a) BCC iron, (b) FCC nickel, and (c) HCO cobalt. After [51].

value for 90° and 270°. The energy, in the terms of a Taylor expansion, could be written out in a series in terms of powers in $\sin^2\theta$, yielding [56]:

$$E_K = K_1 \sin^2\theta + K_2 \sin^4\theta + K_3 \sin^6\theta + \ldots \tag{2.19}$$

$K_n$ are termed the anisotropy constants. The constants decay rapidly with increasing $n$, and terms higher than $n = 2$ are usually negligible in uniaxial materials - and hence a reliable value is not attainable. This is not generally the case in cubic anisotropy materials, where the second-order constant can often be 10% of the first constant and of an alternate direction [70]. Therefore, most work on uniaxially anisotropic systems is undertaken with only the first anisotropy constant, and hence is, as a standard, termed $K$ in the literature.

Uniaxial anisotropy can arise from other sources, not just the crystal structure and material. Thin films can exhibit this type of anisotropy, due to the magnetisation reorienting in order to minimise the energy lost via the production of stray fields due to surface poles. The stacking of layers such as in CoPt [69] can also lead to uniaxial anisotropy in a material. In some systems, the shape anisotropy and the magnetocrystalline anisotropy can be of similar orders of magnitude, leading to interesting domain structures.

### 2.3.3 Zeeman Interaction

The magnetisation also interacts with externally applied magnetic fields. It attempts to align to the applied field, or, mathematically under an applied field $\mathbf{H}_{app}$

$$E_{app} = -\mu_0 \mathbf{M} \,.\, \mathbf{H}_{app} \,. \tag{2.20}$$

### 2.3.4 Magnetostatics and Demagnetising Fields

By definition, the magnetostatic (magnetic analogue to electrostatic) energy is the related to the *demagnetising field*. This is the field generated by the sample that neutralises the effects of changes in the magnetisation. From this, it can be viewed as an energy term that tries to minimise the amount of surface poles in a magnetic material, leading to effects such as shape anisotropy. It is a dipole-dipole interaction, and is the main reason for formation of domain walls in a magnet, and can be seen pictorially in figure 2-7. The origin of the demagnetising field can be visualised by considering an uniformly magnetised sample. Said material will be finite, and thus have magnetic poles on its end cleave planes, and consequently due to the the magnetisation being a material response these must be sources and sinks of the magnetisation. The magnetic flux density in a sample is the sum of the magnetic field and the magnetisation of a sample. If we consider a case in which there is zero

applied magnetic field, a ferromagnet (at least locally) is magnetised. Starting from the definition of the magnetic flux density [35]

$$\mathbf{B} = \mu_0(\mathbf{H} + \mathbf{M})\,, \tag{2.21}$$

and taking the divergence of both sides yields, from Maxwell's equation $\nabla \,.\, \mathbf{B} = 0$

$$\nabla \,.\, \mathbf{H} = -\nabla \,.\, \mathbf{M}\,. \tag{2.22}$$

And thus the nonzero divergence of the magnetisation at the surface will lead to the generation of another field, the *demagnetising field*, which from now will be written $\mathbf{H}_D$, shown in figure 2-8.

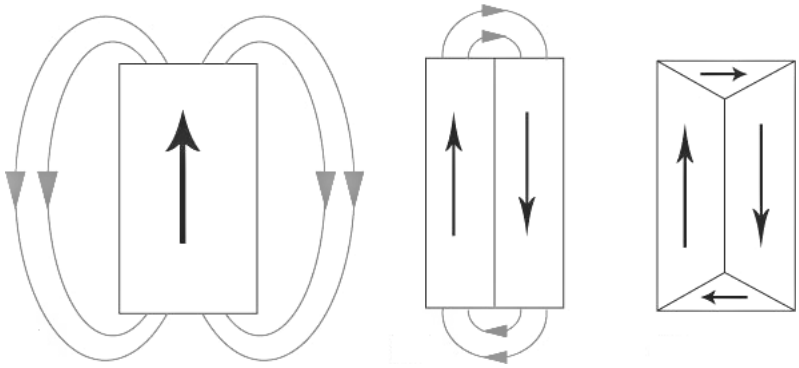

Figure 2-7: How minimisation of the magnetostatic energy leads to the formation of domain walls in magnets.

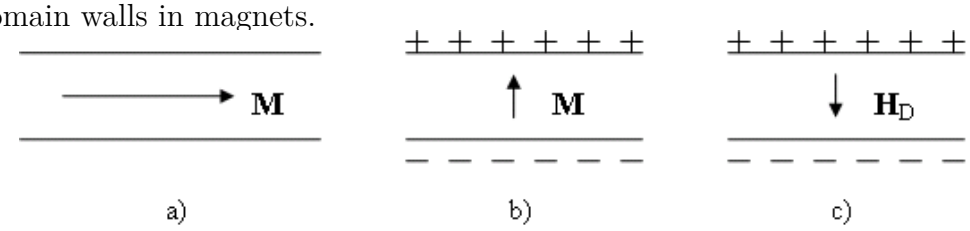


Figure 2-8: The origin of the demagnetising field due to surface poles. a) shows how magnetisation aligned parallel to a surface minimises the field. b) and c) depict how magnetisation perpendicular to a surface gives rise to a non-zero divergence and hence a demagnetising field.

The energy density of the demagnetising field, $E_D$, is [54]

$$E_D = \frac{\mu_0}{2}\mathbf{H}_D^2\,. \tag{2.23}$$

As $\mu_0 \mathbf{H}_D = \mathbf{B}_D - \mu_0 \mathbf{M}$, the energy density can be written as

$$E_D = -\frac{\mu_0}{2} \mathbf{M} \,.\, \mathbf{H}_D \,, \tag{2.24}$$

where this comes from the fact that $\mathbf{B}_D \,.\, \mathbf{H}_D = 0$.

However, to find the demagnetising field, a scalar magnetic potential of the form

$$\mathbf{H}_D = -\nabla \phi_D \tag{2.25}$$

is considered, which is deduced from Maxwell's equation $\nabla \times \mathbf{H} = 0$. Continuing from equation (2.22), in the ferromagnet

$$\nabla^2 \phi_D = \nabla \,.\, \mathbf{M} \,, \tag{2.26}$$

and outside

$$\nabla^2 \phi_D = 0 \,. \tag{2.27}$$

These equations are solved to the boundary conditions that the potential is continuous, and so is the difference between the normal gradients with respect to the magnetisation on the surface, or

$$\phi_D^{in} = \phi_D^{out} \;\text{ and }\; \frac{\partial \phi_D^{in}}{\partial \mathbf{n}} - \frac{\partial \phi_D^{out}}{\partial \mathbf{n}} = \mathbf{M} \,.\, \mathbf{n} \,. \tag{2.28}$$

This nonlocal term is extremely complicated to solve for all but the simplest of ideal geometries. Generally, this term is solved computationally via a finite difference method solver (FDM) [71], or a finite element solver (FEM). The FDM method is simpler to program, but can struggle with difficult boundary conditions. However, the FEM can be more suitable in some geometries as it does not have to concern itself with anything nonmagnetic outside of the geometry of the sample.

### 2.3.5 Summary

A summary of the energy contributions to micromagetic systems is shown in figure 2-9. For the total energy density to be reduced it is more-often-than-not energetically favourable to have at least one magnetic domain wall.

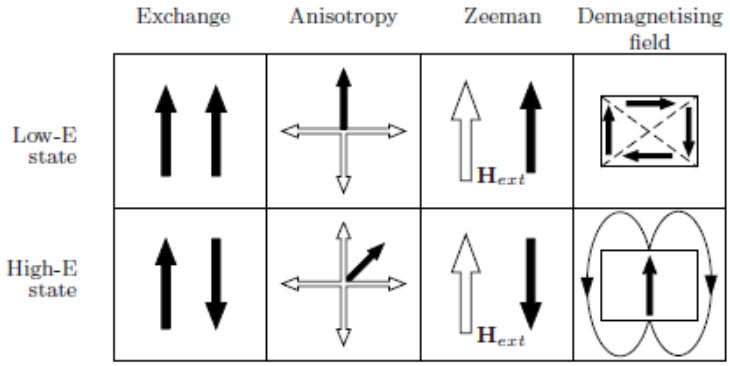


Figure 2-9: Summary of the energetics of magnetic domains and the difference between the high and low energy states.

## 2.4 Domain Walls

It is the competition of all of the terms that have been discussed that lead to domain wall formation [72]. Exchange attempts to keep the magnetisations pointing in the same direction, contracting a domain wall. Anisotropy wants to retain a uniform magnetisation along the easy axis, minimising the number of domain walls in a sample. The demagnetising field will attempt to make the number of domains the highest possible, in order to reduce the magnetostatic energy associated with surface poles.

The regions separating the domains (domain walls) come in many flavours. Bloch, Néel, and vortex walls are illustrated in figure 2-10. Bloch and Néel walls are

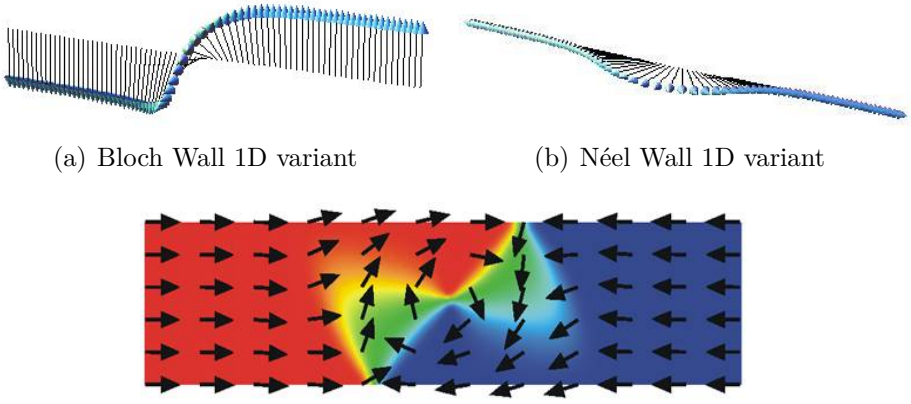

(a) Bloch Wall 1D variant

(b) Néel Wall 1D variant

(c) Vortex Wall 2D example

Figure 2-10: Types of one and two dimensional domain walls. (a) and (b) are classed as one-dimensional domain walls, and (c) is a two-dimensional wall. Bloch walls are usually seen in thin films with high perpendicular magnetic anisotropy.

examples of one-dimensional domain walls. This is because only one dimension is required to view the domain wall. Bloch walls usually form in thin films with high perpendicular anisotropy. Néel walls form in permalloy as the shape anisotropy keeps the magnetisation in-plane. The energy differences between vortex and Néel walls in permalloy is small, but vortex walls are spatially much larger. This is another consideration for the use of permalloy in racetrack memory, the size and type of domain should not be unknown. In addition to the uncertainty as to the domain wall character in permalloy, the chirality is also of interest. The vortex in the 2D plane could either be clockwise or anticlockwise, leading to either an out-of-plane moment at the mathematical singularity inhabiting the centre of the vortex. The direction of this moment can reveal the chirality. A positive use for vortices in the memory might be to prevent annihilation of certain domain walls. Walls of opposite chirality will attract as they seek to align and minimise the exchange contribution, with potential applications in domain wall logic gates [73].

The energy equations presented and be combined and minimised using variational calculation. Combining the energy terms gives a formula for the total energy density

in a uniaxial micromagnet with no applied fields

$$E = E_{ex} + E_K = \frac{A}{M_s^2} \left(\nabla \mathbf{M}\right)^2 + K \sin^2 \theta \,. \tag{2.29}$$

A computational solver, such as OOMMF (the Object-Oriented MicroMagnetic Framework) [74], can be employed to minimise the above energy equation in order to find the equilibrium magnetic state. A word of caution for using a package to derive lowest energy states: for most geometries one has to be careful of the initial magnetisation configuration provided to the solver. This is because the initial configuration can lead the magnetisation evolving into local minima, rather than the global minimum. This effect can be reduced by choosing different seeds for random initial magnetisation, and inputting approximately expected solutions, allowing the system to converge. After this the final energies of the solutions can be compared.

### 1D Domain Walls

In a 1D model with no boundaries it is simple to deduce the structure of a 1D domain wall - imagine an infinite nanowire. The equations are somewhat simplified if a polar coordinate reference frame is adopted. The standard coordinate frame used in micromagnetics is shown in figure 2-11. Utilising the geometry of the problem, assume $\mathbf{M} = \mathbf{M}(x)$ [75]. In the new coordinate frame and with the prior assumption the magnetisation is often transcribed to [75]

$$\mathbf{M} = M_s(\sin\theta\cos\phi\,\mathbf{i} + \sin\theta\sin\phi\,\mathbf{j} + \cos\theta\,\mathbf{k})\,. \tag{2.30}$$

Depicted in figure 2-11 and denoted $\theta$ and $\phi$ in the above equation are angles that define the coordinate system. The energy density in this new coordinate frame now reads

$$E = A\theta'^2 + A\phi'^2 \sin^2\theta + K\sin^2\theta\,, \tag{2.31}$$

where there are no applied fields, and $'$ denotes the spatial $x$-derivative.

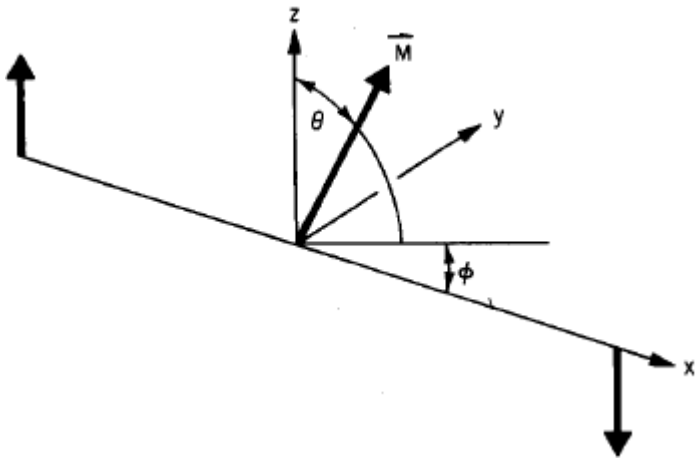


Figure 2-11: Polar coordinate frame used for modelling the domain wall.

The Euler-Lagrange equation minimises the free energy. In its standard form in micromagnetics it is

$$\frac{1}{\mu_0}\frac{\delta E}{\delta \mathbf{M}} = \mathbf{H}_{eff} = 0\,, \tag{2.32}$$

where $\frac{\delta E}{\delta \chi}$ is the functional derivative, defined by $\frac{\delta E}{\delta \chi} = \frac{\partial E}{\partial \chi} - \nabla.\frac{\partial E}{\partial \nabla \chi}$. This equation minimises the effective field $\mathbf{H}_{eff}$ in the entire system, within and without the magnet. It is referred to as the sum of all of the fields acting on the sample and within the sample.

For the stationary state in the 1D model with no applied fields the Euler-Lagrange equations become

$$\frac{\delta E}{\delta \theta} = \frac{\delta E}{\delta \phi} = 0\,. \tag{2.33}$$

This formulation yields the following two equations for intraplaner and extraplanar magnetisation angles:

$$2A\frac{\partial^2 \theta}{\partial x^2} - \sin(2\theta)\left(A(\phi')^2 + K\right) = 0 \text{ and} \tag{2.34}$$

$$\sin^2\theta\phi'' + \sin(2\theta)\theta'\phi' = 0\,. \tag{2.35}$$

1

[1]Note that no temporal fluctuations have been considered, a method for including time's arrow can be undertaken by examining the LLG equation in the following section with the above energy

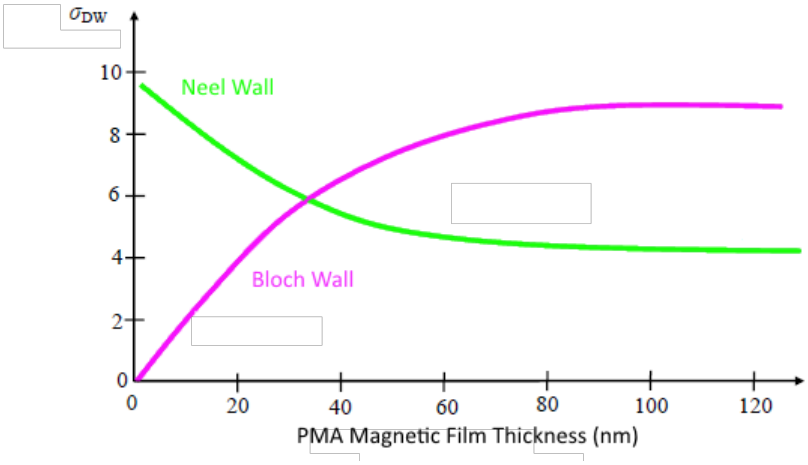


Figure 2-12: Areal energy density versus film thickness of Bloch and Néel walls in a shape anisotropy dominated permalloy thin film. Adapted from [51].

Th difference in energy from the Bloch wall configuration versus the Néel wall configuration for a single domain wall is shown in figure 2-13. The effect of shape anisotropy should be clear from the graph. It is not until the sample starts approaching a micron in width that the Neel wall state becomes possible. The shape anisotropy, $K_D$, can be approximated by

$$K_D = \frac{1}{2}\mu_0 M_s^2 \,. \tag{2.36}$$

However, as the film becomes much wider the Néel state becomes more favourable. This is because $K_D >> K$, the shape anisotropy is much greater than the magnetocrystalline anisotropy. A comparison of Bloch and Néel wall energy density in permalloy is shown in figure 2-12.

A solution for these equations that satisfies the conditions $\theta(x \to \infty) = \pi$ and $\theta(x \to \infty) = 0$ is:

$$\phi(x) = \phi_0 = \text{constant} \;\text{ and }\; \theta(x) = \pm 2 \arctan\left(\exp\left(\frac{x}{\Delta_0}\right)\right) , \tag{2.37}$$

density and finding an equation that states that $\frac{\partial\theta}{\partial t} = 0$, for all time in the region of a domain wall.

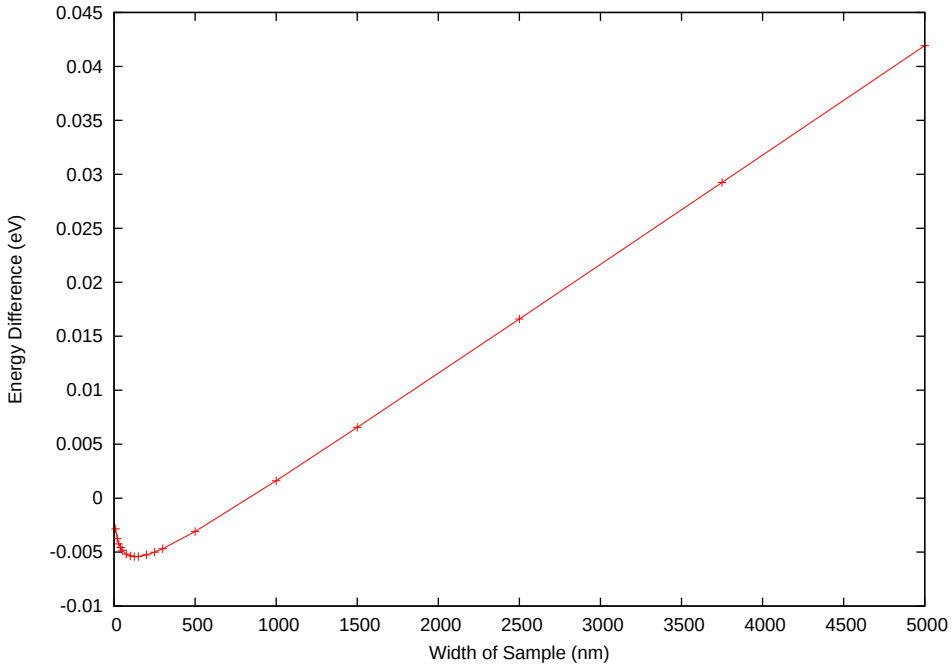


Figure 2-13: The energy comparison between the standard one dimensions wall in nanowires: Bloch and Neel wall states in a thin film with material constants similar to that of cobalt platinum multilayer. The length and thickness of the film are 1 $\mu$m and 0.3 nm respectively, and the width was varied in order to produce the plot. $A = 3 \times 10^{-11}$ Jm$^{-1}$, $K = 8 \times 10^{5}$ Jm$^{-3}$ and $M_s = 8 \times 10^{5}$ Am$^{-1}$.

where $\Delta_0 = \sqrt{(\frac{A}{K})}$ is defined as the domain wall width parameter, illustrated in figure 2-14. This derivation implies that the domain wall should be static and that the width of the wall should be independent of the saturation magnetisation. If $\phi_0 = 0$ then the wall is termed a Néel wall, as the magnetisation transforms in the plane of the magnetisation, or if $\phi_0 = \pi/2$, it is called a Bloch wall. The wall profiles can be studied in figure 2-10. Using the solution for the profile (2.37) and energy density (2.31) allows the domain wall energy density to be found in the 1D model. Using $\mathrm{d}x = \sqrt{A/K}\mathrm{d}\theta/\sin\theta$, and the invariance of $\phi$ yields:

$$\begin{aligned} \sigma_{DW} = \int_{-\infty}^{\infty} E \,\mathrm{d}x = \int_{-\infty}^{\infty} A\theta'^2 + K\sin^2\theta \,\mathrm{d}x = \\ 2\int_{-\infty}^{\infty} K\sin^2\theta \,\mathrm{d}x = 2\sqrt{AK}\int_{0}^{\pi} \sin\theta \mathrm{d}\theta = 4\sqrt{AK}\,. \end{aligned} \tag{2.38}$$

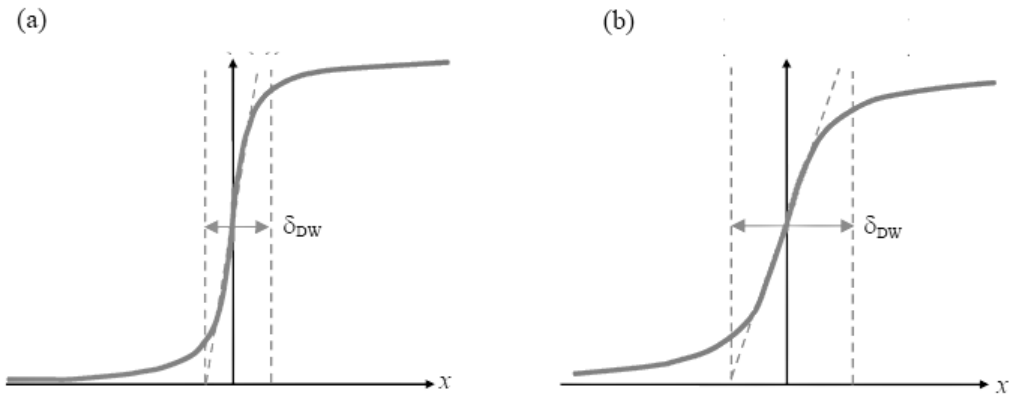


Figure 2-14: Schematic of the domain wall width parameter, defined as the distance mapped out in the x-axis for a gradient taken from the centre of the domain wall profile. (a) shows the effect of large anisotropy, and (b) small anisotropy on the width of the domain wall. The definition is the same as that used by Lilley. After [51].

A summary of investigations in to the shape of 1D domain walls is shown in figure 2-15. The results were obtained using OOMMF and obtained for finite geometries. The domain wall width parameters, $\delta_{DW}$, are consistent to within 0.06%, 6.12 nm versus 6.12372 nm. In order to obtain the width parameter from simulations a domain wall form of

$$\theta = 2 \arctan \exp \left( \frac{x - x_0}{\delta_{DW}} \right) , \tag{2.39}$$

where $x_0$ and $\delta_{DW}$ are fitting parameters to the computation. The energy minimisation routine finds a Bloch wall with properties extremely close to those predicted by the 1D model, and will generate this from a range of 2 domain states.

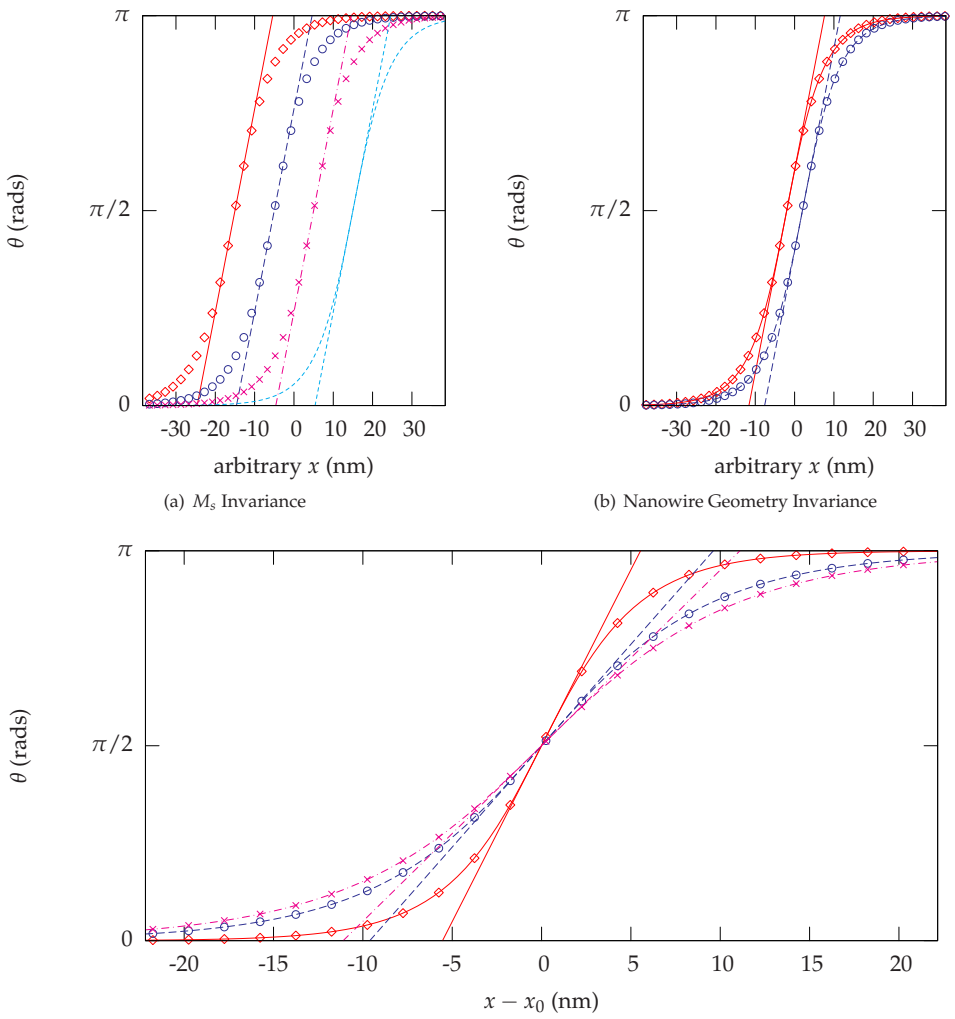


(a) $M_s$ Invariance

(b) Nanowire Geometry Invariance

(c) Exhange and Uniaxial Anisotropy Parameter Dependence

Figure 2-15: (a) The magnetisation angle as a function of position for nanowires of geometry 1000 x 100 x 0.3 nm, with uniaxial anisotropy constant $K = 8 \times 10^5$ Jm$^{-3}$, exchange parameter $A = 3 \times 10^{-11}$ Jm$^{-1}$, mesh size 5 x 5 x 0.3 nm and saturation magnetisation $M_s = 4 \times 10^5$ Am$^{-1}$ (red), $M_s = 6 \times 10^5$ Am$^{-1}$ (dark blue), $M_s = 8 \times 10^5$ Am$^{-1}$ (pink), and the 1D model prediction (light blue). The domain wall centres are offset, and only a subset of OOMMF data is represented for clarity. All simulations produce a value for the width parameter of 6.12 nm, compared to the 1D value of 6.12372 nm. (b) The applicability of the 1D model for nanowire geometries of 1000 x 20 x 0.3 nm (red) and 1000 x 200 x 0.3 nm (blue), both taken at mesh sizes of 5 nm and with anisotropy constant $K = 8 \times 10^5$ Jm$^{-3}$, exchange parameter $A = 3 \times 10^{-11}$ Jm$^{-1}$ and saturation magnetisation $M_s = 8 \times 10^5$ Am$^{-1}$. (c) How the domain wall width scales with the value of the exchange parameter and uniaxial anisotropy constant at values of $K = 8 \times 10^5$ Jm$^{-3}$, $A = 1 \times 10^{-11}$ Jm$^{-1}$ (red) $K = 8 \times 10^5$ Jm$^{-3}$ $A = 3 \times 10^{-11}$ Jm$^{-1}$ (blue) and $K = 6 \times 10^5$ Jm$^{-3}$ $A = 3 \times 10^{-11}$ Jm$^{-1}$ (pink). The three cases gave width parameters of 3.53 nm, 6.12 nm and 7.07 nm respectively, comparing to 1D model predictions of 3.53553 nm, 6.12372 nm and 7.07107 nm.

## 2.5 The Landau-Lifshitz Gilbert Equation

### 2.5.1 Origin and Conception

Micromagnetic simulations are performed in order to predict magnetic ordering, or confirm the configurations found in experiment. The simulations start from some initial state such as a single domain wall, or a random configuration is often used, which is done to simulate the cooling of a ferromagnet from above its Curie temperature. The equation that is solved is the Landau-Lifshitz-Gilbert (LLG) equation (which is a reformulation of the Landau-Lifshitz equation [76] by Gilbert [77] in the 50s to incorporate the large damping effect on the magnetisation in some ferromagnets)

$$\frac{\partial \mathbf{m}}{\partial t} = -\gamma \mathbf{m} \times \mathbf{H}_{eff} + \alpha \mathbf{m} \times \frac{\partial \mathbf{m}}{\partial t} \,. \tag{2.40}$$

$\mathbf{H}_{eff}$ is again the effective field, the sum of the fields due to anisotropy, exchange, demagnetising and externally applied fields. The LLG equation can be phenomenologically derived by considering the consequence of the effective field acting on the magnetisation. The angular momentum associated with the magnetisation will give rise to gyroscopic reaction, mathematically,

$$\frac{\partial \mathbf{m}}{\partial t} = -\gamma \mathbf{m} \times \mathbf{H}_{eff} \,. \tag{2.41}$$

In this equation $g$ is the Landé factor approximately 2 but is an extrinsic propery, and $\gamma = \dfrac{\mu_0 g e}{2 m_e}$ is the gyromagnetic ratio. This equation phenomenologically describes the precession of the magnetisation about the effective magnetic field The precession would be infinite if not for the inclusion of damping terms. A schematic illustrating the precession and damping of the magnetisation about the effective field is shown in figure 2-16. Loss can originate from a number of sources within a ferromagnet. There are intrinsic losses such as lattice defects and the diffusion of them. There are also macroscopic losses like eddy currents. Gilbert reformulated the Landau Lifshitz equation to include intrinsic damping via the phenomenological damping parameter $\alpha$ [77]. This term is essential as it stops infinite precession

and will align the magnetisation to the effective field, and is valid even for large damping. In real materials the damping parameter takes positive values less than 0.01.

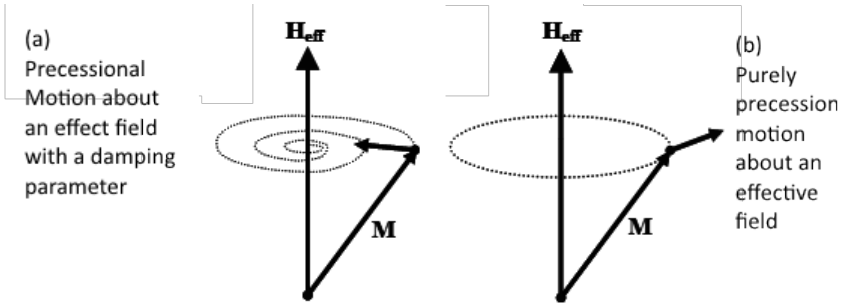


Figure 2-16: Precessional motion of the magnetisation about an effective field governed by the material properties and the local magnetisation. (a) shows the precessional torque, and (b) shows the effect of a damping torque on the precessional motion.

## 2.6 Spin Polarised Currents & CDDWM

### 2.6.1 Background

In a ferromagnet such as cobalt spin-dependent properties are expected to exist. The Fermi velocity is an example, as well as the density of states about the Fermi energyÂn applied current in a standard metal will be transported by spin up and down electrons arranged in a parallel manner. In a ferromagnet the magnetic moments of the electrons would prefer to be aligned as close as possible to the magnetisation - minimising spin transfer torque (STT). This in turn leads to an imbalance in the current carrying electrons, which can be visualised by considering separate spin channels. This difference is termed the polarisation, $P$, often formulated in terms of the occupancy, $n$. In this case a potentially arbitrary parameter that is spin dependent:

$$P = \frac{n_\uparrow - n_\downarrow}{n_\uparrow + n_\downarrow}\,. \tag{2.42}$$

Materials which are not magnetic exhibit zero polarisation, whereas for ferromagnets it will generally be non-zero. The highest measured polarisations have been found in $CrO_2$ (98%) [78], but these measurements are not perfect as they are only conducted on surfaces; to date, no bulk method of experimentally measuring the polarisation of spin currents is possible. The Fermi energy density of states for the magnet is often used as a quantity for determining the polarisation of the material. However, the electrons in a ferromagnet are not all of the same character, with often several electron state bands crossing the Fermi energy, so this simplistic treatment for determining the polarisation is not always valid.

Two approaches for looking at spin polarised currents and domain walls can be found in the literature [79]. One looks at the effect of the presence of a domain wall on an applied current, and the other considers the effect of a spin polarised current on a domain wallÐomain wall resistance is not the focus of this report (although an interesting phenomenon), and so the second problem will be investigated.

The first definitive study of CDDWM was in the 80s by Berger *et al* [1, 2, 3]. Current densities of $10^{11}$ $Am^{-2}$ were found to translate the wallsIt was confirmed that the motion was entirely due to the motion of the electrons, and not the Oersted fields created by the high currents, or any other experimental artefacts. Further to this, the magnetic domains were found to always move in the direction of electron transport. By definition, the domain walls travelled in the opposite direction to the applied current. This suggested the idea of spin-transfer-torque (STT), as every action must have an equal and opposite reaction. The next significant development when Buhrman *et al.* discovered magnetisation reversal due to spin currents [80] in magnetic multilayer structures. This was the first firm confirmation of Slonczewski's concept of STT [81, 82]. The switching was imagined to be due to the spin from one ferromagnetic layer that must relax to match the that of the next layer. The change in direction of the electron leads to a change in angular momentum. In turn, this leads to a torque on the angular momentum of the electrons bound to the lattice being generated by the applied current. The torque can be written as:

$$|\mathbf{T}| = \frac{\hbar P_J J}{e}\,, \tag{2.43}$$

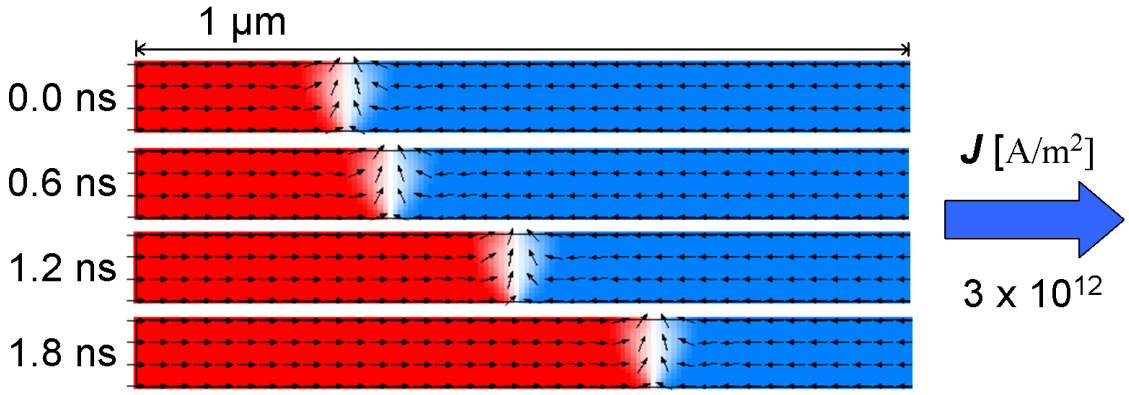


Figure 2-17: Current driven domain wall motion in a perfect Py 5000 x 160 x 8 $nm^3$ nanowire simulated using an OOMMF extension written by IBM labs researchers. Conducted using the material parameters, A = 1.3 x $10^{-11}$ $Jm^{-1}$, $M_s$ = 8 x $10^5$ $Am^{-1}$, with no specified anisotropy direction.

where $P_J$ is the polarisation of the spin current $J$. This torque needs to be sufficiently large in order to dominate over the forces retaining the magnetisation's direction. If this is the case then the magnetisation will rotate to a direction in line with the electron flow (opposite to the current). From this analysis it is transparent that the ferromagnet's spins are the crux of the phenomenon. Even though the previous idea was concerned with different layers with magnetisations of opposite orientation, it is not difficult to stretch this idea to applying a spin-polarised current to a domain wall. Therefore, it can be inferred that a torque will be generated by the spin-polarised electrons crossing the domain wall. At even larger current densities, groups have discovered an effect of domain motion coined as spin pressure. This effect is not directly related to STT as there appears to be no transfer of angular momentum from the carriers to the lattice electrons [79]. The pressure comes from the transference of linear momentum - the electrons being back-scattered by the domain wall. Nonetheless, wall motion driven by STT is the focus here. Initial experiments on STT at the beginning of this renaissance were primarily conducted on permalloy of differing Ni Fe concentrations . This material was used as it was easier to induce wall motion as there is no intrinsic anisotropy in the thin films, only that due to the stray fields - shape anisotropy.

The effect of spin-polarised current on a domain wall will now be analysed. The interaction between the 4s electrons and the 3d electrons can be written as an interaction potential4s and 3d electrons are considered as these are the conduction electrons and localised electrons giving rise to ferromagnetism in cobalt, nickel and iron. The potential acting on a 4s electron due to the 3d electrons is [79]

$$V(x) = g\mu_B(\mathbf{S}\,.\,\mathbf{H}_A(x) + H_A/2)\,, \tag{2.44}$$

where $x$ is the coordinate normal to that of the plane which contains the wall. Here

$$\mathbf{H}_A = \frac{-2J_{sd} < \mathbf{S}(x) >}{g\mu_B} \tag{2.45}$$

is the s-d exchange field and $J_{sd}$ is the relevant exchange integral. Adding $H_A/2$ ensures that the potential vanishes at infinity. Betwixt a domain wall the potential will lead to a force on the magnetic moment of the 4s electron:

$$F_x = -g\mu_B\mathbf{S}\,.\,\frac{\mathrm{d}\mathbf{H}_A}{\mathrm{dx}} = -g\mu_B S_y H_A \frac{\mathrm{d}\theta}{\mathrm{dx}}\,. \tag{2.46}$$

Here the angle $\theta = \theta(x)$ is the direction of $\mathbf{H}_A$. The spins will precess about the exchange field. The adiabatic approximation is the assumption that $\theta(x)$ is much greater than the angle between the spin and the exchange field. The force on the domain wall is then written as

$$F_x = -\frac{\hbar^2 v_x^2}{4g\mu_B H_A}\frac{\mathrm{d}}{\mathrm{d}x}\left(\frac{\mathrm{d}\theta}{\mathrm{d}x}\right)^2\,, \tag{2.47}$$

where $v_x$ is the velocity of the electron when not in the vicinity of the wall. This work should be valid for domain walls whose profile change over a reasonably large distance (>30nm) in order for the adiabatic approximation to be as accurate as possible.

### 2.6.2 Extending the LLG Equation

Slonczewski was the first to attempt to reformulate the LLG equations to include terms to represent STT in magnetic multilayers [81]. He formulated an equation for the torque due to the current $I$ on spins 1 and 2, with unit vectors $\hat{\mathbf{S}}_i$ in their corresponding layer:

$$\frac{\partial \mathbf{S}_i}{\partial t} = \frac{gI}{e}\hat{\mathbf{S}}_i \times \left(\hat{\mathbf{S}}_1 \times \hat{\mathbf{S}}_2\right) , \tag{2.48}$$

with $i = 1, 2$ denoting the spin in each layer. This term describes a torque that is directly proportional to the current flow, whose polarity is modified if the electron flow is turned about. Here $g$ is not the Lande g-factor, but a factor with angular and polarisation dependence. This, in turn, captures more physics. The steady state solution of this system was solved for an applied current [81].

Li and Zhang [83] derived an equation for the STT which has been heavily cited in recent years, and implemented into some micromagnetic solvers. They wrote for the torque

$$\tau = -\frac{b_J}{M_s^2}\mathbf{M} \times \left(\mathbf{M} \times (\hat{\mathbf{J}}_e \,.\nabla)\mathbf{M}\right) . \tag{2.49}$$

Here $\hat{\mathbf{J}}_e$ is the directional unit vector of unitary magnitude of the applied current charge density, with $b$, a velocity vector given by:

$$b_J = \frac{PJ_e\mu_B}{eM_s} . \tag{2.50}$$

They assumed an equation of this form by deriving their own equation for spin torque, and rewriting it in the same form as Slonczewski's. The spin torque was claimed to be the reaction torque on the magnetisation due to the spatial variation of the spin current density,

$$\boldsymbol{\text{ø}}_b = \frac{\partial \mathbf{j}_x(x,t)}{\partial x} = b_J\frac{\partial \mathbf{M}}{\partial x} , \tag{2.51}$$

where $b_J$ is the same as above.

Equation (2.49) was derived to be remarkably similar to the Slonczewski-derived one, but written in terms more obvious from a micromagnetic point of view. Using (2.49) in simulations of a head-to-head [2] Néel wall in Py an initial velocity $-b$ (with applied current density greater than critical) was found, but subsequently the wall slowed down. This was found to be due to the perpendicular magnetisation temporally increasing, implying increased damping which in turn retards the wall motion. Of paramount importance from the simulations was the result that an applied spin-polarised current appears to only move a wall a finite distance, proportional to the velocity over the Gilbert damping constant, for a period of time not usually lasting more than a ns. The relationship between the analytical solutions of the LLG equation in 1D are discussed in section 5.3. This discussion includes a presentation of the perfect nanowire analytically solution, explicitly showing the inverse dependence of the domain wall motion on the phenomenological damping parameter. This motion appears almost the exact opposite of domain wall motion under an applied field, where a wall accelerates and tends to a terminal velocity [81, 84].

Li & Zhang extended their analysis from adiabatic to adiabatic and *non*-adiabatic torques [85]. The initial idea was to compare the spin-flip lifetime $t_{SF}$ to the exchange lifetime $t_A = \hbar/SJ_A$

$$\xi = \frac{t_A}{t_{SF}}\,. \tag{2.52}$$

From this an additional modification to the LLG was derived:

$$\frac{\partial \mathbf{M}}{\partial t} = -\gamma \mathbf{M} \times \mathbf{H}_{eff} + \frac{\alpha}{M_s}\mathbf{M} \times \frac{\partial \mathbf{M}}{\partial t} - \frac{b_J}{M_s^2}\mathbf{M} \times \left(\mathbf{M} \times \frac{\partial \mathbf{M}}{\partial x}\right) - \frac{c_J}{M_s}\mathbf{M} \times \frac{\partial \mathbf{M}}{\partial x}\,. \tag{2.53}$$

In this equation the current is applied in the $x$ direction, and $b_J$ and $c_J$ are velocities,

[2] In shape anisotropy dominated nanowires Néel walls can be of the form head to head (imagine arrow heads representing the domains as shown in the figure) or tail to tail. As it would be inferred, the terminology arises by imagining the magnetisation as an arrow. If the $x < 0$ $\mathbf{m} = (1, 0, 0)$ and for $x > 0$ $\mathbf{m} = (-1, 0, 0)$ then the wall would be termed head-to-head. This is because the drawn arrows would have the (arrow-) heads touching, as opposed to their tails.

given by

$$\begin{aligned} b_J &= \frac{PJ_e\mu_B}{eM_s\left(1+\xi^2\right)} \\ c_J &= \frac{PJ_e\mu_B\xi}{eM_s\left(1+\xi^2\right)}, \end{aligned} \tag{2.54}$$

or, quite simply, $c_J/b_J = \xi \approx 0.01$. The origin of term involving $b_J$ is the same as the prior discussion, but the non-adiabatic term involving $c_J$ is related to the differences in spin of the current-carrying electrons. The value of $\xi$ shows that the adiabatic term usually dominates. Throughout the motion of the domain wall the adiabatic contribution of the spin-polarised current is absorbed by the change in domain wall profile. However, the non-adiabatic term is not, and this is the term that gives CDDWM a terminal velocity. This theoretical realisation explained the misconception that current driven domain walls only traveled a finite distance, which was contradicted by experiment.

Another group performing simulations on CDDWM were Thiaville *et al* [86]. In their first work they omitted non-adiabatic effects, and using perfect Py nanowires they found that a relatively small 25 Oe magnetic field was required for domain wall motion by a current. This appeared to agree with some published experimental work [86]. Including the effects of surface roughness allowed them to translate domain walls via a current, but not until a current density of $6.85 \times 10^{12}$ Am$^{-2}$ was reached, roughly thirty times larger than observed in experiment. They next formulated an equation similar to equation (2.53), and for a perfect wire they found no critical current density as expected. That is, a perfect wire within the assumptions made by the LLG equation would not expect to exhibit a critical current density. Physically, this is because a perfect wire would offer no coercitivity in an applied field magnetisation loop. Further to this, when roughness effects were included in the simulation a finite critical current density was found, in much better quantitative agreement with experiment [87, 88, 89]. Their findings are summarised in figure (2-18).

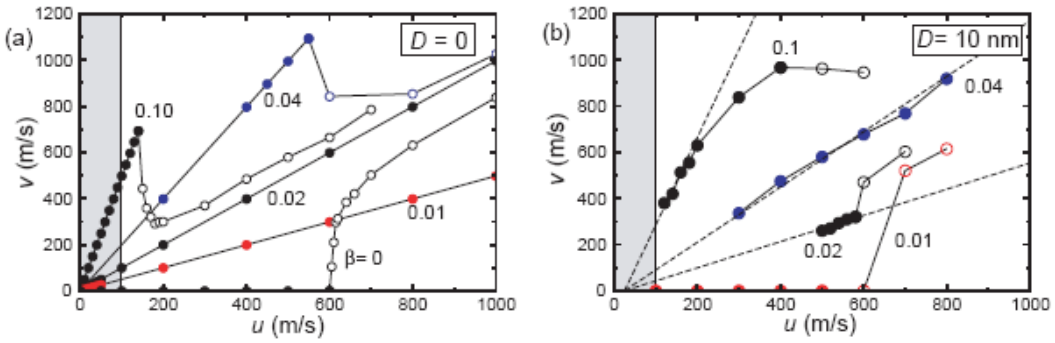


Figure 2-18: Steady state velocities of domain walls driven by a current predicted via micromagnetic simulations in 120 x 5 nm wires with material parameters resembling that of Py. $u = j_e P g \mu_B / (2eM_s)$ is a velocity parameter for CDDWM similar to $b_J$. The different values of $\beta$ are the strength of the non-adiabaticity in the Thiaville equations, and the shaded region to the left of the figures denote (current) experimentally viable regions. (a) is for a perfect wire and (b) is that of a wire with a surface roughness in the region of 10 nm. Figure and parts of caption reproduced from Thiaville [86].

### 2.6.3 Domain Wall Inertia

Doring demonstrated that a domain wall has inertia [90]. This was found to be an intrinsic property from the discovery and knowledge that the spins contain in the domain wall themselves exhibit angular momentum. To envisage this a Bloch wall (one-dimensional wall from figure 2.4, perpendicular to $x$ with spins in the $yz$ projection can be considered. In this scenario, a magnetic field applied parallel to the $y$ axis will cause the magnetisation to rotate. To do this the spins have to precess, and thus leave the $yz$ plane, giving rise to a demagnetising field $H_x = -M_x$. The spin precession causes a a translation of the wall in the $x$-axis with speed $v$. However, there is an additional demagnetising contribution from the components of the magnetisation vector $\mathbf{M}$ that were motion induced. As $M_x$ and $H_x$ are both directly related to the velocity, similar to a *kinetic* energy, this energy contribution will be proportional to $v^2$, . The proportionality constant must therefore have dimensions of mass. Consequently, the domain wall can be considered as having a mass. The mass of the wall can then be related to the static domain wall areal

energy density by:

$$m_{wall} = \frac{\mu_0 \sigma_{DW}}{2Av^2} \,. \tag{2.55}$$

Although some might call the assignment of a mass to something which is not matter specious, domain walls, experimentally and theoretically have been shown to move with inertial character [90]. This mass has a typical density of $10^{-9}$ kg/m$^2$, and implies that the domain wall does not stop *immediately* after an applied field's application is terminated. For memory purposes this effect would need to be studied and included into the dynamics of the memory system.

## 2.7 Micromagnetic Solvers and Parametrisation

FEM or FDM solvers are used to solve the LLG equation. A free, extensively used, and tested micromagnetic solver is the OOMMF package. This package discretises the sample into smaller, cuboidal cells, wherein each cell has a magnetisation vector of a fixed magnitude. Another feature that determines the density of grid points required is termed the exchange length, the same parameter found in equation (2.37). This governs the resolution required to observe the formation of domain walls correctly in the material, helping to ensure that no artificial domain walls are produced, or pinned in place. Finally, if the evolution of the domain wall profile is a necessary output of a calculation, then a mesh smaller than the previous lengths discussed is often required.

Applied current densities in the form of the Thiaville model [91, 8, 86] are implemented in OOMMF via a spin-transfer-torque extension. Therefore, to undertake micromagnetic simulations of current-driven domain wall motion in racetrack memory the building blocks are in place. However, the micromagnetic parameters that overwhelmingly govern the motion of domain walls in the system are not well known. The saturation magnetisation can be straightforwardly calculated by experiment, the damping factor and magnetocrystalline anisotropy can be estimated too. However, the polarisation of a device can only be determined on a surface. The

Table 2.2: Micromagnetic parameters that would directly affect simulations involving current-driven domain wall motion.

| Parameter | $M_s$ | $A$ | $P$ | $K$ | $\alpha$ |
|---|---|---|---|---|---|
| Theory | ✓ | ✓ | ✓ | ✓ | ✓ |
| Experiment | ✓ | ✓ | × | ✓ | ✓ |

cobalt platinum multilayer and trilayer systems all have platinum capping layers, so the cobalt is not directly accessible. Table 2.2 lists the micromagnetic parameter discussed in this section. A noticable void in first-principles calculations specifically for micromagnetic applications motivated the author to investigate electronic structure techniques. Discussions, implementations, and results from these investigations form the following two chapters. It is hoped that the results could be used to parametrise micromagnetic calculations, but experimental parameters could still be used.

# Chapter 3

# Electronic Structure Methods

## 3.1 Introduction and Overview

The previous chapter on micromagnetism primarily dealt with continuum models. In this chapter electronic structure theory and techniques are discussed. In this realm the reader should be particularly aware of the Pauli Exclusion principle and the exchange interaction, and the exciting physics that are a major consequence of them.

In order to understand the origins of observable macroscopic properties of solids, knowledge of the electrical and magnetic components is paramount. Beginning in the early 1900's great strides have been made in this area, spawning among the Born-Oppenheimer approximation [92]This approximation by Born-Oppenheimer concerns separating the momentum of the electron from that of the nucleus in to two discrete problems [92]. Simply analysing the relative speeds and interaction time-scales provides robust validity of the applicability of the approximation. Note that the nucleus weighs at least 5 orders of magnitude more than an electron. Following

on from this the first solution to the many-body problems was theorised by Hartree-Fock [93, 94]. In this theory the single-particle wavefunction of the electrons is used in an attempt to recreate the full solution. Hartree-Fock [93, 94] theory was groundbreaking in that it took into account the antisymmetric character of fermions i.e. the wavefunction has to be change sign when interchanged due to the Pauli exclusion principle. This idea was discussed at length in chapter 2 in section 2.2.3. Consider that the count of crystalline atoms in a typical solid is of order $10^{23}$, and a solution would require solving three times as many coupled differential equations [93, 94]. Computers have progressed more than could have been imagined in recent decades (Popular culture states that Moore did not intend for his law to be gospel, but it has been surprisingly accurate), nevertheless, the many-body problem without extending any assumptions is still numerically intractable. Thomas-Fermi theory is noteworthy: the foundational solution to the many-body problem to use the electron's density, compared to all previous attempts, instead of its wavefunction. Unfortunately the theories modelling of the kinetic energy is abject, and fails to model the exchange [95]. Using the electron density to solve the many-body problem is now called Density Functional Theory (DFT)

DFT is one of the most widely used theories in the field of condensed matter physics. Modern DFT has its roots in the theory first proposed by the likes of Hohenberg, Kohn, and Sham [96, 97]. The foundational principle developed by Hohenberg and Kohn was that they theorised that "there exists at most one potential for a given electron ground-state density" [96, 97]. Following this, Kohn and Sham formalised a perfect solution by utilising an XC (exchange-correlation) potential - but only for the ground state, now affectionately known as the "Kohn-Sham equation" [96, 97].

Kohn and Sham were also the first to propose a tractable implementation of the XC potential - the LDA ("Local Density Approximation") [97]. The LDA is based on including the exchange-correlation potential of "*Jellium*" (a homogeneous electron gas). This was extended to a spin-dependent system by Barth and Hedin in the following paper [98]. The stoner parameter discussed in section 2.2.3 is well described by the LSDA in some ferromagnets [99], i.e. the Local Spin Density Approximation

can accurately describe itinerant magnetism [95]. The idea of using the Jellium potential was then extended to use the XC potential's gradient terms differentiated through the density. This technique is termed the Generalised Gradient Approximation (GGA) and its first implementation was in the seminal paper by Perdew, Burke, and Ernzerhoff [100].

The LSDA can model Iron's magnetic state accurately [95], but actually suggests that the ground-state crystal is FCC (Face Centred Cubic). However, it is known that it is BCC (Body Centred Cubic), which is accurately predicted by the GGA [100]. Both approximations catastrophically fail to predict the existence of Mott insulators [101], as they fail to model the high Coulombic electrostatic interaction of the partially screened d electrons of transition oxides [102]. The Hubbard U parameter has been included in the LSDA+U approximation to address this deficiency: the inclusion of a local Coulomb repulsion marries theory and experiment in some systems [103].

Typically, spin polarisation in many materials is sufficiently well modelled by the LSDA and GGA approximations of the exchange correlation potential. Prior published work often reports difference to within five percent of the experimental systems, which are not always transferable problems. Unsurprisingly, there are contrasts in the computationally simulated magnetic properties and experimentally obtained magnetic properties for many electronic structure problems. This is because they are influenced not only by spin-polarisation, but also orbital polarisation. When concerned with isolated atoms, Hund's rules can be applied to deduce the energy scales, roughly 1 ~10 eV for spin polarisation, 0.1 ~2 eV for orbital polarisation, and similar to the latter value for the spin orbit coupling. In forming a solid the atomic energies are changed and their order may alter. That is, the crystal field, band formation, and the hybridisation of valence electrons generally quench the orbital moment. It is noteworthy that in the transition metals such as cobalt the measured magnetic momenta for the orbital motion is typically less than a tenth of the spin momentum.

In atoms with atomic numbers greater than 30 relativistic effects begin to become

more important. Magnetocrystalline anisotropy - the energy behind the preferred orientation of the magnetisation (explained in section 2.4.3) in crystals is governed by the spin orbit interaction. So, observed values of the parameter would certainly rely on an accurate description of both the orbital and spin moments in the ferromagnet. The variational method used Hohenberg and Kohn discussed in the previous section is non-relativisticExtensions to the equation to include relativity lead to a relativistic equation called Kohn-Sham-Dirac [104]. It is worth noting that orbital polarisation is formed not from correlation effects, but from the combination of spin polarisation and spin orbit coupling. Fundamentally, the interplay leads to a non-zero orbital current density exhibited by the breakdown of time-reversal symmetry.

Computationally solving the many-body problem using density functional theory is usually performed using band structure techniques. Furthermore, Modern methods use the full-potential, and the differences between solvers is usually to do with the potentials and any approximations or modifications, or the basis sets used. Methodologies of implementing density functional theory within a computational framework are not limited to consisting of a superset of the following: "linearised augmented plane waves" (LAPW) [105, 106], "Korringa-Kohn-Rostocker" (KKR) [107, 108], "augmented spherical waves" (ASW) [109], "plane wave pseudopotential" (PWPP) [30], and "linear muffin-tin orbital" (LMTO) approaches [106]. In this thesis PWPP, and full-potential LAPW (FLAPW) implementations of DFT are used.

In DFT scientists have a formalism that enables them to predict observable properties of solids, be that the structure, or magnetism. Often confused with approximate numerical implementations, DFT is, in fact, a mathematically exact representation of the electronic ground state for the many-body problem. First the equations of non-relativistic DFT are presented, followed by their relativistic forms, as these will be required in this thesis. Following from this the implementations of DFT used in this work are presented, and methodologies for obtaining material parameters.

### 3.1.1 Atomic Units

Often used in electronic structure methods, atomic units can be used as a convenient way of not writing many physical constants in equations. Many physicists consider this to be natural order of things, however, in this thesis I will generally use electron volts (eV), angstroms (Å), and S.I. units. This is often justified by comparing and contrasting work with other theoretical and experimental works, which are typically presented in S.I. For completeness the following should encompass all a reader will need to know about atomic units.

In essence: $m_e$ is the effective mass of an electron, $\hbar$ is "Planck's constant" renormalised through a divisor of $2\pi$, $a.u.$ abbreviates atomic unit, Ha is a Hartree, Ry is a Rydberg, $a_B$ is the Bohr radius, and other physical constants have their usual representation. Note the famous bunch of founding fathers of physics within the description [95].

$$1a.u. = \hbar = m_e = e^2 = 2\mu_B \tag{3.1}$$

$$1Ha = 2Ry = 27.2113845eV \tag{3.2}$$

$$1a_B = 5.291772108 \times 10^{-11}m = 0.5291772108 \text{ Å} \tag{3.3}$$

## 3.2 Hard Matter Quantum Mecahnics

In certain potentials the two and three-body Schroedinger equations are analytically solvable. Due to the inherent complexity computational solvers must implement numerical algorithms for problems and more complex than the helium atom.

As we have discussed, the fundamental problem of electronic structure is to model the electronic and ionic interactions, and the extremely complex structures that are the result of these effects. Models need to be accurate enough to predict ground

and excited states. For electrons, the Hamiltonian is essential to the theory of electronic structure. A general system of interacting electrons and nuclei - without any magnetic interactions or relativistic effects - can be described by [95]:

$$\begin{aligned}\hat{H} = -\frac{\hbar^2}{2m_e}\sum_i \nabla_i^2 + \sum_{i,I}\frac{Z_I e^2}{|\mathbf{r}_i - \mathbf{R}_I|} + \frac{1}{2}\sum_{i\neq j}\frac{e^2}{|\mathbf{r}_i - \mathbf{r}_j|} \\ -\sum_I \frac{\hbar^2}{2M_I}\nabla_I^2 + \frac{1}{2}\sum_{I\neq J}\frac{Z_I Z_J e^2}{|\mathbf{R}_I - \mathbf{R}_J|}\,.\end{aligned} \tag{3.4}$$

Here lower cases denote electrons, and upper nuclei, $Z$ is the atomic number, with $m$ and $M$ the masses. Now we can use the aforementioned Born-Oppenheimer approximationWith the assumption of static nuclei, the problem of solving the time independent Schroedinger equation becomes significant easier and deduction of the electronic configuration can be primarily obtained. A calculation could then be performed to evaluate the most energetically favourable positions of the nuclei. The Hamiltonian of the system could now be written

$$\hat{H} = \hat{T} + \hat{V}_{ext} + \hat{V}_{int} + E_{II}\,, \tag{3.5}$$

where the terms are from left to right, $\hat{T}$ kinetic energy, $\hat{V}_{ext}$ the potential acting on the electrons from the nuclei, $\hat{V}_{int}$ the electron-electron interaction operators, and $E_{II}$ the (parameter) nucleon-nucleon interaction energyAlthough S.I. units are desirable for consistency, and have been used throughout this report, electronic structure calculations and equations are much easier to write in *atomic units*. In this system

$$e = m_e = \hbar = 1\,, \tag{3.6}$$

And thus, in this new unit system the Hamiltonian is

$$\hat{H} = \sum_i -\frac{1}{2}\nabla_i^2 + \sum_{i,I} V_I(|\mathbf{r}_i - \mathbf{R}_I|) + \frac{1}{2}\sum_{i\neq j}\frac{1}{|\mathbf{r}_i - \mathbf{r}_j|} + E_{II}\,. \tag{3.7}$$

The nuclei's interaction with the electrons is described in the fixed potential termThe ionic nucleus' electrostatic attraction can be included in a pseudopotential (PP) [95]. This pseudopotential would count the core electrons as screening charges for the nucleus when considering interactions. Other external potentials such as applied

magnetic or electric fields could also be include in the external potential.

Quantum mechanically for a non-relativistic system the governing equation is the time dependent Schrodinger equation [110]:

$$\hat{H}\Psi(\{\mathbf{r}_i\},t) = i\hbar\frac{\mathrm{d}\Psi(\{\mathbf{r}_i\},t)}{\mathrm{d}t}\,, \tag{3.8}$$

the many-body wavefunction is $\Psi(\{\mathbf{r}_i\},t)$, and $\{\mathbf{r}_i\}$ represent space and spin. Implementing the Pauli exclusion principle we know that the wavefunction should exhibit antisymmetry under exchange, and the eigenstate is [110]

$$\Psi(\{\mathbf{r}_i\},t) = \Psi(\{\mathbf{r}_i\})e^{-(E/\hbar)t}\,. \tag{3.9}$$

Finally, system energy can be found from the expectation value of the Hamiltonian.

### 3.2.1 The Kohn-Sham Equations

To transform the problem into one which we can solve using DFT, we need to look at occupations, $n$, of the particles and not their wavefunctions. The map

$$n(\vec{r_1}) = N\int \mathrm{d}^3r_2\int \mathrm{d}^3r_3\,..\int \mathrm{d}^3r_N\Psi^*(\{\mathbf{r}_i\})\Psi(\{\mathbf{r}_i\}) \tag{3.10}$$

yields a method for finding the density from the wavefunction, but how do we make the reverse possible [97]? The ground state wavefunction could be described as a functional (note that a function of variable returns a number, a functional of a function returns a number) of the unique ground state density, or

$$\Psi_0 = \Psi[n_0]\,. \tag{3.11}$$

Kohn and Sham [97] took this approach and developed the ansatz for DFT - deal with independent particles which have an interacting density. The premise revolves

around transforming a difficult problem in to a simpler one, but managing to ensure the GS solutions are comparable. Discussed in the introduction to this section, the difficult to handle terms are bundled in to the XC potential. All in all, the method relies on solving the density problem with accuracy only mediated by the quality of XC functional, finding the ground state density and hence the ground state wavefunction. This approach has prompted the description of solving these equations as *ab initio*, or from first principles. Remember the XC consists of many types [111, 100].

To this end the Kohn-Sham approach to the formulating the GS energy of many interacting particles is [95]

$$E_{KS} = T_s[n] + \int \mathrm{d}\mathbf{r} V_{ext}(\mathbf{r}) n(\mathbf{r}) + E_H[n] + E_{II} + E_{XC}[n]\,, \tag{3.12}$$

where the independent particles for each spin have a K.E. of $T_s[n]$, and

$$E_H = \frac{1}{2}\int \mathrm{d}^3 r \mathrm{d}^3 r' \frac{n(\mathbf{r})n(\mathbf{r}')}{|\mathbf{r}-\mathbf{r}'|}\,. \tag{3.13}$$

Furthermore, the individual particles will have their own wavefunctions, e.g.

$$\Psi(\{\mathbf{r}_i\}) = \psi(\mathbf{r}_1)\psi(\mathbf{r}_2)\,..\,\psi(\mathbf{r}_N) \tag{3.14}$$

An intermediate formula for the XC energy is [95]

$$E_{XC}[n] = <\hat{T}> - T_S[n] + <\hat{V}_{int}> - E_H[n]\,. \tag{3.15}$$

If this functional were to be known *exactly* then electronic structure problems would be entirely accurate.

The Kohn-Sham equations are similar to the single particle Schrodinger equation:

$$(\hat{H}^\sigma_{KS} - \epsilon^\sigma_i)\psi^\sigma_i(\mathbf{r}) = 0\,, \tag{3.16}$$

where

$$\hat{H}^{\sigma}_{KS} = -\frac{1}{2}\nabla^2 + V^{\sigma}_{KS}(\mathbf{r}) = -\frac{1}{2}\nabla^2 + V_{ext}(\mathbf{r}) + V_H(\mathbf{r}) + V^{\sigma}_{XC}(\mathbf{r}) \quad (3.17)$$

$$= -\frac{1}{2}\nabla^2 + V_{ext}(\mathbf{r}) + \frac{\delta E_H}{\delta n(\mathbf{r},\sigma)} + \frac{\delta E_{XC}}{\delta n(\mathbf{r},\sigma)}\,. \quad (3.18)$$

### 3.2.2 Including Relativistic Effects

Relativistic effects can be important in the simulation of heavier atoms [95], and where physical effects caused by the spin orbit interaction are tangible. Cobalt and platinum are used in this work, and this interaction is one of the reasons for magnetocrystalline anisotropy in the 3d ferromagnets. However, these effects do not make significant contributions to the structure and properties of most lighter molecules and solids. Conveniently, relativistic effects originate deep inside the core of the atom. This typically means that the relativistic equations need only to be solved in the atom's spherical geometry. In molecules and solids this observation is transferred. Starting from Dirac's 1928 equation [112, 113],

$$i\hbar\frac{\partial}{\partial t}\mathbf{\Psi} = \left(c\alpha.\mathbf{p} + \beta mc^2\right)\psi = \hat{H}\mathbf{\Psi} \quad (3.19)$$

a generalisation of the Schrodinger equation in a relativistically covariant form. Where $\alpha_i$, $\beta$ (4 x 4 matrices), and $\sigma_i$ (2 x 2 matrices) are the matrices - the Pauli spin matrices - defined as [110]:

$$\alpha_i = \begin{pmatrix} 0 & \sigma_i \\ \sigma_i & 0 \end{pmatrix}\,,\ \beta = \begin{pmatrix} \mathbf{1} & 0 \\ 0 & -\mathbf{1} \end{pmatrix}\,,$$
$$\sigma_1 = \begin{pmatrix} 0 & 1 \\ 1 & 0 \end{pmatrix}\,,\ \sigma_2 = \begin{pmatrix} 0 & -i \\ i & 0 \end{pmatrix}\,,\ \sigma_3 = \begin{pmatrix} 1 & 0 \\ 0 & -1 \end{pmatrix}\,, \quad (3.20)$$

$\mathbf{p} = s - i\hbar\vec{\nabla}$ is the momentum operator. The problem can then be split in to radial functions and a sinusoidal time varying wave.

$$\Psi(x^{\mu}) = \mathrm{e}^{-i\epsilon t/\hbar} \begin{pmatrix} \phi(\mathbf{r}) \\ \chi(\mathbf{r}) \end{pmatrix} \tag{3.21}$$

allows, the derivation of radial equations. As long as the value for spin-orbit interaction is able to be ignored and can be treated as a perturbation, this yields the scalar relativistic equation and a spin-orbit Hamiltonian of

$$\hat{H}_{SO} = \frac{\hbar^2}{2M^2c^2}\frac{1}{r}\frac{\mathrm{d}V}{\mathrm{d}r}\mathbf{L}.\sigma. \tag{3.22}$$

This term originates near the core of the atom where $\frac{1}{r}\frac{\mathrm{d}V}{\mathrm{d}r}$ is large, confirming the earlier statement detailing that the equations should hold for atoms, molecules, and solids. Pseudopotentials are sometimes used to aid in simplifying the equations that need to be solved: they can incorporate the spin-orbit effects leaving only the non-relativistic equations to be solved. More detail will be given on the implementation in section 3.3.1.

The Kohn-Sham-Dirac equation's derivation can be found in [114, 115, 116]. It is normally written as:

$$\left[c\alpha\,.\,[\hat{\mathbf{p}} - e\mathbf{A}_{eff}(r)] + \beta mc^2 + V_{eff}(r)\right]\psi_i(\mathbf{r}) = w_i\psi_i(\mathbf{r})\,, \tag{3.23}$$

where $\psi_i(\mathbf{r})$ are set of single particle, four-component eigenstates, and the $w_i$ are Lagrange multipliers behaving as eigenvalues. The relativistic charge and current densities are now given by [113, 95]

$$n(\mathbf{r}) = \sum_{i=1}^{N} \psi_i^{\dagger}(\mathbf{r})\psi_i(\mathbf{r}), \quad \mathbf{J}(\mathbf{r}) = c\sum_{i=1}^{N} \psi_i^{\dagger}(\mathbf{r})\alpha\psi_i(\mathbf{r}) \tag{3.24}$$

summed over the lowest $(N)$ electron eigenvalues. The effective vector and scalar potentials, $\mathbf{A}_{eff}(\mathbf{r})$ and $V_{eff}(\mathbf{r})$ are given by:

$$\mathbf{A}_{eff}(\mathbf{r}) = \mathbf{A}_{ext} + \int \mathrm{d}^3\mathbf{r}'\frac{\mathbf{J}(\mathbf{r})}{|\mathbf{r}-\mathbf{r}'|} + \frac{1}{e}\frac{\delta E_{XC}[n(\mathbf{r}),\mathbf{J}(\mathbf{r})]}{\delta\mathbf{J}(\mathbf{r})} \tag{3.25}$$

and

$$V_{eff}(\mathbf{r}) = V_{ext} + \int \mathrm{d}^3\mathbf{r}' \frac{n(\mathbf{r})}{|\mathbf{r}-\mathbf{r}'|} + \frac{\delta E_{XC}[n(\mathbf{r}), \mathbf{J}(\mathbf{r})]}{\delta n(\mathbf{r})} \,. \tag{3.26}$$

Following from reference [117] the relativistic total energy functional can be written as:

$$\begin{aligned} W[n(\mathbf{r}), \mathbf{J}(\mathbf{r})] = \sum_{i=1}^{N} w_i - \frac{1}{2} \int \mathrm{d}^3\mathbf{r} \int \mathrm{d}^3\mathbf{r}' \frac{n(\mathbf{r})n(\mathbf{r}')}{|\mathbf{r}-\mathbf{r}'|} + E_{XC}[n(\mathbf{r}), \mathbf{J}(\mathbf{r})] + \\ \frac{1}{2c^2} \int \mathrm{d}^3\mathbf{r} \int \mathrm{d}^3\mathbf{r}' \frac{\mathbf{J}(\mathbf{r})\mathbf{J}(\mathbf{r}')}{|\mathbf{r}-\mathbf{r}'|} \\ - \int \mathrm{d}^3 n(\mathbf{r}) \frac{\delta E_{XC}[n(\mathbf{r}), \mathbf{J}(\mathbf{r})]}{\delta n(\mathbf{r})} + \int \mathrm{d}^3\mathbf{J}(\mathbf{r}) \frac{\delta E_{XC}[n(\mathbf{r}), \mathbf{J}(\mathbf{r})]}{\delta \mathbf{J}(\mathbf{r})} \,. \end{aligned} \tag{3.27}$$

The non-relativistic expression, containing the energy eigenvalues, the Hartree term, and the XC value form the first line of equation 3.27. Analogous to the the Hartree term, the second line contains the classical current-current interaction. As the exchange-correlation is a functional of both the current densities and the charge then the final line is obtained. The lack of dependence on the vector potential is an example of gauge invariance, the total energy functional does not depend explicitly on $\mathbf{A}(\mathbf{r})$. The XC can be modelled in a similar to the non-relativistic. However, it is also performs not so well in some systems arising due to Jelliums poor implementation of correlation. The difficulties in relativistic approximations of the XC functional have led to many electronic structure calculations using non-relativistic approximations [102]. That is, many calculations use non-relativistic LDA in relativistic calculations.

In this thesis we are concerned with the magnetic properties of relativistic atoms. Similar to the above equations, a relativistic density functional theory that depends on the magnetisation and not the four current density [114, 116]. A Hamiltonian of the form, in [114] MacDonald's 1979 paper, follows

$$\hat{H} = \hat{H}_{sys} + \int \mathrm{d}\mathbf{r} \left[ n(\mathbf{r}) v(\mathbf{r}) - \hat{\mathbf{m}}(\mathbf{r}) \,.\, \mathbf{B}(\mathbf{r}) \right] \tag{3.28}$$

where

$$v(\mathbf{r}) = -\frac{eA_0(\mathbf{r})}{c} \, , \hat{\mathbf{m}}(\mathbf{r}) = -\mu_B \psi^\dagger(\mathbf{r}) \sigma \psi(\mathbf{r}) \, , \mathbf{B}(\mathbf{r}) = \nabla \times \mathbf{a}(\mathbf{r}) \, . \tag{3.29}$$

Finally, it is worth again noting that relativistic effects are core effects. These can be included in a pseudopotential, meaning that one still has to only solve the non-relativistic Schrodinger equation outside of the pseudopotential radius, and not the Dirac equation.

## 3.3 DFT Implementations

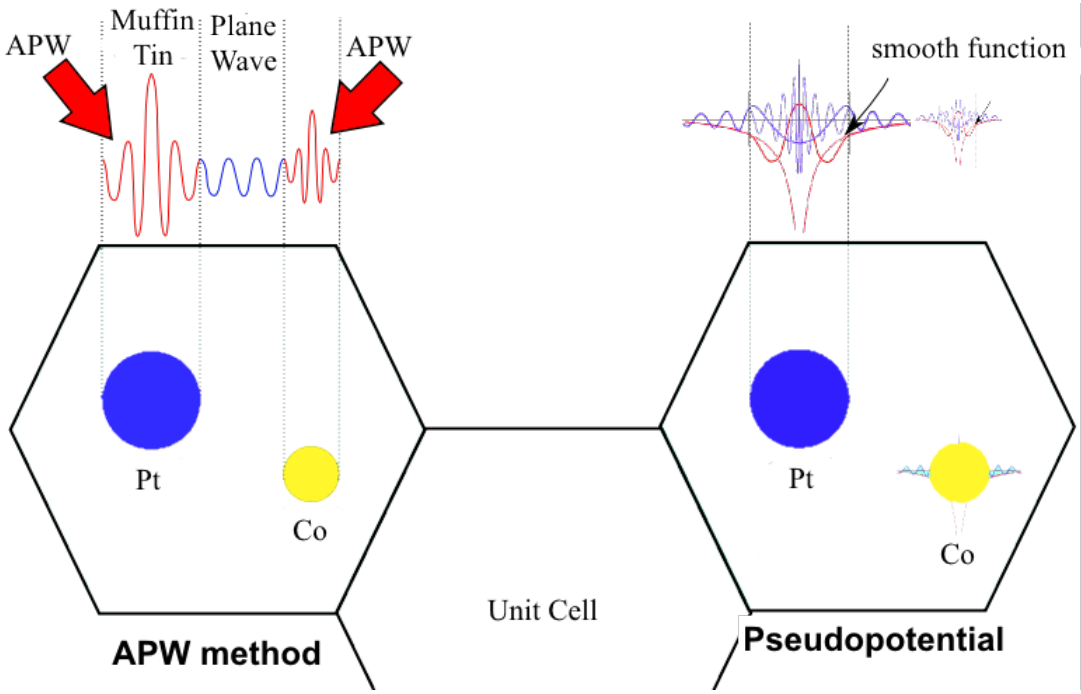


Figure 3-1: Schematic showing differences between the plane-wave pseudopotential and augmented plane wave methods.

Cobalt and platinum's different lattice constants imply that at a surface boundary there will be some kind of surface relaxation. The breaking of lattice symmetries and

the energetics cannot be simply evaluated by hand. A DFT code implementation such as CASTEP or ELK can be used to find total energies for different crystal configurations. With knowledge, experience, convergence, and parameterisation automatic structural relaxation can be undertaken. Note that DFT is a ground state theory, so predictions and results are limited to ground state phenomena.

### 3.3.1 CASTEP: Plane Wave Pseudopotential Method

CASTEP's limitations and features are now presented, but readers wishing to fully understand the implementation are referred to the CASTEP web pages [118] and discussion groups [119].

CASTEP uses plane waves to describe the electronic wavefunctions. All calculations have periodicity, and thus Bloch's theorem can be implemented. The eigenfunctions of the Schrodinger equation are then able to be transcribed as

$$\psi(\mathbf{r}) = \sum_{\mathbf{k}+\mathbf{G}} c_{i,\mathbf{k}+\mathbf{G}} \times \frac{1}{\sqrt{\Omega}} e^{i(\mathbf{k}+\mathbf{G})\,.\,\mathbf{r}}\,, \tag{3.30}$$

where $\mathbf{G}$ the reciprocal lattice vectors, $\Omega$ is the unit cell volume, and $c_{i,\mathbf{k}+\mathbf{G}}$ are the Fourier expansion coefficients, and $\mathbf{k}$ another reciprocal space vector [95].

The effective potential in the primitive cell can be written using the Fourier components as it is periodic, allowing the Schrodinger equation for any reciprocal space vector to be determined. The above formulation leads us directly to Bloch's theorem:

$$\psi(\mathbf{r}) = \sum_{\mathbf{k}+\mathbf{G}} c_{i,\mathbf{k}+\mathbf{G}} \times \frac{1}{\sqrt{\Omega}} e^{i(\mathbf{k}+\mathbf{G})\,.\,\mathbf{r}} = e^{i\mathbf{k}\,.\,\mathbf{r}} \frac{1}{\sqrt{N_{cell}}} u_{i,\mathbf{k}}(\mathbf{r})\,, \tag{3.31}$$

in which $\Omega = N_{cell}\Omega_{cell}$, and $u_{i\mathbf{k}}(\mathbf{r}) = \frac{1}{\sqrt{\Omega_{cell}}} \sum_m c_{i,m}(\mathbf{k}) e^{i\mathbf{G}\,.\,\mathbf{r}}$, a periodic function. Furthermore, Bloch's theorem also tells us that the first Brillouin zone yields all of the information to be known from the Schrodinger equation. All of the basis

functions used in CASTEP are orthogonal, meaning that operations performed on them such as Fourier transforms are computationally efficient. Furthermore, if a system is not naturally periodic (e.g. a surface), then CASTEP can still be used by defining a spacer region of empty space. This can be computationally expensive, but allows the simulation of more physical systems [95].

However, the orthogonality condition does lead to increased computations and convergence parameters. As the states are filled, increasing orthogonality forces the wavefunctions to have an increasing number of nodes. This poses a problem for simulation, as the quantity of dedicated plane-waves imperative to model a wavefunction dramatically increases. However, the core region around the nucleus involving the tightly bound electrons have wavefunctions which are relatively static. A significant number of the lower energy states are localised in this core region [95].

The pseudopotential (PP) replaces the effect of the highly charged ionic core. An *effective* ionic potential, which interacts with the valence electrons, simply replaces the generally inconsequential core electrons. Essentially, it is the substitution of one problem for another. As the core electrons can have little impact in a molecular calculation as they are not involved in bonding, PPs can be made for atoms and then used as an approximation. Additionally, the PP is not unique. One has the ability to tailor PPs to specific calculations. The radius of the pseudopotential may need to be reduced in high pressures, or not as many electrons should be pseudised away.

The localised electrons are pseudised away in the pseudopotential approximation. Their wavefunctions are not considered, and instead an effective potential to represent them is included in the calculations. The effective potential from the localised wavefunctions combined with the nuclear Coulomb potential is termed in CASTEP as the *pseudopotential*. The number of states has been reduced, so that the quantity of nodes in the remaining plane waves decreases from the orthogonality condition, but still leaving the wavefunctions outside of the core region untouched. CASTEP utilises by default *ultrasoft* pseudopotentials (USPP)'s. These are PPs that are as smooth as possible. In CASTEP calculations the valence electron eigenfunctions

are expanded in Fourier components. USPP's attempt to make the simulation as accurate as norm-conserving ones by a transformation. Norm-conserving pseudopotentials (NCPP's) are defined and regarded as the most transferrable and accurate PP's. They are usually built for the isolated atom and intended to be reused for the atom in ionic, molecular, and condensed states. USPP's are utilised as they are computationally cheaper than NCPP's, but need to be tailored for individual situations. An example of two USPP's used to model cobalt atoms are shown in figure 3-2. The first PP is the default USPP used in CASTEP for modelling cobalt. This USPP, however, can be augmented to include extra semi-core states, allowing a more suitable fit for some observable quantities in crystalline cobalt.

It is reported that pseudopotential implementations are computationally efficient methods for solving relativistic DFT problems [120]. A pseudopotential can be used to include the relativistic effects, and allow solution of the non-relativistic Kohn-Sham equations. At the time of performing this research, CASTEP was not able to properly implement relativistic calculations for materials. However, at the time of writing, this feature has been added to the code base, although the author is unsure of its maturity and applicability to cobalt platinum systems. CASTEP has also been used to model, in many different media, surface absorption and structural studies [121].

### 3.3.2 ELK: Full-Potential Linearised Augmented Plane Wave Method (FLAPW)

(FLAPW) is an all-electron technique that is generally considered to universal with DFT. It can be used to represent all atom species, solids and open structures. It is the most accurate and portable DFT based simulation procedures [122]. The all-electron nature of the calculation means that magnetism and magnetic properties of the system are all treated rigorously. Estimates of relativistic effects are included by solving the relativistic electronic structure equations for the density.

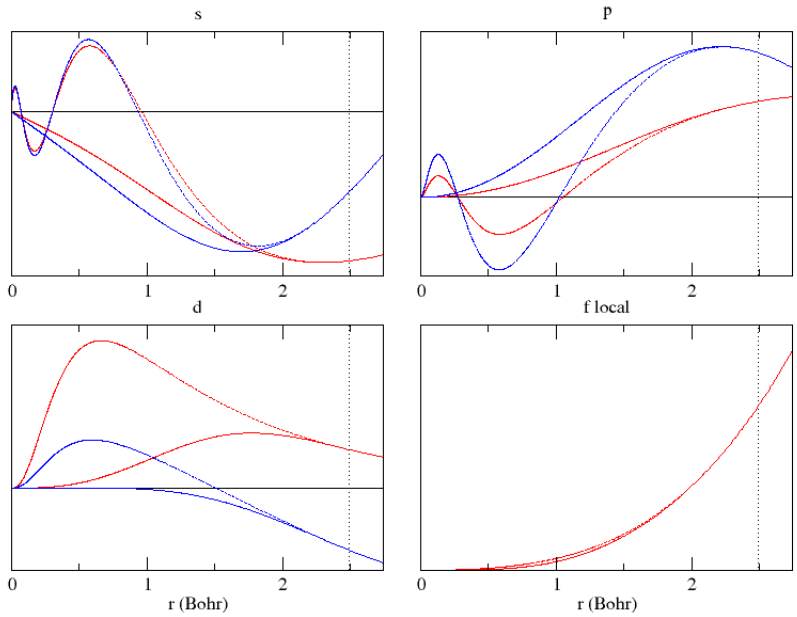


(a) Default CASTEP cobalt PP

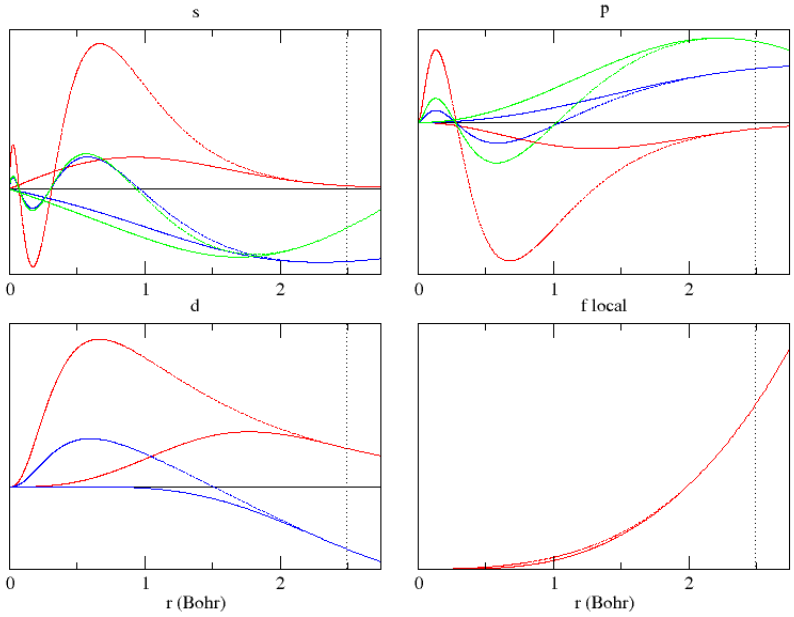


(b) CASTEP cobalt PP including 3s and 3p states

Figure 3-2: The all-electron and pseudo wavefunctions for cobalt with a cut-off radius of 2.5 bohr, showing the valence channels. The functions that do not vary as strongly are the pseudopotentials, with Red and blue are the two different channels. In (a) the states are 4s, 4p and 3d, with 2 channels for each. In (b) singular channels for the 3s and 3p states are introduced.

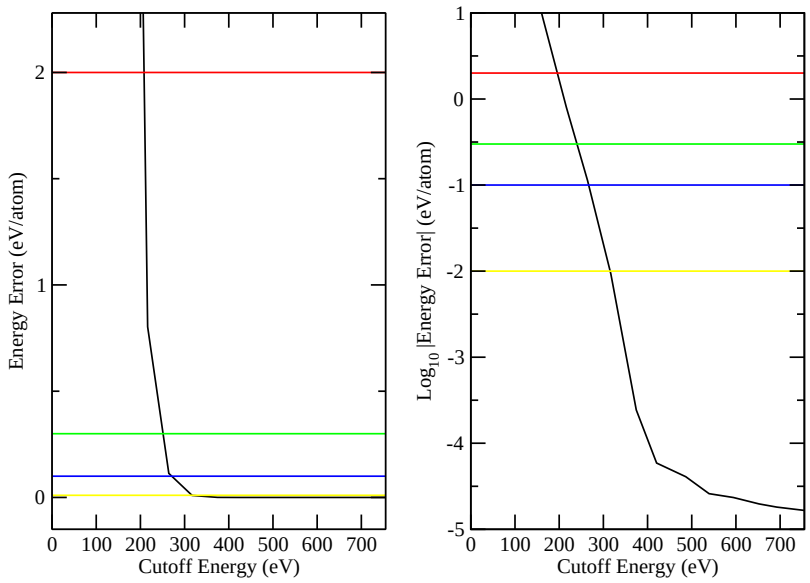


(a) Pseudopotential Convergence

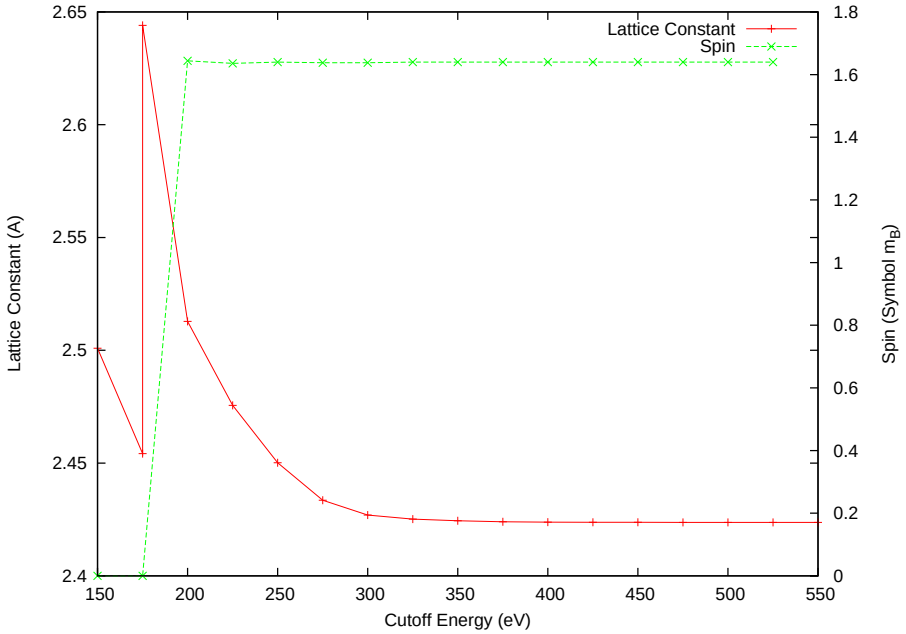


(b) Spin and Lattice Constant Convergence

Figure 3-3: (a) The convergence of the default CASTEP cobalt pseudopotential with the plane wave energy cut-off for a cut-off radius of 2.5 bohr. The red, green, blue and yellow horizontal lines intersection with the curve denotes the cut-off energy used if the 'coarse', 'normal', 'fine' or 'extreme' keywords are used for energy cut-off. (b) The convergence of spin magnetic moment and lattice constant of cobalt with cutoff energy using the default pseudopotential.

Basis functions in the augmented method are energy dependent, leading to difficulties arising from having to solve separately for each eigenenergy, and nonlinear equations. Linearisation occurs due to the use of linear combinations with the polar functions and its energetic derivative, at a fixed energy [95]. The accuracy and universality of the FLAPW method is computationally expensive. The large basis set means that the potentials must be represented to a high degree of accuracy. FLAPW results are sometimes used as benchmarks for other DFT based techniques.

In ELK the potential is found by evaluating the Poisson's equation for the run-of-the-mill potential and by the spherically asymmetric terms inside the spheres. The extra waiters unfortunately depend on the schematic of the charge density inside the sphere. From this the charge inside the muffin tin is replaced by a smoother charge, which does not affect the potential outside. The augmented plane wave approach joins the ability to consider the core states as atomic-like spherical functions, and the valence (delocalised) states as plane waves. In essence the Bloch wavefunctions for the crystal are actually solved distinctly for the two different regions in terms of the augmented plane wave basis functions. This approach and be linearised and yields more a useful form, and this is implemented in ELK.

Principles of augmented plane waves were developed by Slater [123]. The eigenstates are expanded in terms of basis functions which are dependent on position. The two regions are usually called the interstitial region - between the atoms, and a sphere centred on the nucleus. In the interstitial region the potential is smoothly varying, but in the sphere the potential is similar to that of the actual atom. The most special case of this is of the muffin tin potential. Here the potential in the sphere is spherically symmetric but varying, and outside it is constant. This allows for significant simplification of the DFT problem. One could implement spherical harmonic in the sphere, and plane waves without.

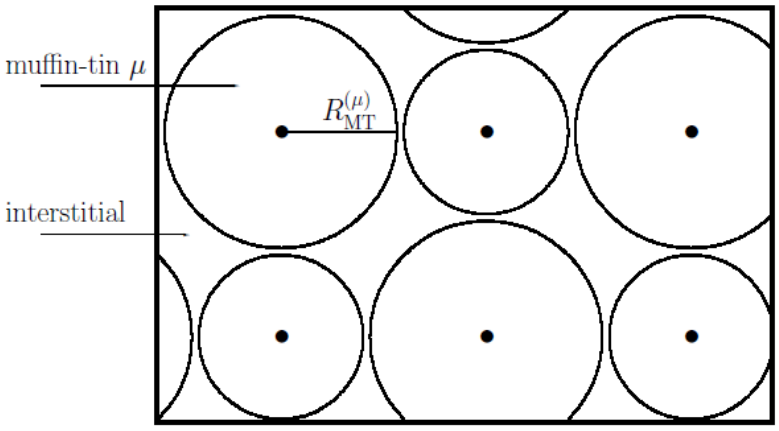


Figure 3-4: Division of space employed by a FLAPW method.

## 3.4 Material Modelling in DFT

### 3.4.1 Package Operation

After telling a DFT code to execute the package will make a guess to the electron density, based on atomic theory or otherwise. It will then attempt to mix the density with a solution of the Kohn-Sham equations for the system, and checks the result of the mix for self-consistency. If this fails then the process is repeated. The flowchart in figure 3-5 shows the process in a more coherent manner.

### 3.4.2 Typical Output

The eigenvalue spectrum and occupancy is the first major output of a DFT calculation. Of course, interest should only be paid to energy levels below the Fermi energy. This is because DFT is a ground-state theory, and results that use eigenvalues above the Fermi energy cannot be relied upon. The occupancies of electron orbitals, and values of magnetic moments are available. Band structures and density of states

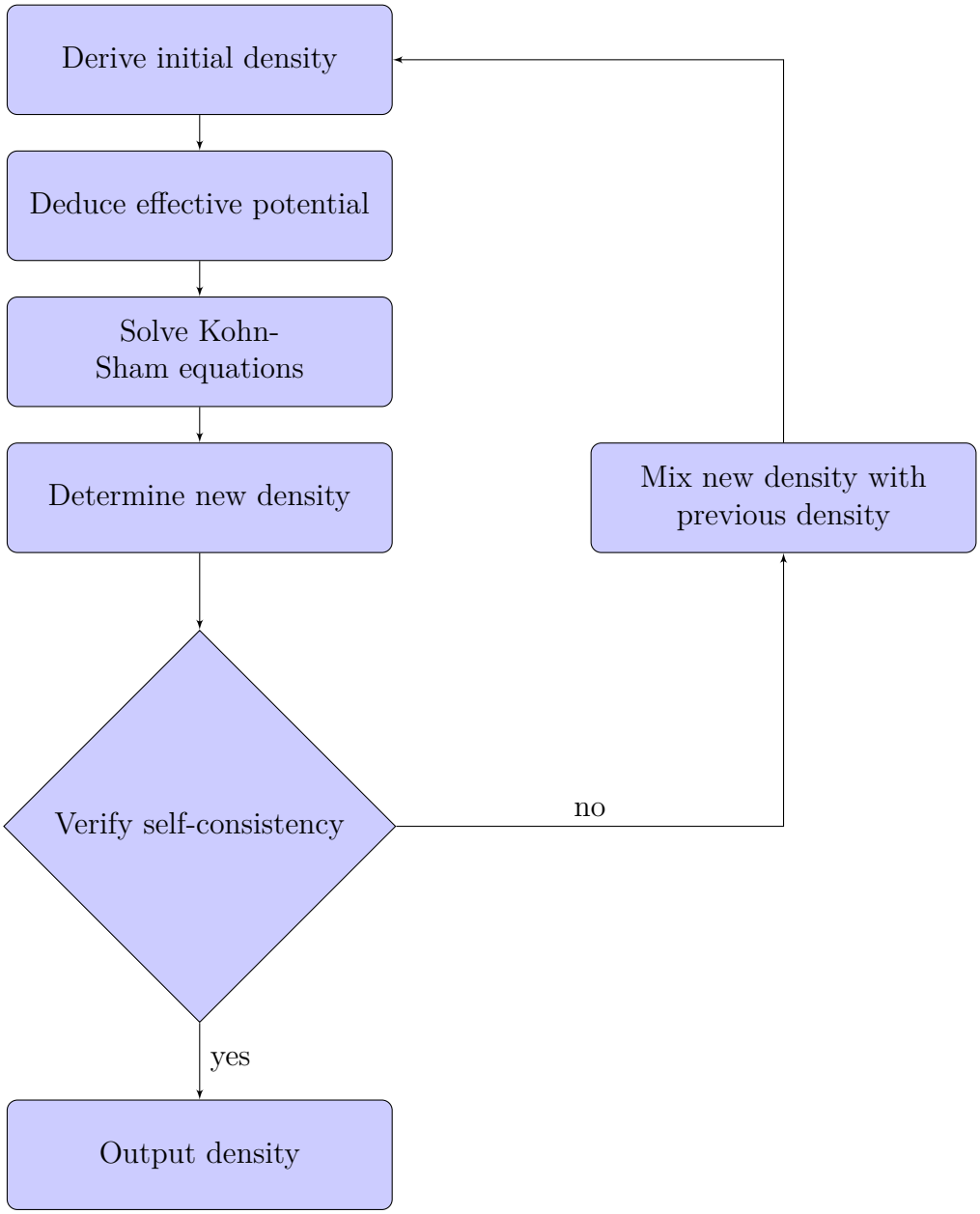


Figure 3-5: Flowchart indicating the typical path taken by an eigenvalue minimiser in a DFT calculation.

Table 3.1: Parameters that need to be converged in CASTEP and ELK calculations. $N_k$ is the number of k-points, $E_{cutoff}$ is the plane wave cut-off energy, $l_{max}$ the atomic basis, $N_g$ planewave basis and swidth the smearing width.

| Parameter | $N_k$ | $E_{cutoff}$ | $l_{max}$ | $N_g$ | swidth |
|---|---|---|---|---|---|
| ELK | ✓ | ✓ | ✓ | ✓ | ✓ |
| CASTEP | ✓ | ✓ | × | ✓ | ✓ |

plots can be generated quickly. Bespoke data processing tools need to be written to obtain many more complex parameters which should be accessible from DFT.[1]

### 3.4.3 Convergence

As both CASTEP and ELK use plane waves to expand the wavefunctions, tests need to be undertaken to ensure the number of plane waves is sufficient to model them correctly. Most tests for convergence involve checking physical observables and energy differences on parameters. If a representation of a physical observable dependent on a parameter $\chi$ varies within allowed tolerances upon a small change of the parameter $\delta\chi$, then the observable would be deemed converged. In other words, if a convergence parameter is changed and a response is observed in the calculation of a physical observable, then the systematic error of the parameter has not been properly removed from the simulation. This is a common cause of inaccuracies from DFT simulations. The user of the DFT package implementation is able to set the parameters used, and estimate, evaluate, and plot the convergence criteria required to remove all parametrisable sources of error.

CASTEP has other convergence criterion which are used in its geometry optimiser. The tolerances of atomic position on the lattice constant and the magnitude of energy differences required are indicative of what values the geometry optimiser

[1]Remark: Due to the approximations made in making the theory computationally tractable it is worth noting that even the occupied eigenvalues from the DFT calculations are not reliable. Naturally, due to the reformulation of the problem in to the density framework, the eigenvalues themselves obtained from variational calculus are not representative.

and self-consistency checker should have. A previous package had a default self-consistency threshold of 100 $\mu$eV. This value would be sufficient for many DFT calculations. However, for magnetocrystalline anisotropy investigations, where difference of $\mu$eV are expected, the convergence criterion is orders of magnitude too high to have any confidence in the result. The results of all convergence calculations will not be included in this thesis, every calculation for a new property has to be checked. Sample convergence calculations (see figures 3-3, 3-6, and 3-2) will be presented for each micromagnetic parameter. Figure 3-6 demonstrates how not only the convergence criterion can effect a simulation. The ratio and method detailing the mixing of $n_{i-1}$ (density of iteration $i-1$) and $n_i$ (density of iteration $i$) can lead to simulations becoming unable to escape the metastable non-magnetic solution. That is, care needs be taken and previous results used as a guidance to verify that the answer is converged to a global minimum, and not one of the many potential local minima.

## 3.5 Summary of Electronic Structure Methods

CASTEP solves the Kohn-Sham equations using a plane-wave pseudopotential method. This method is comparatively computationally inexpensive, and has been used by many research groups to a high degree of success. CASTEP has the ability to relax a geometry automatically, even changing lattice constants to find a more energetically favourable configuration. It is often the case where a package such as CASTEP is used to obtain a starting point for all-electron calculations.

ELK can solve the Kohn-Sham or Kohn-Sham-Dirac equations using the all-electron linearised augmented plane wave method. This is expensive as every electron is modelled, although the problem is made simpler by the use of spherical harmonics to augment plane waves to make them more suitable for modelling wavefunctions near the core. The inclusion of relativistic effects such as spin-orbit coupling means that ELK should be suitable for modelling most parameters, but computation time may be increased extensively.

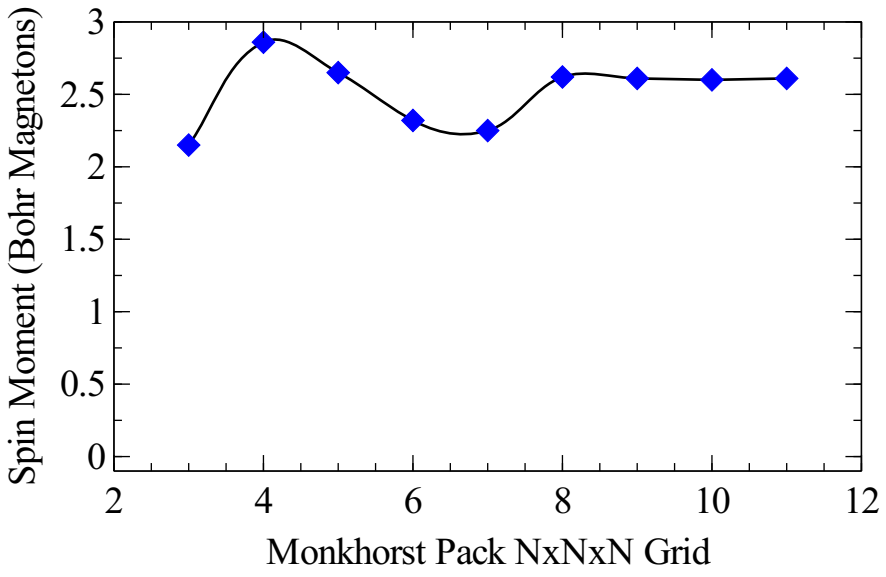


a) K-point Convergence

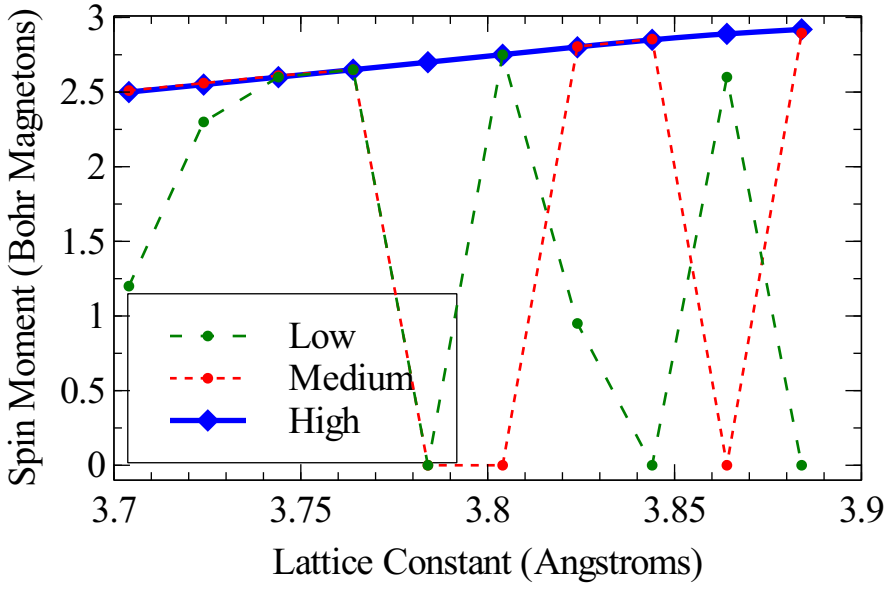


b) Cut-off Energy Convergence

Figure 3-6: Convergence of the total spin moment with plane-wave cut-off energy in $CoPt_3$ with lattice constants of 3.804 Å in the ELK package.

With most DFT packages computational tricks can be used to aid in the time taken. Simply reusing the density from a very similar problem can save literally days of time. The simulations in this thesis requires the minimisation of the atomic and electronic structure. The lattice constants are obtained by running the DFT model to find the lowest energy state (noting that these energies are not real energies, but the differences in energy are where the information is stored). If the lattice spacing is changed by 0.1 Å, then one could simply reuse the prior electron density as a starting point, rather than starting from scratch with the monatomic estimate. In convergence calculations with regards to paramters such as the k-points density this can lead to unitary iterations being performed by the DFT package for complex systems, wheras a fully self-consistent simulation could take closer to fifty iteration to converge.

# Chapter 4

# Ab Initio Modelling of Cobalt Platinum Systems

## 4.1 Foreword

This chapter will look at the properties of cobalt platinum systems from a condensed matter theorist's point of view, with the overall aim of determining material parameters. The aim of the simulations being to simulate otherwise computationally intractable systems using a different model on a longer length scale. The electronic structure methods used and their implementation in the CASTEP and ELK code packages were presented in chapter 3. Electronic structure formulations for material parameters are discussed, and then results for pure, alloyed, film, and multilayer cobalt platinum are presented.

## 4.2 Ab-Initio Material Parameters

### 4.2.1 Interatomic Spacing

When attempting to calculate the interatomic spacing, and ground state of a crystal using DFT the standard process defined in figure 3-5 is followed. The total energy, although a meaningless physical quantity, can be converged with respect to interatomic spacings of periodicity. This quantity converges slowly, and is a common cause for simulations being conducted with excessively high convergence criterion. This comes with great cost to computational efficiency, but does not affect the accuracy of results. When performing DFT calculations, energy differences are the relevant quantities. Considering energy differences also makes the results more portable: different methodologies will generally return different total energy figures for computations. Energy differences afford comparisons of systemic errors in regimes, e.g. the s-p hybridised band is poorly treated in non-relativistic DFT calculations.

### 4.2.2 Magnetic Moment

The magnetisation can be obtained from density functional theory calculations, although care should be taken as from reading this section and the results it can be seen how strongly the magnetic moment depends on deducing the correct crystalline ground state (it in itself can be effect the lattice constant and lowest energy configuration). The occupation numbers $f_i$ and eigenfunctions $\psi_{i\sigma}(\mathbf{r})$ are used to find the magnetisation observable in the usual quantum mechanics representation:

$$\mathbf{m}(\mathbf{r}) = \sum_{i\sigma\sigma'} \psi^*_{i\sigma}(\mathbf{r}) f_i \psi_{i\sigma}(\mathbf{r}) \sigma_{\sigma\sigma'} \tag{4.1}$$

, or, for the Dirac-style spin-only magnetisation [36]

$$\mathbf{m}(\mathbf{r}) = \sum_{i}^{occ} \psi_i^{\dagger}(\mathbf{r}) \underline{\underline{\beta\sigma}} \psi_i(\mathbf{r}) \tag{4.2}$$

The saturation magnetisation of the material can then be approximated by dividing the magnetic moment by the unit cell volume. Or, rigorously [95]:

$$M_s = \frac{1}{V^2} \int \mu dV \tag{4.3}$$

### 4.2.3 Polarisation

The polarisation of a material can be taken to mean many different phenomena. It could refer to the electromagnetic radition. In this thesis we are interest in the spin-polarisability of the material. There are two common relevant measures for the polarisation that are straightforward calculations from ab-initio studies. Firstly, the density ratio [79]:

$$P = \frac{n_{\downarrow} - n_{\uparrow}}{n_{\downarrow} + n_{\uparrow}}, \tag{4.4}$$

and secondly, the ratio of the Fermi energy density of states:

$$P = \frac{g(E_F(\downarrow) - g(E_F(\uparrow))}{g(E_F(\downarrow) + g(E_F(\uparrow))}, \tag{4.5}$$

where majority/minority ($\downarrow$ / $\uparrow$) spin density of states at the Fermi energy $E_F$ [79] are written as $g(E_F)$. The density of states measure is less problematic. Using the electron density can lead to unrealistic spikes in the polarisation due to the same in spikes the raw density occupation numbers. The density of states is smeared by artificially small Gaussians, in order to make the density of states more indicative of a real system. The density of states is spread to make the mathematical function smoother. This effects means that properties that depend on the density of states at the Fermi energy become less dependent on the exact Fermi energy. This in turn is

a favourable characteristic due to the inexact implementation of density functional theory in this thesis.

### 4.2.4 Exchange

This parameter was not modelled within this thesis. The author has seen pioneering work undertaking the accurate simulation of these parameters from a scattering theory regime [124, 125], but unfortunately there was not enough justification to ratify, implement, or extend the scattering theory implementation in to the work in this thesis. The figures for the exchange are reasonably consistent in the literature regarding the exchange parameter, common values used between $14^{-12}J/m$ and $30^{-12}J/m$, see the following for interest [126, 40, 127].

### 4.2.5 Anisotropy

Anisotropy in solid state physics has many different forms: magnetocrystalline anisotropy, interfacial anisotropy, shape anisotropy. Of these shape anisotropy is understood to be dependent on the macroscopic shape of the sample. The shape anisotropy is a side-effect of the minimisation of the demagnetising/magnetostatic field energy discussed in chapter 2. The magnetocrystalline anisotropy is also seen macroscopically, but its origins lie in a combination of the intrinsic angular momentum of the electrons and the crystal field. In most crystalline solids the orbital momentum of the electrons are quenched in bonding, but in the 3d ferromagnets it does remain after bonding. The relativistic effect of spin-orbit coupling irreducably couples the spin to the orbital momentum. The orbital momentum is directly related to the atomic structure of the crystal, and so we see anisotropy along the high symmetry lines of the crystal. Energy differences are typically of $\mu$eV/atom, orders of magnitude smaller than the total energy of a unit cell, but are macroscopically evident. At the time of writing, CASTEP did not have an implementation of

spin-orbit coupling, so self-consistent calculation could not be conducted using the plane-wave pseudopotential method.

### Magnetocrystalline Anisotropy

There have been a multitude of methods presented for calculating the magnetocrystalline anisotropy of a crystal from first principles [69, 128, 129, 130, 131, 36, 132]. For many years, the scientific community utilised the force theorem. In this a small perturbation of the final state is envisaged, eigenvalue sums evaluated, and then substracted from the original value. This type of measurement uses the force theorem [20]. With differences of energies of typically a few $\mu$ eV/atom, great care has to be taken to ensure confidence in the scientific method applied. Further details on convergence of systematic and cancellation of systematic errors are discussed in section 4.3.1. In ELK relativistic effects can be included self-consistently, so fully converged calculations can be conducted for the systems, without need for perturbation theory. However, the methods still subtracts values from each other to leave a figure orders of magnitude smaller. Other work has taken a different formalism for solving the electronic structure problem, scattering theory. The Korringa-Kohn-Rostocker (KKR) scattering theory has advantages that it can be more easily extended to non-zero temperatures via its Green's function origin and non-reliance on the ground state electron density. KKR also allows for the modelling of disorder via the use of potentials. Energetics and structural relaxations are key components of many DFT calculations, and KKR methods typically evaluate this poorly. In this thesis the ab-initio calculations are performed using DFT, and this work attempts to find the limitations in the predictions of the current DFT frameworks.

The presence of different atomic species, alloying, surfaces, and grain boundaries all have macroscopic affects on the anisotropy of a magnetic system. The anisotropy in cobalt platinum multilayers has been observed to be of the form

$$Kt \approx 2K_s + K_v t\,, \tag{4.6}$$

where $t$ is the thickness of the cobalt layer, and $K_s$ and $K_v$ are the surface/interface and volume energy-densities respectively. For thin cobalt layers the anisotropy is out of plane, but as the thickness of the cobalt layer increases the anisotropy switches to in-plane. This observation implies that the perpendicular orientation of the magnetisation is determined by the interface anisotropy.

Neel [133] first observed that the reduced symmetry at the surface could lead to enhanced anisotropy energy. Others have applied Brooks' itinerant model [134] for cubic anisotropy [135] to surfaces [136]. DFT calculations for the anisotropy of bulk crystals have been conducted from first-principles [137]. Calculations of isolated monolayers have been conducted and found to not always agree with experiment. The reasons for the discrepancies are not clear. Is the theory incomplete or is the experimental substrate affecting the results [138].

The Bruno model is an accessible theory [139]. It defines the magnetocrystalline anisotropy as follows:

$$\Delta E_{MAE} = \zeta[< \mathbf{L}.\mathbf{S} >_{hard} - < \mathbf{L}.\mathbf{S} >_{easy}] = \frac{\zeta}{4\mu_B}(\mu_L^{easy} - \mu_L^{hard}) > 0\,, \qquad (4.7)$$

where $\mu_L^{hard/easy}$ are the orbital magnetic moments in the hard/easy axis. The Bruno model suggests that the easy axis will align with the direction of maximum orbital magnetic moment.

Anisotropy values of two orders of magnitude greater than the bulk 3d ferromagnets have been observed in layered systems. Even today, the origin of the anisotropy measured in multilayers is not completely understood. Investigations have been performed in to the effect of structure [140], roughness [141], and interface mixing. This thesis concerns itself with fully self-consistent calculations of the anisotropy in a range of cobalt platinum systems, including multilayers.

In order to evaluate the anisotropy in the cobalt platinum systems the highest energy and lowest energy magnetisation directions are identified and subtracted from one

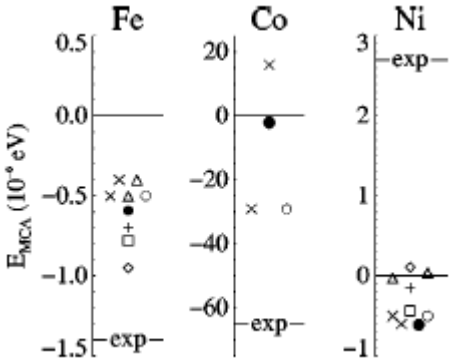


Figure 4-1: The magnetocrystalline anisotropy of BCC Fe, HCP Co, and FCC Ni. The experimental results (-exp-) are from [142]. . Stile's work is represented by black circle [143], [128] ×, [144] open circle, [36] diamond, [145] triangle, [146] square, and [147] plus symbol. After [132].

another

$$\Delta E_{MAE} = E_{max}(\theta) - E_{min}(\theta)\,. \tag{4.8}$$

As discussed, previous works typically use the force theorem [69] to do the calculation. Remember that the force theorem in this context states that the actual energy difference is comparable to the difference in band energies. This allows large simulations to be solved self-consistently once, and then the same density can just be reused in the new scenario to obtain an answer. However, this second answer is, generally, not self-consistent. Please note that in this thesis unless stated otherwise a fully converged self-consistent calculation is performed for a high symmetry direction. The output density from this calculation is then used to run another calculation. However, simulations using the force theorem contain only one iteration of the DFT code implementation is performed with the previous computation's starting density. This yields a non-self-consistent approximation for new energies, occupations and band energies. With modern computers and advanced computational techniques fully self-consistent simulations are possible in most regimes.

### 4.2.6 Micromagnetic Damping Parameter

The applicability of magnetic films for memory applications has led to an increase of interest in damping. The specific damping related to the equations of micromagnetics is magnetic precession damping. In micromagnetics this is the third term in this form of the LLG equation:

$$\frac{d\mathbf{M}}{dt} = -\gamma \left[\mathbf{M} \times \mathbf{H}_{eff}\right] + \frac{\alpha}{M_s}\left[\mathbf{M} \times M_s \frac{d\mathbf{M}}{dt}\right]. \tag{4.9}$$

The many possible contributions to the Gilbert damping parameter in micromagnetics are listed in to categories in figure 4-2. Of the direct sources, contributions to the damping through magnon-phonon coupling, itinerant electron relaxation, and crystal defects could be investigated by first principles. Magnon-phonon coupling is extremely computationally expensive and has only been investigated for pure metals. This is because the DFT unit cell is usually broken down in to a symmetric irreducible Brillouin zone. Often the k-points have symmetry about the $\Gamma$ [35] and other points, meaning that only a fraction of $k$-points have to be calculated. Magnon-phonon coupling combined with the spin-orbit coupling removes this computational nicety, leading to considerably longer computation times. The crystal defect contribution can be investigated for disordered alloys, but disordered multilayer unit cells would require too many atoms to be tractable. The itinerant electron relaxation models are thus the only models available, which would be simulative on a university-scale cluster computer.

The precession of the magnetisation will affect the filling of energy levels. A Fermi surface is a 3d representation of the familiar band structure. The first major investigations in to this were undertaken by Kambersky in [148]. Imagine majority and minority spin surfaces. In a crystal with spin orbit coupling effects there will be energy differences between the magnetisation directions. Therefore, as the magnetisation precesses, the Fermi surfaces will change shape, in order to ensure the energy is minimised. This could be as simple as an intraband transition, the electron stays

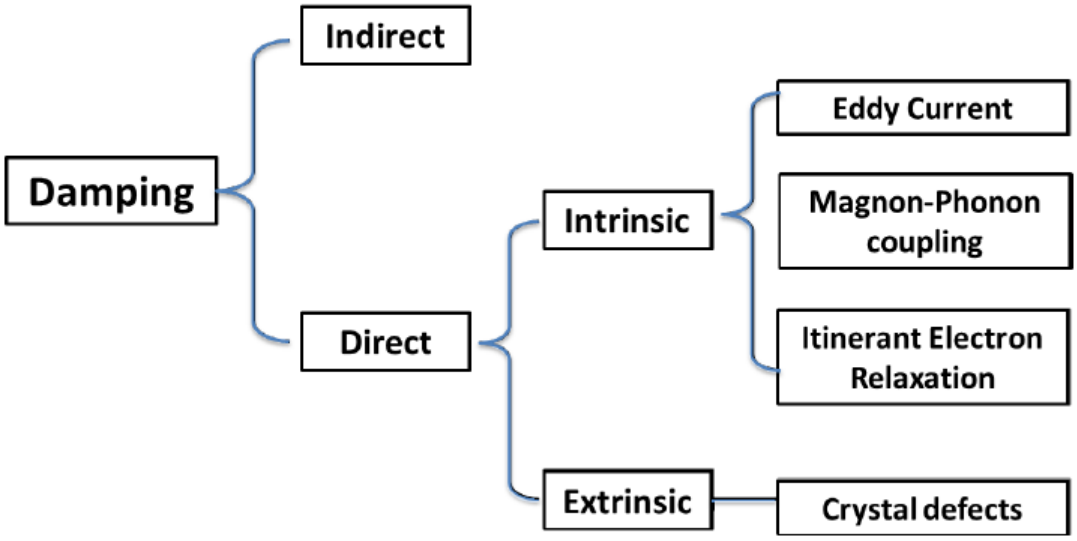


Figure 4-2: Classification of the types of damping exhibited in ferromagnets.

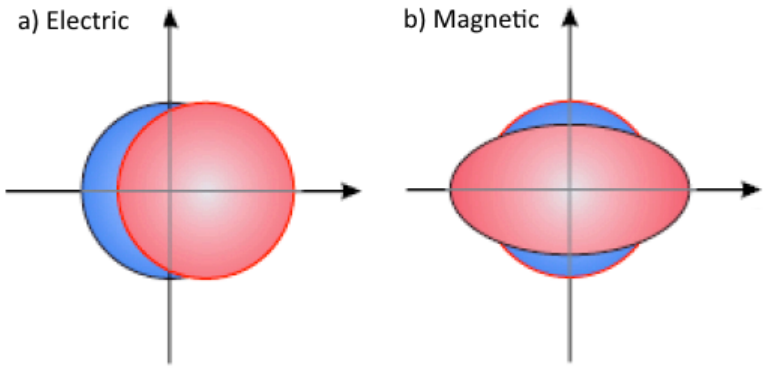


Figure 4-3: Fermi surface deformations.

within the band but has a different wavevector. Conversely, the electron may need to be excited and relax in to a different band with or without a different wavevector - an interband transition. These transitions are monikered *Breathing Fermi Surface* and *Bubbling Fermi Surface* effects [21]. Details on how to formalise these ideas, and methodology for ab initio values are presented in the following subsections.

**Breathing Fermi Surface**

Kambersky [149, 150, 151] attempted to describe the precession damping in terms of a lifetime approximation method and ab initio calculations. As the energy depends on the direction of magnetisation, the microscopic mechanism of population relaxation needed to be investigated. Remember that the 3d electrons are delocalised. It is therefore convenient to treat the electronic degrees of freedom about the Fermi energy as Bloch states [135].

The Bloch state energies $\epsilon_{\mathbf{k},\mu}$ are dependent on the magnetisation direction $\hat{m} = \mathbf{M}/M_s$ via dependence on spin orbit coupling, that is

$$\epsilon_{\mathbf{k},\mu} = \epsilon_{\mathbf{k},\mu}(\hat{m}) \,. \tag{4.10}$$

The effective field (in atomic units) was studied and reported in chapter 2, that is,

$$\mathbf{H} = -\frac{1}{M_s}\frac{\partial E}{\partial \hat{m}} \,. \tag{4.11}$$

In addition, the total electron energy density can be written

$$E = \Omega^{-1} \sum_{\mathbf{k},\mu} \epsilon_{\mathbf{k},\mu} n_{\mathbf{k},\mu} \,, \tag{4.12}$$

where the sum over $\mathbf{k}$ is a sum over the first Brillouin zone, and $\Omega$ is the volume of it, and n is the population. The population of the state can be approximated using the Fermi function, $f_\mu(\epsilon_\mu)$, and assigning a lifetime to the state, $\tau_\mu$. The population can thus be approximated as

$$n_\mu = f_\mu - \tau_\mu \frac{df_\mu}{dt} \,, \tag{4.13}$$

where the states are still k-dependent, but otherwise every term would carry the subscript too. The approximation is only valid for fast relaxation, relative to the

frequency of magnetic precession. This is valid for microwave frequencies and reasonably pure crystals at low temperatures. Mathematically, the approximation holds when

$$\tau_\mu \frac{df_\mu}{dt} << 1 \quad \text{and} \quad \tau_\mu \frac{d^2 f_\mu}{dt^2} << \frac{df_\mu}{dt} \,. \tag{4.14}$$

The variation of the energy density with the magnetisation direction $\hat{m}$ leads to the equation for an effective field:

$$\mathbf{H} = -(M_s \Omega)^{-1} \sum_{\mathbf{k},\mu} n_{\mathbf{k},\mu} \frac{\partial \epsilon_{\mathbf{k},\mu}}{\partial \hat{m}} + \epsilon_{\mathbf{k},\mu} \frac{\partial n_{\mathbf{k},\mu}}{\partial \hat{m}} \,. \tag{4.15}$$

Under the assumptions of the (BFS) Breathing Fermi Surface model, the second term can be neglected. This is because in this first treatment the system occupation is assumed not to change with magnetisation, and thus the occupation derivative with respect to magnetisation would be nil. Discussed in the following section, the second term denotes the excitation of electrons from lower to higher bands, creating electron-hole pairs. Note that the Fermi function is dependent on time as it is a function of the eigenvalues which are time-dependent. Therefore, using the chain rule the $i^{th}$ component of the effective field is

$$H_i = -(M_s \Omega)^{-1} \sum_{\mathbf{k},\mu} \tau_{\mathbf{k},\mu} \left( -\frac{\partial f_{\mathbf{k},\mu}}{\partial \epsilon_{\mathbf{k},\mu}} \right) \frac{\partial \epsilon_{\mathbf{k},\mu}}{\partial m_i} \frac{\partial \epsilon_{\mathbf{k},\mu}}{\partial m_j} \frac{dm_j}{dt} \,. \tag{4.16}$$

This field is theorised to be a significant contribution to the damping in the LLG equation. Therefore, if the form of the damping field (LL)

$$H_i = -\frac{\lambda}{(\gamma M_s)^2} \frac{dM_i}{dt} \tag{4.17}$$

is compared to the above formula then an expression for $\lambda$ can be found:

$$\frac{\lambda}{\tau} = \gamma^2 \Omega^{-1} \sum_{\mathbf{k},\mu} \left( \frac{\partial \epsilon_{\mathbf{k},\mu}}{\partial m_j} \right)^2 \delta(\epsilon_F - \epsilon_{\mathbf{k},\mu}) \,, \tag{4.18}$$

where $m_j$ is the magnetisation component perpendicular to the chosen magentisation state, $\mathbf{M}_0$. This simple equation does assume that the damping is isotropic,

and so can be treated as a scalar. Although it is well known the damping factor can be anisotropic and thus rigorous treatments require it to be modelled as a tensor. A final approximation that the derivative of the Fermi function can be equivalent to the dirac-delta function is:

$$-\frac{\partial f_\mu}{\partial \epsilon_\mu} \approx \delta(\epsilon_F - \epsilon_{\mathbf{k},\mu})\,. \tag{4.19}$$

The inverse of the lifetime $\tau^{-1}$ is a scattering frequency. If comparisons are made to the Drude model [35] for scattering of itinerant electrons, it can be seen that the at low temperature the damping parameter is proportional to the inverse square of the temperature. A low temperature increase in the damping of pure crystal nickel and cobalt has been seen using ferromagnetic resonance [152]. The formula for the damping parameter can also be derived using a linear-response formalism [150].

### Torque-Correlation Model

The BFS model only accounts for intraband transitions. In order to quantify the interband transitions, Kambersky started from Hamiltonians and torque-correlation [150]. The result is

$$\lambda = \frac{g^2\mu_B^2}{\hbar}\sum_{n,m}\int \frac{dk^3}{(2\pi)^3}|\Gamma^-_{nm}(k)|^2 W_{nm}(k)\,, \tag{4.20}$$

where transitions between bands m and n induced by the spin-orbit interaction are measured by

$$\Gamma^-_{nm}(k) = \langle n,k|[\sigma^-, H_{SO}]|m,k\rangle\,, \tag{4.21}$$

the scattering events are weighted by the spectral overlap

$$W_{nm}(k) = \frac{1}{\pi}\int d\omega_1 \eta(\omega_1) A_{nk}(\omega_1) A_{mk}(\omega_1)\,, \tag{4.22}$$

$A_{nk}$ are Lorentzians broadened by lattice interactions positioned about the band energy $\epsilon_{nk}$. The damping from the torque-correlation model can be regarded as the ratio of the complex to real frequency components of a spin-orbit damped spin wave.

The torque-correlation model has been applied to the 3d ferromagnets. BCC iron, HCP, cobalt, and FCC nickel have been modelled by Gilmore *et. al.*[21]. Their results are shown in figure 4-4. They present values for the Landau-Lifshitz and Gilbert damping parameters in terms of the scattering rate $1/\tau$ and equivalent energy $\hbar/\tau$. Contributions from the intraband and interband transitions are shown. The values predicted by ab-initio calculations are of the same order of magnitude as the experimentally measured values. For HCP cobalt, the measured value is two times larger than the predicted value. Nowhere in the derivation of the theory were the Fermi surface deformations apportioned as the entirety of the damping in the pure crystal. Therefore, a result of a the same order of magnitude but less than the measured value is extremely encouraging. However, the damping could actually be dominated by the Fermi surface deformations, and systematic errors in the first-principles calculation could be the issue. In the results section the values for the 3d ferromagnets are calculated using the ELK package.

## 4.3 Results

Results for electronic structure investigations in to cobalt platinum systems are now presented. Starting with examples of general convergence critera, results are then presented for pure metals, alloys, 'disordered' alloys, low-dimensional cobalt, and cobalt platinum multilayers. The lattice constant, magnetic moment, polarisation are presented. Where calculable, electronic structure calculations for Fermi surface contributions to the Fermi surface are included, and comparisons made to prior published work.

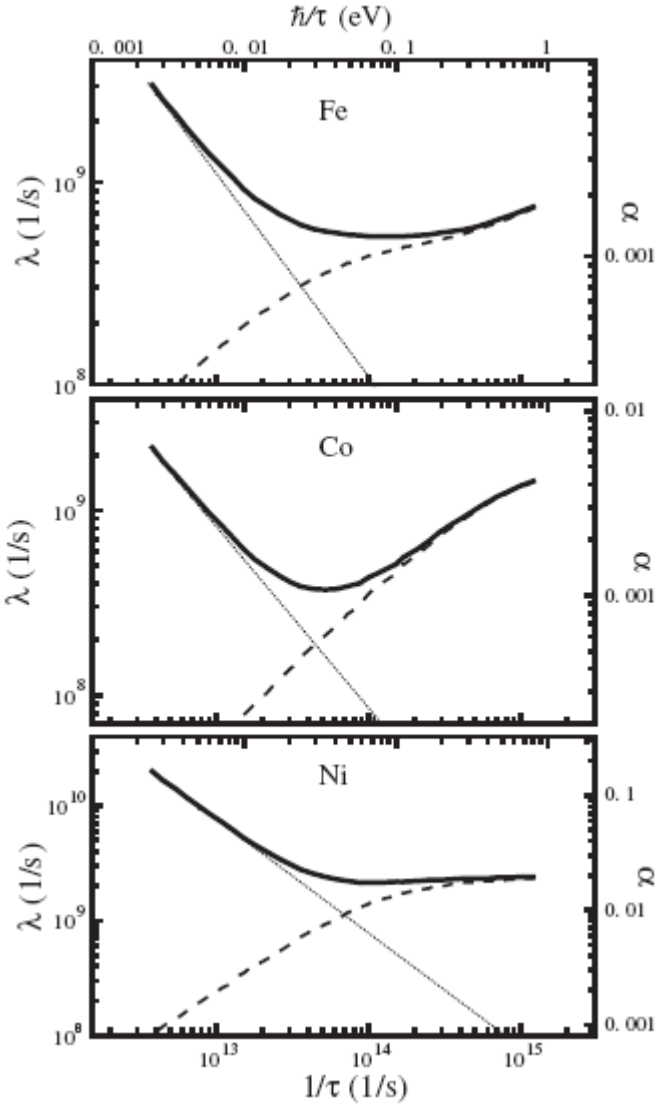


Figure 4-4: Gilbert and Landau-Lifshitz damping parameters calculated for iron, cobalt, and nickel. The solid curves denote the result, and the dotted and dashed lines represent the contributions from intraband and interband transitions respectively. The scattering parameter is sometimes converted to an energy and this is shown on the top x axis. Figure and caption reproduced from [21].

Table 4.1: Cobalt: The lattice constants (in angstroms) and magnetic moments (in $\mu_B$) for Co.

| Type | Method | Lattice Constant | $\mu$(Co) |
|---|---|---|---|
| Expt | | 3.550 | 1.57 (spin only) 1.70 (total) |
| CASTEP | OTF PseudoPot LDA | 3.454 | 1.686 |
| CASTEP | New PseudoPot LDA | 3.503 | 1.636 |
| ELK | LDA no SOC | castep | 1.59 |
| CASTEP | OTF PseudoPot PBE | 3.551 | 1.806 |
| CASTEP | New PseudoPot PBE | 3.618 | 1.758 |
| ELK | PBE no SOC | castep | 1.72 |
| ELK | LDA no SOC | 3.423 | 1.52 |
| ELK | LDA inc SOC | 3.423 | 1.53 |
| ELK | PBE no SOC | 3.521 | 1.65 |
| ELK | PBE inc SOC | 3.521 | 1.65 |
| CASTEP | OTF PseudoPot LDA | 3.550 (expt) | 1.756 |
| CASTEP | New PseudoPot LDA | 3.550 (expt) | 1.664 |
| ELK | LDA no SOC | 3.550 (expt) | 1.61 |
| CASTEP | OTF PseudoPot PBE | 3.550 (expt) | 1.804 |
| CASTEP | New PseudoPot PBE | 3.550 (expt) | 1.708 |
| ELK | PBE no SOC | 3.550 (expt) | 1.67 |

### 4.3.1 Note on Convergence

In chapter 3 parameters were identified that electronic structure calculations should be converged against. Some of these parameters are implementation and system dependent. For example, a three-dimensional unit cell intended to simulate a single layer of platinum needs to have enough padding vacuum layer so that the wavefunctions cannot interact. Care and many shell scripts have been used to iterate parameter space. Examples of convergence have been included in the results following. It is intended that errors and discrepancies between prior published work and experiments will be systemic errors.

### 4.3.2 Pure Metals

After multiple convergence tests were performed for the standard cobalt and platinum systems in CASTEP and ELK simulations on the ordered alloys were per-

formed. The band structures all showed generally good agreement. The spin splitting of the bands about the Fermi energy was reasonably consistent, and this is a criterion expected to see from the Stoner theory of band ferromagnetism. ELK generally provided lower magnetic moments than the CASTEP code, and this was attributed to the FLAPW technique's inherent ability to treat with magnetic systems. The magnetic moment's reliance on lattice constant was charted, to check if CASTEP's inconsistency with prior published work was due to its (<5%) reasonable error in evaluating the lattice constants. From the plots of the variation of the magnetic moment, and the values given in table 4.3.2, it was thus decided that CASTEP's treatment of cobalt and platinum were not accurate enough to use it to parametrise interactions. ELK's predicted magnetic moments were then calculated and these were found to be in a much better general agreement with prior published work, experimental and theoretical. To aid in the comparison of all of the data sets the code packages were each employed to evaluate spin moments at their predicted equilibrium lattice constant, and to those of experimental studies. In both cases there are discrepancies, but ELK appears to treat the systems quantitatively more accurately than CASTEP. This might be expected from the fewer assumptions made in the qualitative model, but comes at great cost of efficiency. Using a code package that currently implements the spin orbit interaction, however, does allow for more micromagnetic parameters to be computed. Furthermore , note that these calculations are complicated by the fact that the magnetic moment of cobalt induces one in the subsequent platinum atoms.

**Platinum**

Initial calculations were conducted on FCC platinum. Platinum is non-magnetic, and DFT functional calculations confirm spin degeneracy: no intrinsic spin magnetic moment is exhibited. It was found that purely non-relativistic calculations are likely insufficient to model platinum. Overestimations are evident when compared to prior published work in the literature, with a poor description of the sp-hybridised band. Therefore, it was found that at least a scalar-relativistic description was required to correctly describe crystalline platinum atoms.

### Cobalt

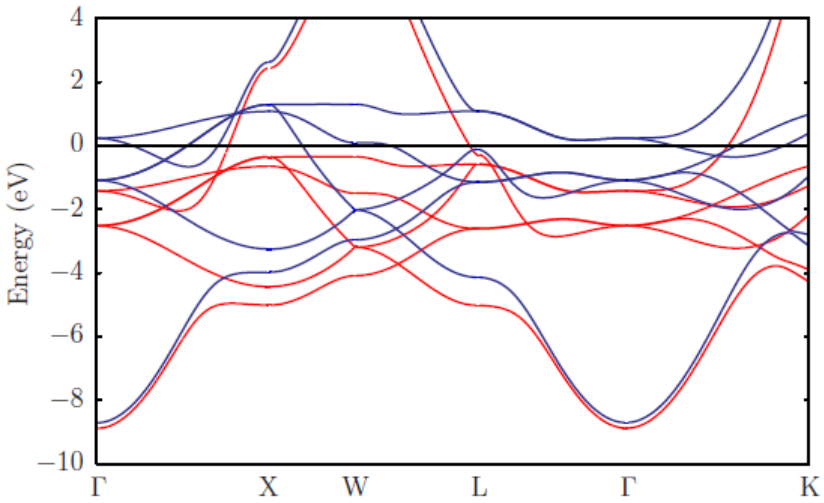


Figure 4-5: FCC Co band structures through the high symmetry points and lines. Different colours denote opposite spin polarisation.

Bulk cobalt exists naturally in the HCP and FCC phases. HCP cobalt is energetically preferable, but room temperature provides enough energy to overcome this barrier. This thesis is primarily concerned with evaluating and confirming the properties of FCC cobalt and (111) stacking, as these are relevant to the multilayer structures used experimentally that motivated this work. FCC cobalt is studied in particular, as platinum for all intents and purposes is FCC. Calculations are performed where FCC platinum is modelled, and substitutional cobalt atoms are inserted. Lattice constants are relaxed and atomic locations are not fixed. However, for symmetry reasons, it is only when we have a planar surface we generally observed atomic relaxation. For example, a layer of cobalt adjacent to a layer of platinum would neither have the cobalt-cobalt nor platinum-platinum interlayer spacing. CASTEP has a built in solver that can identify local minima in the energy landscape by performing self-consistent calculations and estimating the forces on the atoms. In ELK a more basic approach is used. Calculations at experimental and CASTEP lattice constants are performed, and then a simple linear mixing of the calculated energies and lattice constants is used to estimate where a local minimum might be.

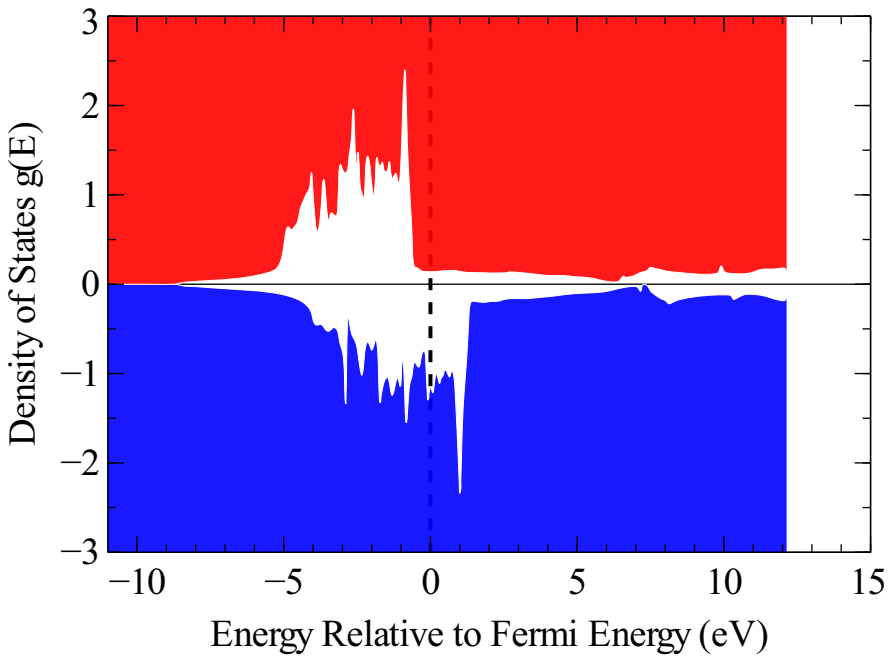


Figure 4-6: FCC Co density of states showing the majority (red outset) and minority (blue outset). The peaks of the density of states are artificially smoothed by small Gaussians (0.1eV *FWHM*- full-width at half-maximum) in order to make $g(E)$ more continuous and representative of real systems.

Table 4.3.2 demonstrates a whole range of magnetic moments for cobalt at a wide-range of lattice constants. It is worth noting that the spin-only magnetic moment is reported as well as the total magnetic moment. The magnitude of the magnetic moment is not greatly affected by the inclusion of spin-orbit coupling, but the orbital moment itself does make a significant contribution to the observed total magentic moment, approximately 9%. Values of the magnetic moment are presented for the PBE (Perdew-Burke-Ernzerhoff) [153] implementation of the exchange-correlation potential in the flavour of a GGA (generalised-gradient approximation). Remember that some magnetic properties are poorly represented by the LDA [154], with the ground-state of iron incorrectly determined (LSDA in spin-polarised systems).

The magnetic moment is heavily reliant on the lattice constant. Figure 4-11 shows the reliance of the magnetic moment on the lattice constant. An approximately linear relationship can be seen close to the equilibrium lattice constant, but of course

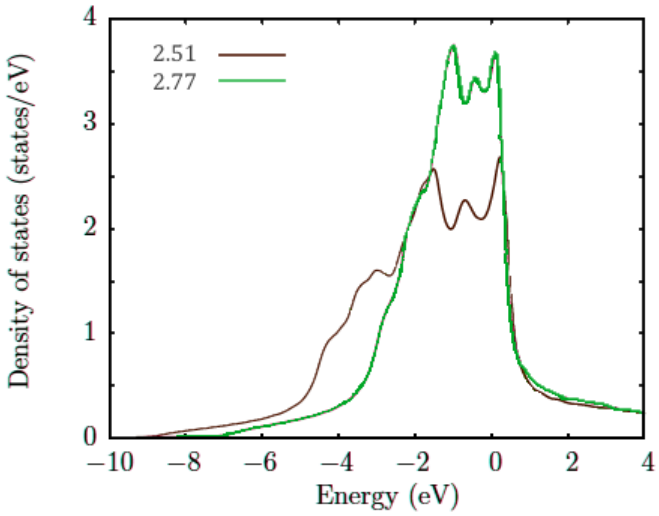


Figure 4-7: Density of states of FCC cobalt. The two different lines illustrate the change with lattice constant, and the flattening of the cobalt bands if cobalt is forced to adopt platinum's lattice parameter. Note that the Fermi energy is defined as 0 eV.

this relationship is no longer valid for a wider range of lattice constants, generally within 10% of the equilibrium value. As the lattice constant increases the cobalt bands flatten. Figure 4-7 shows how the band flattening leads to higher peaks in the density of states. The exchange is still present and strong at lattice constants up to the value of the platinum lattice constant, so the 3d bands become even narrower. This in turn makes it more likely that an even higher proportion of the majority states are occupied, increasing the magnetic moment. The density of states are plotted by smearing the zero-temperature states in order to provide a more continuous and useful measure. A sensible choice of the smearing factor does not greatly affect the polarisation, even though this is directly dependent on the amplitude at the Fermi energy. This is because the majority and minority bands are smeared equally. Differences might be observable when comparing smeared data with the raw output data. This is because the raw data could have a disproportionately large peak at the Fermi energy, which is then sensibly smeared around it.

The density of states at the Fermi energy is the measure being used to identify the spin-polarisability of the system. The band-resolved density of states shown in figure 4-8. This shows that near the Fermi energy it is indeed the d electrons that

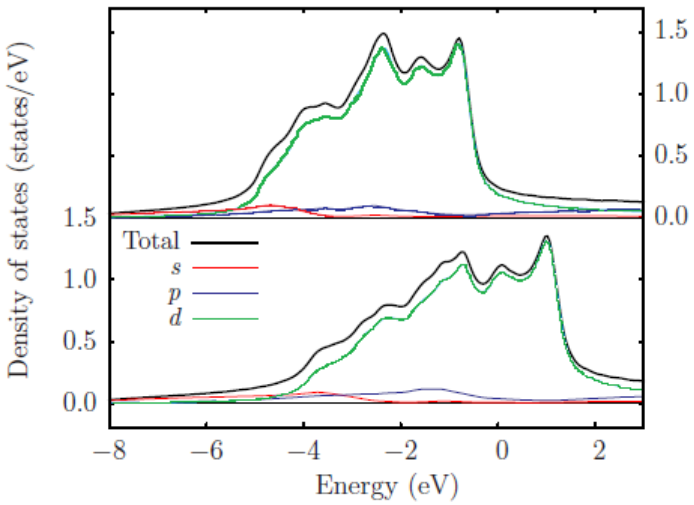


Figure 4-8: Majority/minority band resolved density of states of FCC cobalt. The different lines represent the different electron quantum numbers and the total is also represented. The top section represent the majority density of states and beneath the minority density of states. A Gaussian broadening parameter of 0.15 eV is used to round the densities. Note that the Fermi energy is defined as 0 eV.

are present in affecting the properties of the system.

The summarial table 4.6 demonstrates the calculated polarisation, saturation magnetisation, and Gilbert damping parameters for bulk FCC cobalt.

### Damping Parameter in Cobalt, Iron, and Nickel

The work by Gilmore [21] *et. al.*was repeated using the ELK implementation. ELK is based on the same theory as Gilmore's group. In our calculations 120x120x69, 150x150x150, and 120x120x120 k-points were used similar to Gilmore's group. This is an extremely large number of k-points. More points are required as the *eigenvalue* convergence needs to be tight enough to allow for energy differences of magnitudes less than the magnetocrystalline anisotropy.

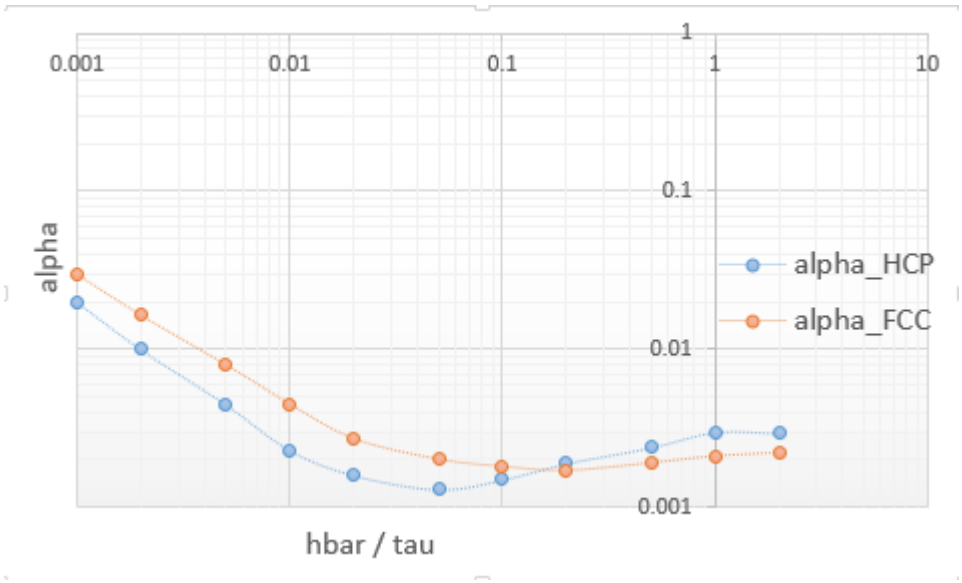


Figure 4-9: Gilbert damping parameter plotted as a function of the scattering rate. All calculations are for the bulk 3d ferromagnets in their equilibrium phases: BCC Fe, HCP Co, and FCC Ni.

The torque-correlation formula 4.20 is specific to three-dimensions. A similar formula can be derived for two-dimensional crystals. This formula is presented in equation (4.23).

### 4.3.3 Alloys

#### CoPt, $Co_3Pt$, and $CoPt_3$

Instead of thinking of FCC cobalt as a primitive unit cell. We can imagine the FCC crystal using a simple cubic unit cell with four atoms in a unit. cell. The bottom-left vertex of the cube, simple cubic lattice vectors, and the three adjacent face atoms form a new unit cell. The ordered alloys hail from substitutions of the vertex and face atoms, e.g. one cobalt vetex, three platinum face atoms is $Co_1Pt_3$. Convergence of the structure was conducted for the 3 different alloy types. CoPt required more

work, as the repeatable layering caused reasonable geometry relaxations. $Co_2Pt_2$ is this regard could essentially be regarded as $Co_1Pt_1$ multilayers. The cobalt and platinum layers relax to find their equilbrium spacing. As the interface anisotropy appears to be dominant term in the anisotropy in the multilayers, the $Co_1Pt_1$ toy system should set an upper bound for the anisotropy calculations.

Table 4.2: The lattice constants (in angstroms) and magnetic moments (in $\mu_B$) for $Co_3Pt$.

| Type | Method | Lattice Constant | $\mu_{tot}$ | $\mu$(Co) | $\mu$(Pt) |
|---|---|---|---|---|---|
| thry[155] | LMTO ASA (Barth-Hedin XC) | 3.6636[156] | 5.54 | 1.39 | 0.38 |
| thry[157] | ASW LSDA | 3.6636[156] | 5.28 | 1.64 | 0.36 |
| thry[158] | LMTO LSDA | 3.668(expt - no ref) | e 5.24 | 1.6379 | 0.3153 |
| CASTEP | OTF PseudoPot LDA | 3.598 | 5.852 | 1.82 | 0.40 |
| CASTEP | New PseudoPot LDA | 3.572 | 5.384 | 1.68 | 0.32 |
| ELK | LDA no SOC | castep | 4.96 | 1.57 | 0.37 |
| CASTEP | OTF PseudoPot PBE | 3.692 | 6.235 | 1.96 | 0.36 |
| CASTEP | New PseudoPot PBE | 3.667 | 5.900 | 1.86 | 0.30 |
| ELK | PBE no SOC | castep | 5.70 | 1.82 | 0.40 |
| ELK | LDA no SOC | 3.565 | 4.92 | 1.55 | 0.36 |
| ELK | PBE no SOC | 3.666 | 5.70 | 1.82 | 0.40 |
| CASTEP | OTF PseudoPot LDA | 3.6636[156] | 5.913 | 1.83 | 0.41 |
| CASTEP | New PseudoPot LDA | 3.6636[156] | 5.499 | 1.72 | 0.34 |
| ELK | LDA no SOC | 3.6636[156] | 5.46 | 1.72 | 0.41 |
| CASTEP | OTF PseudoPot PBE | 3.6636[156] | 6.178 | 1.95 | 0.35 |
| CASTEP | New PseudoPot PBE | 3.6636[156] | 5.883 | 1.85 | 0.30 |
| ELK | PBE no SOC | 3.6636[156] | 5.69 | 1.82 | 0.40 |

CASTEP was used to attempt to simulate the properties of bulk cobalt, platinum, and the ordered FCC $Co_xPt_{4-x}$ structures. The pseudopotentials energy cut-off had to be checked for energy convergence. Other calculation parameters that need converging are the number of plane waves and the $k$-point sampling. A sample of these calculations can be seen in figure (3-3).

It was found that CASTEP significantly overestimated the spin magnetic moments of the ordered cobalt platinum alloys (see tables below). Courtesy of my supervisor's previous communications with one of the authors of CASTEP, it was concluded that to increase the accuracy of the calculations, semi-core states should be included in the pseudopotential. These are the states in the shell just below the valence shell, and in the case of cobalt are the 3s and 3p channels. This helped to reduce the overestimate, but not as much as was hoped prior to the commencement of calculations.

Table 4.3: The lattice constants (in angstroms) and magnetic moments (in $\mu_B$) for CoPt.

| Type | Method | Lattice Constants | c/a | $\mu_{tot}$ | $\mu$(Co) | $\mu$(Pt) |
|---|---|---|---|---|---|---|
| thry[159] | FP-LMTO LSDA | - | - | e 2.16 | 1.79 | 0.37 |
| thry[157] | ASW LSDA | 3.793 3.675[160] | 0.969 | 2.06 | 1.69 | 0.37 |
| thry[155] | ASW LMTO (Barth-Hedin XC) | 3.803 3.701[156] | 0.973 | 2.215 | 1.85 | 0.38 |
| thry[161] | FP-LMTO LSDA | 3.806 3.684[159] | 0.968 | e 2.09 | 1.74 | 0.35 |
| thry[161] | FP-LMTO GGA | 3.806 3.684[159] | 0.968 | e 2.40 | 1.83 | 0.37 |
| thry[162] | Spin Pol TB | - | - | e 2.06 | 1.69 | 0.37 |
| expt[163] | Xray Diffraction | 3.786 3.685 | 0.973 | no access | to PDF | - |
| expt[159] | Xray Magc Circ Dichrsm | - | - | e 2.11 | 1.76 | 0.35 |
| expt[164] | Neutron Scattering | - | - | e 1.95 | 1.70 | 0.25 |
| CASTEP | OTF PseudoPot LDA | 3.747 3.651 | 0.974 | 2.370 | 1.96 | 0.40 |
| CASTEP | New PseudoPot LDA | 3.735 3.617 | 0.968 | 2.196 | 1.84 | 0.36 |
| ELK | LDA no SOC | castep | | 2.11 | 1.73 | 0.42 |
| CASTEP | OTF PseudoPot PBE | 3.828 3.750 | 0.980 | 2.495 | 2.12 | 0.38 |
| CASTEP | New PseudoPot PBE | 3.819 3.715 | 0.973 | 2.392 | 2.04 | 0.36 |
| ELK | PBE no SOC | castep | | 2.28 | 1.93 | 0.42 |
| ELK | LDA no SOC | 3.738 3.614 | 0.967 | 2.11 | 1.73 | 0.42 |
| ELK | PBE no SOC | 3.815 3.713 | 0.973 | 2.20 | 1.83 | 0.42 |
| CASTEP | OTF PseudoPot LDA | 3.803 3.701[156] | 0.973 | 2.403 | 1.97 | 0.40 |
| CASTEP | New PseudoPot LDA | 3.803 3.701[156] | 0.973 | 2.251 | 1.86 | 0.36 |
| ELK | LDA no SOC | 3.803 3.701[156] | 0.973 | 2.20 | 1.83 | 0.42 |
| CASTEP | OTF PseudoPot PBE | 3.803 3.701[156] | 0.973 | 2.478 | 2.12 | 0.37 |
| CASTEP | New PseudoPot PBE | 3.803 3.701[156] | 0.973 | 2.383 | 2.03 | 0.36 |
| ELK | PBE no SOC | 3.803 3.701[156] | 0.973 | 2.27 | 1.91 | 0.42 |

ELK was implemented to attempt to simulate the properties of bulk cobalt, platinum, and the ordered FCC $Co_xPt_{4-x}$ structures. Again, as with all simulations parameters such as K-point mesh density and plane wave energy cut-off need to be converged in order to make sure that the code's predictions are as indicative as possible.

**'Disordered Alloys'**

Razee *et. al.*[36] performed the first first-principles calculations of disordered cobalt platinum alloys. Their implementation utilised the KKR method [107, 170] and the coherent potential approximation (CPA) [171, 172, 173]. This method investigates the Green's function of a system. Typically, this involves replacing a disordered

[1]The sample used was of the form $CoPt_{3.02}$ with 0.2% impurity content

Table 4.4: The lattice constants (in angstroms) and magnetic moments (in $\mu_B$) for $CoPt_3$.

| Type | Method | Lattice Constant | $\mu_{tot}$ | $\mu$(Co) | $\mu$(Pt) |
|---|---|---|---|---|---|
| thry[161] | Full-Pot LMTO LSDA | 3.857[165] | e 2.48 | 1.82 | 0.22 |
| thry[161] | Full-Pot LMTO GGA | 3.857[165] | e 2.61 | 1.89 | 0.24 |
| thry[166] | ASW LMTO LSDA | - | e 2.44 | 1.66 | 0.26 |
| thry[167] | ASA LMTO inc SOC | - | 2.727 | 1.796 | 0.238 |
| thry[157] | ASW LSDA | 3.8540[168] | 2.50 | 1.69 | 0.27 |
| thry[155] | LMTO ASA (BH XC) | 3.8310[156] | 2.59 | 1.85 | 0.25 |
| thry[169] | FLAPW LSDA | 3.8735 (calc) | e 2.6 | 1.7 | 0.3 |
| thry[162] | Spin Pol TB | - | e 2.5 | 1.69 | 0.27 |
| thry[158] | LMTO LSDA | 3.831 (expt - no ref) | e 2.43 | 1.7079 | 0.2384 |
| expt[164] | Neutron Scattering | -[1] | $2.43 \pm 0.03$ | $1.64 \pm 0.04$ | $0.26 \pm 0.02$ |
| CASTEP | OTF PseudoPot LDA | 3.812 | 2.902 | 2.06 | 0.28 |
| CASTEP | New PseudoPot LDA | 3.802 | 2.665 | 1.94 | 0.24 |
| ELK | LDA no SOC | castep | 2.54 | 1.77 | 0.27 |
| CASTEP | OTF PseudoPot PBE | 3.894 | 3.261 | 2.24 | 0.34 |
| CASTEP | New PseudoPot PBE | 3.885 | 3.069 | 2.16 | 0.30 |
| ELK | PBE no SOC | castep | 2.97 | 2.02 | 0.33 |
| ELK | LDA no SOC | 3.804 | 2.54 | 1.78 | 0.27 |
| ELK | PBE no SOC | 3.885 | 2.97 | 2.02 | 0.35 |
| CASTEP | OTF PseudoPot LDA | 3.8310[156] | 2.998 | 2.08 | 0.29 |
| CASTEP | New PseudoPot LDA | 3.8310[156] | 2.802 | 1.99 | 0.27 |
| ELK | LDA no SOC | 3.8310[156] | 2.61 | 1.82 | 0.28 |
| CASTEP | OTF PseudoPot PBE | 3.8310[156] | 3.044 | 2.14 | 0.30 |
| CASTEP | New PseudoPot PBE | 3.8310[156] | 2.937 | 2.07 | 0.29 |
| ELK | PBE no SOC | 3.8310[156] | 2.83 | 1.94 | 0.28 |
| CASTEP | OTF PseudoPot LDA | 3.857[165][161] | 3.103 | 2.19 | 0.30 |
| CASTEP | New PseudoPot LDA | 3.857[165][161] | 2.936 | 2.13 | 0.27 |
| CASTEP | OTF PseudoPot PBE | 3.857[165][161] | 3.189 | 2.19 | 0.33 |
| CASTEP | New PseudoPot PBE | 3.857[165][161] | 2.994 | 2.12 | 0.29 |

solid's array of variable potentials with effective potentials considered to be inhabiting an ordered lattice. Key results in the paper are for the temperature-dependence of the anisotropy in the disordered alloys. The implementation used in this thesis is ground-state only, so only as an interesting thought experiment should results be extrapolated as such. Small finite 'temperatures' are used to smear the density of states, as otherwise it can be extremely discrete, leading to computational difficulties.

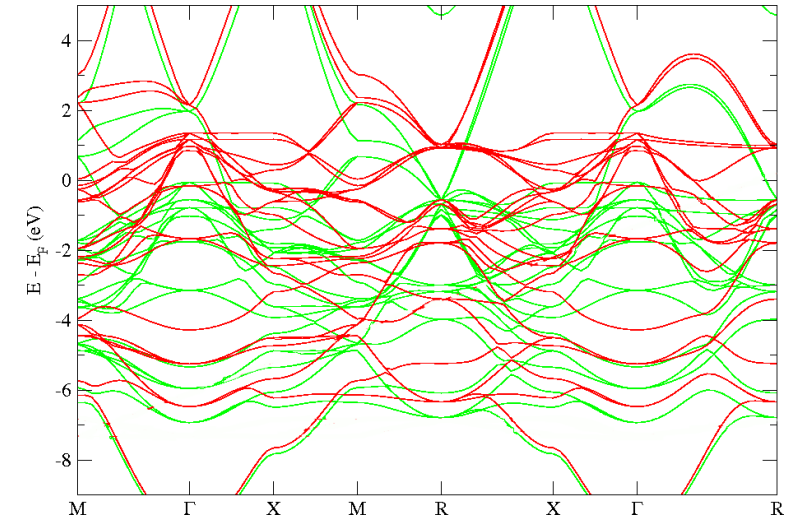


(a) CASTEP

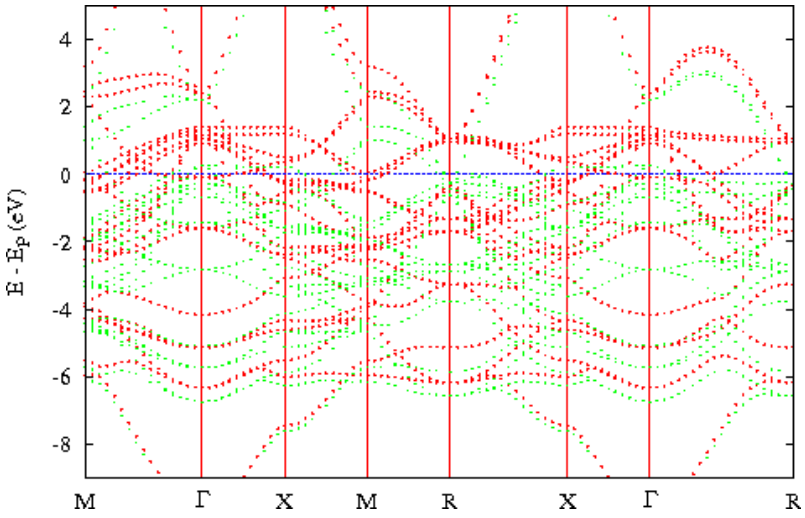


(b) ELK

Figure 4-10: FCC $Co_3Pt$ band structures through the high symmetry points and lines. Different colours denote opposite spin polarisation. At the Fermi energy a splitting of approximately 1 eV can be seen in both code packages. Both computations utilise the LDA approximation, and are non-relativistic.

### 4.3.4 Thin Films

Theory and lack of experimental evidence suggests that no crystals exist natively in 2D without a substrate of some sort. Reference should be given to the Mermin-

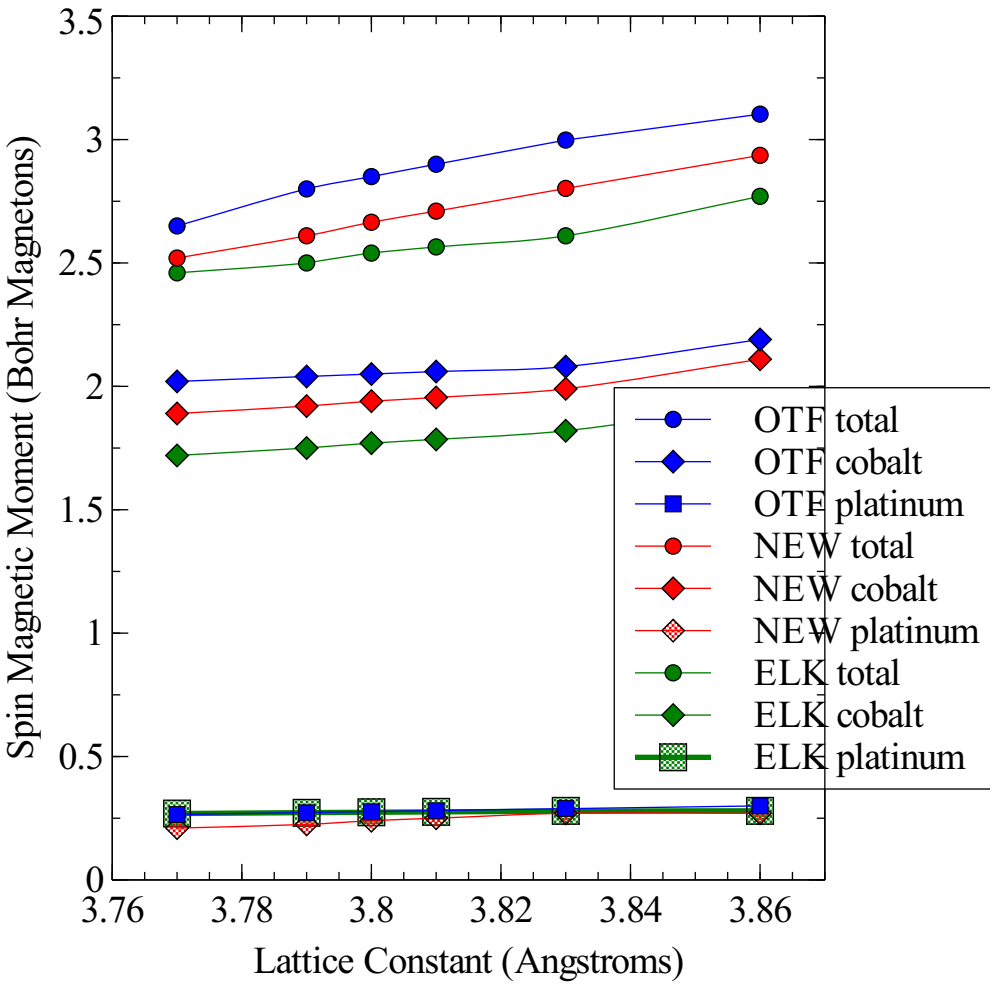


Figure 4-11: The total, cobalt, and platinum magentic moments of atoms in the ordered $CoPt_3$ alloy. OTF and NEW denote the default CASTEP pseudopotential, and the CASTEP pseudopotential with added semicore states. ELK results are shown for comparision. All results were obtained using the LDA for the exchange-correlation potential. See table 4.4 for the source of the data.

Wagner theorem [174]. Even the cobalt platinum multilayers examined in this thesis would experimentally exist upon a silicon substrate. The substrate can be used to affect the properties of the system favourably, silicon dioxide can be used to open a band gap in graphene [175]. However, care is normally taken for the substrate to not influence the material. Simulations were performed on isolated cobalt layers *gedanken* - as an insight in to the differences that the surrounding platinum layers contribute to the properties of cobalt platinum multilayers.

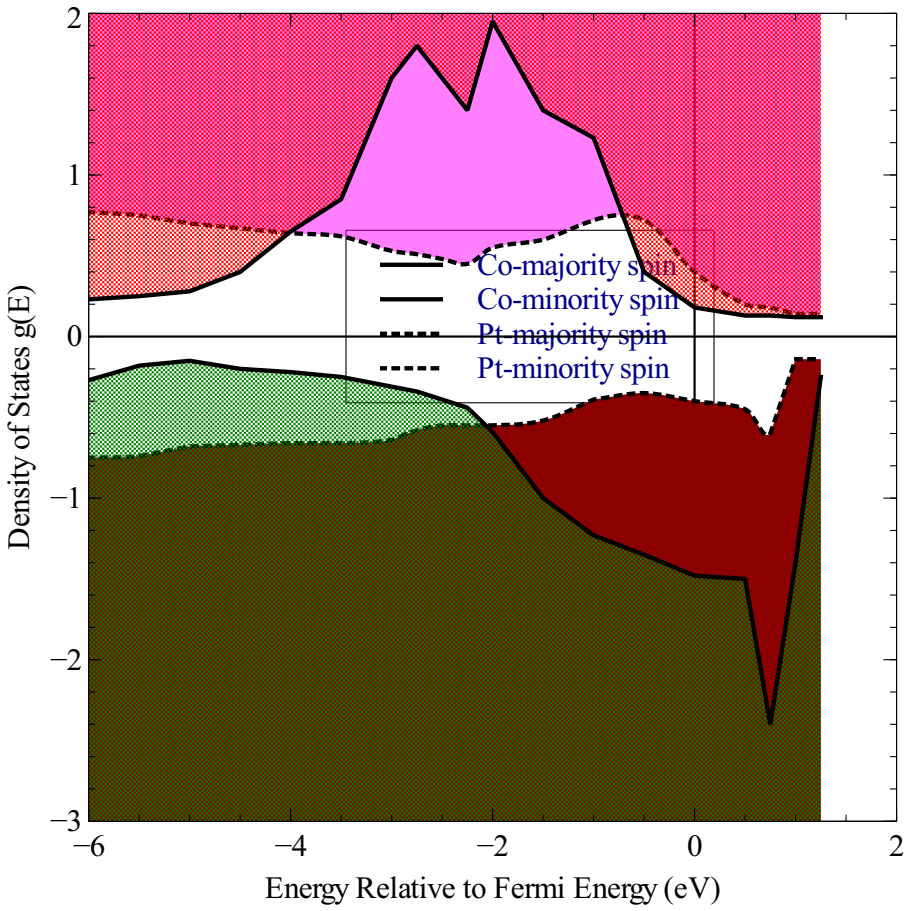


Figure 4-12: Rework of work presented by Razee *et. al.*[36] The density of states is plotted for ordered CoPt alloy. The majority and minority spin components for platinum and cobalt are included. The solid line (above) below the axis shows the (majority) minority density of states, and the dashed line is a similar representation of the density of states for platinum.

Within the film geometry the computation of the damping parameter could be undertaken. Equation 4.20 previously presented for the torque-correlation model is for three-dimensional systems. Following on from the aforementioned equation, the damping term in two-dimensions can be written

$$\alpha = \frac{\pi a_{2d}^2}{N_{Co}\mu_s} \sum_{n,m} \int \frac{dk}{4\pi^2} |\Gamma_{nm}(\mathbf{k})|^2 W_{nm}(\mathbf{k}) \,. \tag{4.23}$$

Here the integration is done over reciprocal space, $a_{2d}$ is the in-plane lattice constant,

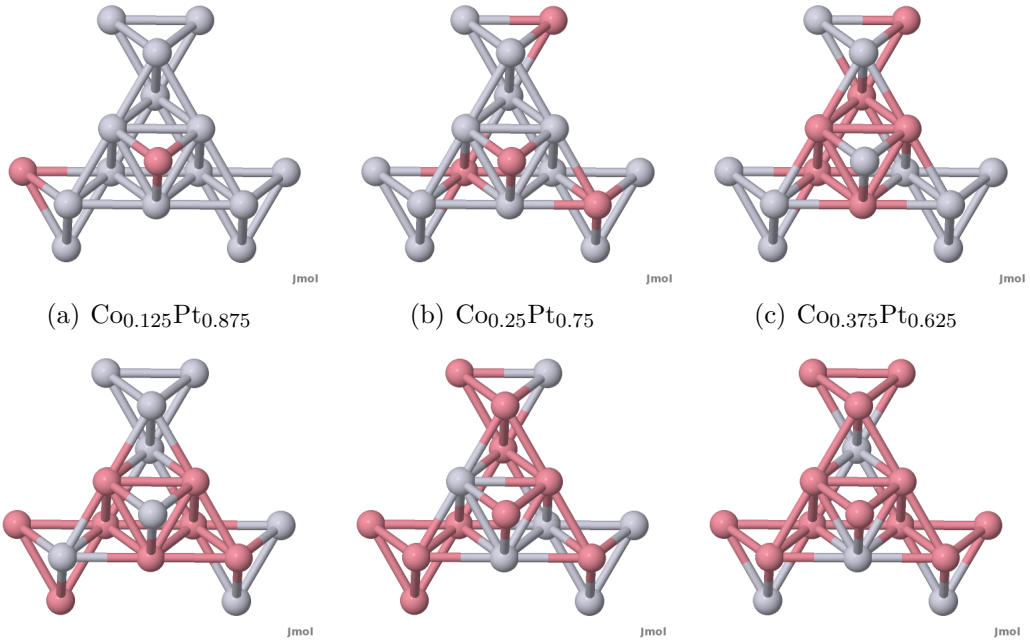

(a) $Co_{0.125}Pt_{0.875}$ (b) $Co_{0.25}Pt_{0.75}$ (c) $Co_{0.375}Pt_{0.625}$

(d) $Co_{0.5}Pt_{0.5}$ (e) $Co_{0.625}Pt_{0.375}$ (f) $Co_{0.75}Pt_{0.25}$

Figure 4-13: Examples of disordered versions of the $Co_xPt_{4-x}$ alloys with the amount of cobalt and platinum in the alloy proscribed in the subfigure caption. These, although technically ordered, alloys are used to approximate more disordered cobalt platinum alloys.

$\mu_s$ is the magnetic moment in Bohr magnetons , and $N_{Co}$ is the atom count.

### Co Monolayer

Miranda *et. al.*have studied experimentally the band structure of a cobalt monolayer deposited on a copper surface [176]. These investigations are interesting to theorists as the experimental band structure shows that the copper surface band structure and d-waves appear to be unaffected by the presence of the cobalt. This allows experimentalists to attempt to probe (seemingly) isolated monolayers of cobalt for their properties. Unfortunately Miranda *et. al.*did not manage to measure the magnetic moment, but they confirmed that the exchange splitting of the monolayer (0.80 eV $\pm$ 0.12 eV) was close to the bulk value of 0.9 eV. The work conducted on

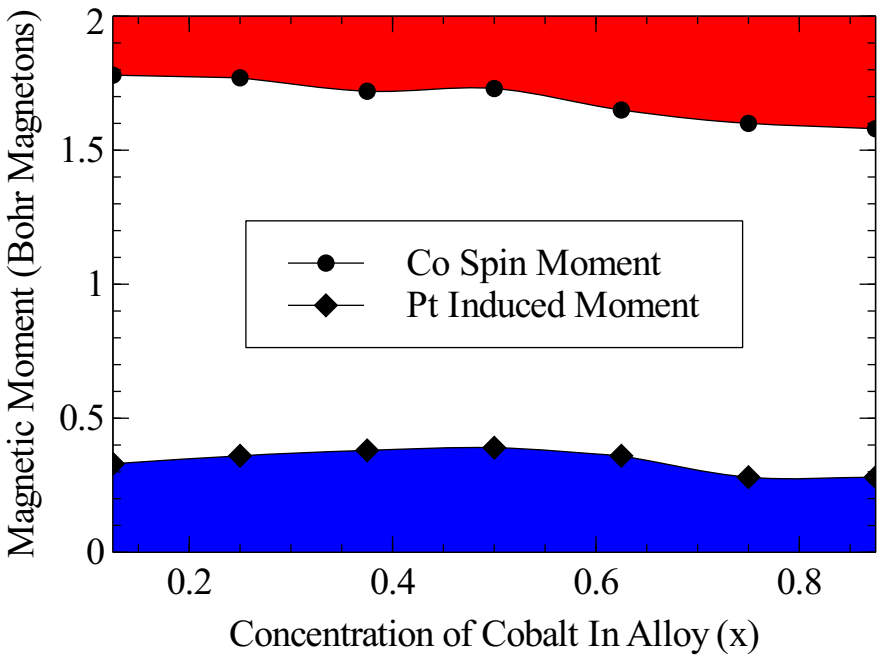


Figure 4-14: The calculated magnetic moments for the 'disordered' cobalt platinum alloys shown in figure (4-13). Note that the cobalt moment decreases approximately linearly from the free space value to the bulk value, whereas the induced platinum moment appears to peak around the 50% concentration.

low-dimensional cobalt in this thesis is intended to demonstrate that the interesting properties of cobalt platinum multilayers have their origin in the cobalt/platinum surface, compared to the thickness of the cobalt layers. Note that Miranda's work was performed on a HCP-Co(0001) monolayer, which would be equivalent to a FCC-Co(111) monolayer.

Electronic structure implementations specifically designed for low-dimensional calculations exist in the literature. However, the method and implementation used in this thesis needs to be consistent, in order for the results to be comparable. In order to model a monolayer in three-dimensional supercell codes such as CASTEP and ELK a vacuum region is used. Usually included in the z Cartesian for computational efficiency, the unit cell is made up of the intended atoms, and then a vacuum region that needs to be large enough so that the atoms do not interact with their repeated selves in the z-direction. Care must be taken to ensure this

criterion is met, otherwise it is not a true simulation of a low-dimensional system. Although more plane waves will be required to model the much larger unit cell, small-mercy that only one k-point in the z-direction is required. The effect of the vacuum layer is shown in figure 4-15. Note that the simplistic exchange correlation functions currently implemented in many flavours of density functional theory do not include dipole-dipole interactions and therefore van der Waal's forces. With this knowledge, it is expected that the interaction distance in a DFT model would less than the realistic value, and so the convergence distance required to eliminate self-interaction between surfaces would be smaller than what might be expected. For completeness, a formalisations and implementations of longer range interactions in to density functional thoery covered in the following and numerous other articles [177, 178, 179].

### Co Bilayer

Two layers of cobalt is more applicable to the multilayer systems: the average thickness of cobalt will generally be about  0.3 nm and  0.5 nm in the systems. This is equivalent to an average number of cobalt atoms in the sandwiched layers of between 1.7 and 2.8 atoms, assuming the bulk cobalt interlayer spacing is a valid approximation. The bilayer system of (0001) HCP and (111) FCC cobalt

### Low-Dimensional Cobalt Summary

The anisotropy of cobalt thin films is found to be in the plane of the films. With similar results found for the monolayer and the bilayer. This is in good accordance with experiment and predating simulations [180]. This confirms that the perpendicular magnetic anisotropy in cobalt platinum multilayers must be interfacial. If thin

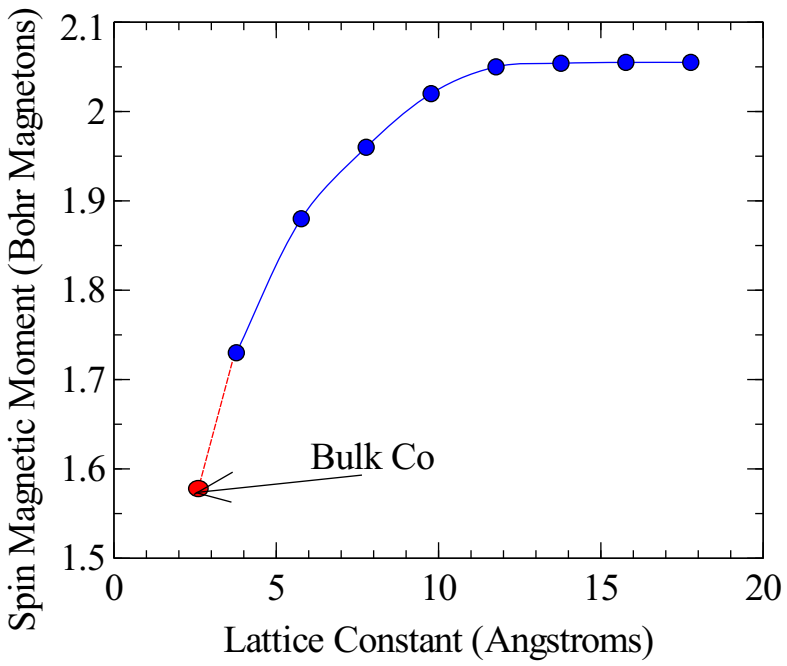


Figure 4-15: Convergence of the spin magnetic moment with the vacuum buffer layer seperating cobalt monolayers from supercell images. The 'lattice constant' is the distance between a monolayer atom and its nearest out-of-plane neighbour. Note that simulations could not be performed for the bulk lattice spacing, as the position of the monolayer would be directly above the underlying atom, 'AA' stacking. The out-of-plane lattice vectors could be changed to ensure 'AB' stacking, but is currently parallel to $z$ due to computational efficiencies and accuracies. The figure is based on ELK calculations performed using the LDA approximation with a 16x16x1 Monkhorst pack.

films of cobalt are in-plane anisotropic, HCP cobalt's preferred axis is the stacking axis (0001), and FCC cobalt is (100). However, these energies are very small differences on a condensed matter scale: 57 $\mu$ eV and 1.8 $\mu$ eV.

Table 4.5 shows a summary of the results for investigations in to cobalt monolayers and cobalt bilayers. Only systems demonstrating the hexagonal stacking basal plane were examined.

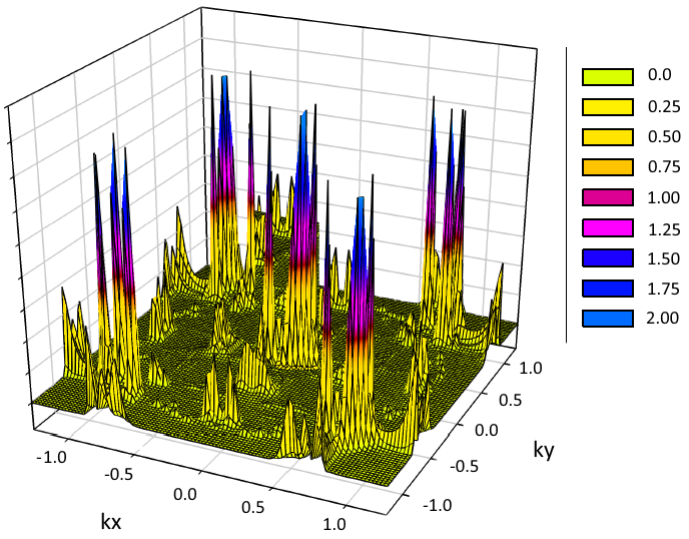


Figure 4-16: Colour and contour map showing the k-points for what contributions to the damping parameter are calculated. The measured system is a (111) cobalt bilayer, approximately the thickness of the cobalt sandwiched in a cobalt platinum multilayer. $a_{2d}$ represents the in-plane lattice constant. The modelling of this system and the equation used in parameterising the figure are shown in 4.23. The contributions have been measured for a scattering rate of $\tau^{-1} = 0.01/\hbar$.

Table 4.5: This table contains a compendium of predicted parameters for isolated cobalt momolayers and bilayers.

| Low-Dimensional Cobalt | $a_0$ | $d_z$ | $\mu_s^{Co}$ | $P$ | $K$ | $\alpha$ |
|---|---|---|---|---|---|---|
| cobalt monolayer | 2.47 | - | 2.05 | - | - | 0.007 (1.s.f.) |
| cobalt bilayer | 2.48 | 1.75 | 1.95 | - | - | 0.006 (1.s.f) |

### 4.3.5 Cobalt Platinum Multilayer Systems

The structure of (111) cobalt platinum multilayers was investigated using CASTEP and ELK. CASTEP was used to make an initial estimate of the interatomic spacings in the multilayer. Then ELK was implemented to relax and converge the calculations. The unit cells used in generating the bulk multilayers can be seen in figure 4-18. A comparison between the density of states in the multilayer systems can be seen in figure 4-19. In this plot a the density of states appears to be reasonably different between the 7-2 and 8-1 multilayers. However, because of the shape of the majority and minority curves, similar values (0.76 versus 0.73) are obtained for the

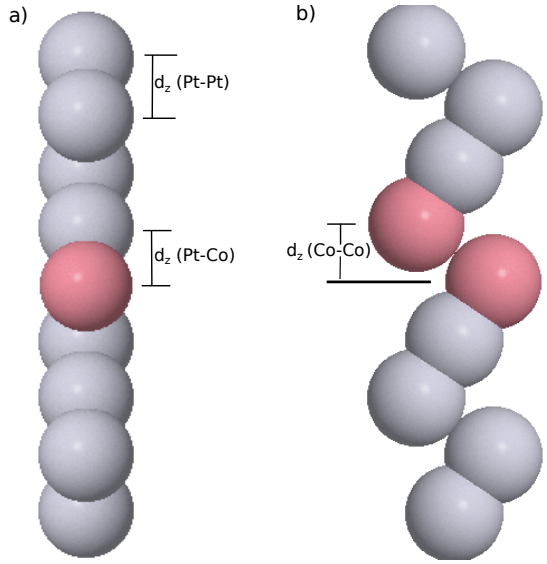


Figure 4-17: Structure and until cell of (111) cobalt platinum multilayers.

polarisation.

The magnetic moments of the cobalt atoms and induced moments on the platinum atoms can be seen in figure 4-20. The moments are all of a similar magnitude to those obtained in the disordered and ordered cobalt alloys. It can be seen that a 7 platinum atom buffer is just enough for the induced moment to decay to almost zero.

A comparatively large anisotropy can be seen for the multilayers. This is orders of magnitude larger than any of the bulk crystals or low-dimensional systems previously simulated in this chapter. A qualitative discussion as to possible reasons for the difference in presented in the summary.

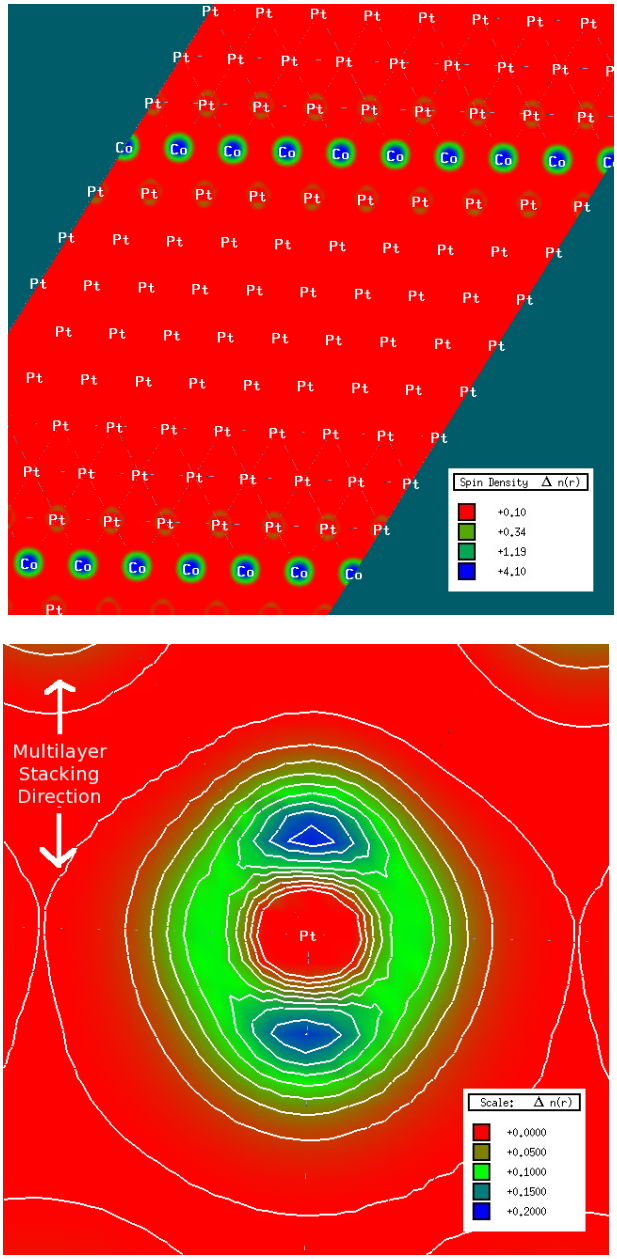


Figure 4-18: Colour map showing the spin density distribution in $Pt_8Co_1$ (111) stacked multilayers. The second plot shows a map of the induced spin density on the platinum atom adjacent to the cobalt surface.

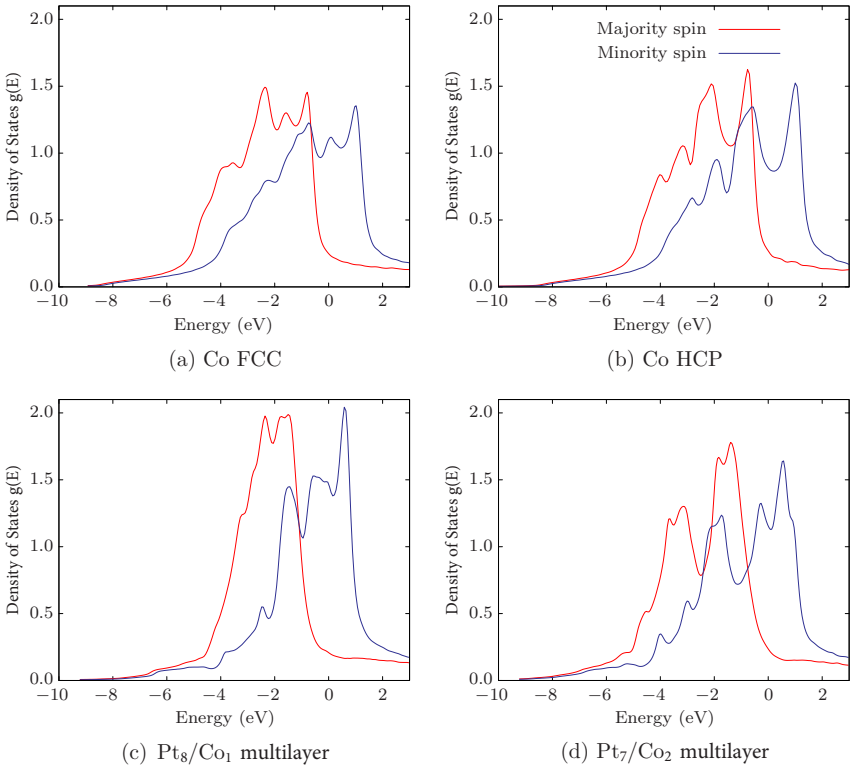


(a) Co FCC (b) Co HCP

(c) $Pt_8/Co_1$ multilayer (d) $Pt_7/Co_2$ multilayer

Figure 4-19: Comparison diagram for the spin-resolved density of states of the two bulk phases of cobalt and the $Co_1Pt_8$ and $Co_2Pt_7$ multilayers studied. A pronounced difference between the single and double cobalt layers is seen.

## 4.4 Summary and Discussion

Table 4.6 summarises the results from this chapter. Values for the lattice constant, magnetic moment, saturation magnetisation, polarisation, and (where calculable) the magnetocrystalline anisotropy and breathing and bubbling Fermi surface contributions to the Gilbert damping parameter.

Anisotropy values were seen in multilayer systems two orders of magnitude greater than the bulk and isolated thin film values. This is good evidence that the anisotropy in cobalt platinum multilayers can be apportioned to the cobalt platinum interface. In order to understand this effect consider a d electron in a free atom, and in atom in a planar geometry. The planar atom is neighboured by four atoms which can be

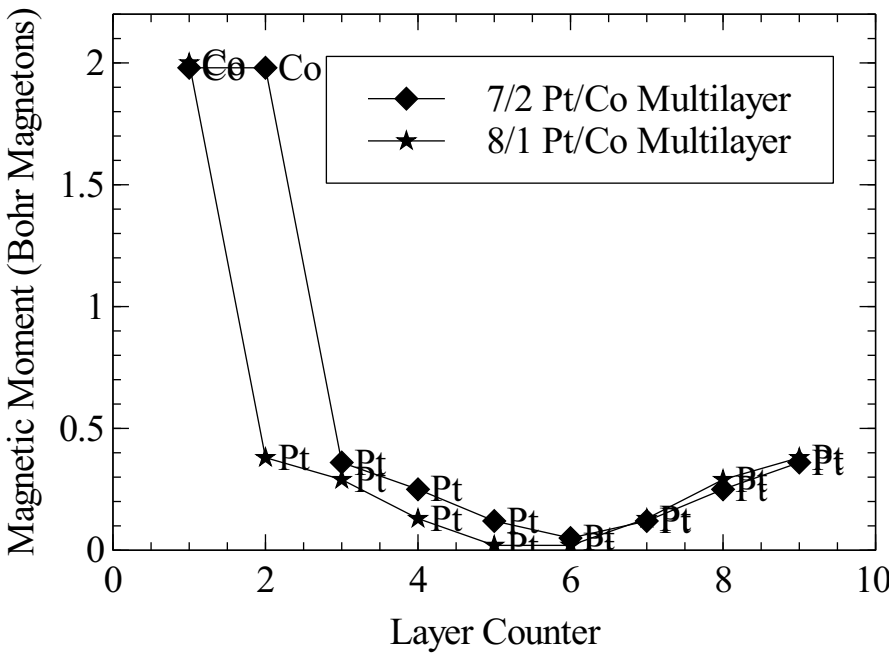


Figure 4-20: The magnetic moment's dependence on the stacking layer in (111) stacked $Pt_7Co_2$ and $Pt_8Co_1$ multilayers.

positively, or negatively charged. In the plane the electron will suffer Coulomb effects from the neighbouring atoms, altering its orbitals compared to the free atom. This is in essence the effect of the crystal field on the orbitals. Due to the loss of neighbours supplemented by a change in bonding at the surface, the orbital momenta are no longer entirely quenched.

This leads to the the anisotropic orbital moment and the interfacial anisotropy. In summary, the exchange interaction is responsible for the creation of the spin moment, and the crystal field induces anisotropic orbitals. The spin-orbit coupling links the spin and orbital moments, and the crystal field has a fixed direction. The combination of these factors yields the anisotropy. This simple qualitative argument does well to explain the differences in anisotropy found for bulk cobalt, low-dimensional cobalt, and cobalt platinum multilayers.

The values for polarisation were obtained by summing the spin-resolved density of states about the Fermi energy. Little work appears to have been conducted on

Table 4.6: This table comprises the multitude of results in this chapter in to one coherent table, for ease of dissemination. Gilbert damping parameters are given to one significant figure, saturation magnetisations are given to two, polarisations two, and anisotropies two significant figures respectively.

| System | $M_s$ (A m$^{-1}$) | $P$ | $K$ (J m$^{-3}$) | $\alpha$ |
|---|---|---|---|---|
| FCC-Co | 1.4 $\times 10^6$ | 0.67 | (001) 4.5 $\times 10^3$ | 0.001 |
| $Co_3Pt$ | 1.0 $\times 10^6$ | 0.74 | (111) 1.2 $\times 10^3$ | 0.001 |
| CoPt | 7.7 $\times 10^5$ | 0.75 | (111) 32 $\times 10^3$ | 0.001 |
| $CoPt_3$ | 4.2 $\times 10^5$ | | (111) 1.3 $\times 10^3$ | 0.001 |
| $Co_{0.125}Pt_{0.875}$ | 1.8 $\times 10^5$ | 0.69 | (111) 7.9 $\times 10^3$ | - |
| $Co_{0.25}Pt_{0.75}$ | 3.5 $\times 10^5$ | 0.70 | (111) 7.7 $\times 10^3$ | - |
| $Co_{0.375}Pt_{0.625}$ | 5.2 $\times 10^5$ | 0.72 | (111) 7.5 $\times 10^3$ | - |
| $Co_{0.5}Pt_{0.5}$ | 6.9 $\times 10^5$ | 0.73 | (111) 3.8 $\times 10^4$ | - |
| $Co_{0.625}Pt_{0.375}$ | 8.6 $\times 10^5$ | 0.72 | (111) 7.4 $\times 10^3$ | - |
| $Co_{0.75}Pt_{0.25}$ | 1.0 $\times 10^6$ | 0.72 | (111) 7.2 $\times 10^3$ | - |
| $Co_{0.825}Pt_{0.125}$ | 1.1 $\times 10^6$ | 0.73 | (111) 6.9 $\times 10^3$ | - |
| Co Monolayer | 1.8 $\times 10^6$ | - | (100) 1.4 $\times 10^4$ | 0.008 |
| Co Bilayer | 1.7 $\times 10^6$ | - | (100) 1.3 $\times 10^4$ | 0.007 |
| (111) $Pt_8Co_1$ | 1.8 $\times 10^6$ (Co layer) | 0.68 | (111) 1.8 $\times 10^6$ | - |
| (111) $Pt_7Co_2$ | 1.7 $\times 10^6$ (Co layer) | 0.69 | (111) 1.6 $\times 10^6$ | - |

determining the polarisation of a material for micromagnetic purposes. This means that it is difficult to draw specific quantitative comparisons for the polarisation parameter. However, as the polarisation is usually characterised by the density of states difference at the Fermi energy prior published work can be compared. Using the ELK implementation of DFT the author was able to rerun the results produced by Razee *et. al.*[36]. Results that appear to be within 5% were found, but as the smearing parameter could effect the exact figure used for the polarisation little certainty can be held for the quantitative comparison.

The precision required to model the Gilbert damping parameter using self-consistent density functional theory calculations is not ideal. Band eigenvalues of have to be converged to hundredths of electron volts for the parameter to approach a steady. Calculations using the force theorem are possible, but as the shape of bands changes so much with the change of magnetisation direction (on such a small scale, nonetheless), the results can fluctuate vastly between simulations of similar systems. The KKR methods described are possibly more useful for these investigations as they are

not attempting to model the eigenvalues to such high precision. The author would like to note the following references for work being performed in to the Gilbert damping parameter in the KKR regime [181, 182, 183]. However, at the time of writer the author remained unaware of particular self-consistent schemes not relying on perturbative effects.

The damping factors found in the cobalt monolayers and bilayers are extremely interesting. They are almost an order of magnitude (0.008 versus 0.001) larger than the bulk and alloy systems. Unfortunately due to the convergence criteria discussed above, fully representative calculations for the multilayer systems could not be recorded. The plot in figure 4-16 attempts to show the contributions to the Gilbert damping parameter from specific points in K-space. It is not clear whether or not the Gilbert damping parameter would also be increased in the monolayer when sandwiched inside cobalt, but as the damping parameter utilised the band energies like the magnetocrystalline anisotropy calculations it is likely that it will change. The magnetic moments in isolated and sandwiched monolayers, however, are similar. This, however, is due to the forced lattice constant change that the sandwiched layers would have, if it were not for this, then it is anticipated that the magnetic moments in the multilayers would be significantly lower. Remember that the lattice constant expansion causes the bands to flatten, leading to a more densely packed density of states. This in turn yields a higher magnetic moment, due to the increased exchange splitting.

The calculations presented in this chapter are not fully representative of experimental systems. In an experimental system there would typically be crystalline disorder and defects. In addition to this, many of the samples used in experimental studies are created by DC magnetron sputtering. This technique would generally create polycrystalline materials. These materials are difficult to model using electronic structure calculations in the augmented plane wave we have been working in. Large unit cells with dozens if not hundreds of atoms would be required to sufficiently model the system with grain boundaries and defects. Further work could use the aforementioned methods on larger scales with high performance computers. It is more likely that as the functional modelling and DFT implementations improve,

more and more systematic errors will be removed. Otherwise, the entirely different style of approach such as the KKR method implementing cutting-edge developments in the Torque Correlation Model would be the author's avenue of choice.

# Chapter 5

# Domain Wall Motion and Applications

## 5.1 Introduction

Chapter 2 highlighted the use of parameters in micromagnetic theory to yield equations of motion for domain walls in nanowires that are solvable. Chapter 4 attempted to investigate the underlying physical nature of these parameters, and how using computational methods and analysing experimental data can lead to estimates of these values. This chapter will use the results of the previous chapters to parametrise and analyse the current-induced motion of domain walls in real-world, if not idealised, materials.

## 5.2 Modelling Domain Walls with OOMMF

Chapter 2 introduces approximate modelling of magnetic domains in micromagnetic theory. In this section it will be elucidated as to how these structures can be modelled in non-ideal/perfect environments, such as experimentally patterned areas and including the effects of surface roughness. Typically the derived micromagnetic equations of motion are analysed using one of two models, finite difference methods, or finite element methods. This thesis uses the OOMMF (object-oriented micromagnetic framework) implementation, which implements the finite difference method, of which further details are in the following subsection. Capable finite element method solvers are also available in the field, such as magpar [184] and nmag [185]. The finite element meshing could more accurately measure some of the experimental features covered in the chapter. However, the extremely large surface areas of thin films are not well adapted to meshing, as the RAM usage is much larger.

### 5.2.1 Implementation

OOMMF is an open-source software package that implements the Landau-Lifshitz-Gilbert (LLG) equation. It generates spatial and temporal numerical solutions using the finite difference method. A schematic of how OOMMF discretises the micromagnetic body as a mesh is shown in figure 5-1. The continuous micromagnetic model is applied to a rectangular discrete mesh. The spatial derivatives are approximated efficiently and accurately using the 4th order Runge-Kutta algorithm to provide O(4) accuracy [186]. OOMMF will first compute all of the spatial derivatives in the system and then make an estimate as to what configuration would be energetically favourable in the next timestep within the constraints of the LLG equation. The computationally expensive part of the calculation involves the deduction of the point-wise demagnetising field. As this is the non-local term that contributes to the effective field and thus directly affects the magnetisation. Work

by Aharoni [71] is included in OOMMF with reference in order to make this calculation as straightforward as possible, but as the system size increases this component increases substantially with the number cells.

If the ground state position of a domain wall within an non-trivial geometry is required then OOMMF can implement an Euler based algorithm in order to find a local minimum for the magnetisation configuration. This is can be regarded as the computational physicists equivalent to creating known input conditions to running an experiment. As it can occur in experimental systems, and those electronic structure calculations in the previous chapter, care should be taken to ensure that the local minimum is suitable, and if possible a range of local minima should be chosen to mitigate the issue of not beginning in the global minimum.

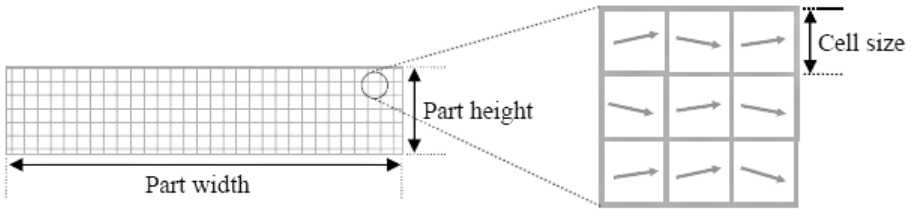


Figure 5-1: Schematic of OOMMF's operation on a micromagnetic body. After [187].

### 5.2.2 Convergence

The cancellation of errors and the mitigation of systematic errors is crucial to any computational investigation. In a system containing a FDM the cellsize needs to be small enough to capture all physics, but large enough to allow children to go to school.

The mesh size in a micromagnetic computation is dependent on the physics that need to be captured, and the parameters used in the simulation. Termed the 'exchange length', the mesh size required to accurately model the energies of domain

walls in micromagnetics. The cellsize has to be small enough to represent the magentisation as a continuous and slowly varying vector, as this is one of the key tenets of micromagnetics [188]. The exchange length is defined as (for a magnetically hard material)

$$\kappa = \sqrt{(\frac{A}{K})}\,, \tag{5.1}$$

where $K$ and $A$ are the micromagnetic parameters discussed in chapter 2 sections 2.3.1 and 2.3.2, the anisotropy energy density and the exchange length. Referring to these sections and the previous chapter calculations we should note that these terms dictate the size and shape of the domains almost exactly for simplistic nanowire systems with uniaxial anisotropy. For a magnetically soft material the axial anisotropy is replaced by the effective shape anisotropy caused by the demagnetising field:

$$\kappa = \sqrt{(\frac{2A}{\mu_0 M_s^2})} \tag{5.2}$$

For materials such as cobalt platinum multilayers and trilayers with thin cobalt layers with very large perpendicular magnetic anisotropy, (PMA) the exchange length becomes small, down to two nanometres. However, experimental samples rarely have linear dimensions less than a micron. A 50 micron wire that is 1 micron wide would therefore require 625 million cells. If a third dimension was incorporated in to the problem, as was an idea for refined racetrack memory, then the amount of information starts to become quite large. In the aforementioned case. A basic 3D implementation might only have 20 cells to roughly model a linear change in a parameter within the z-direction. With this information the number of cells in the toy model has expanded to 13 billion cells. Now the equation has to be solved for every cell in an iterative manner. Just storing the 13 billion three-vectors required to store the problem in memory at double precision (8 byte / 64 bit) equates at roughly 2.5 trillion bits or 0.3 terabytes. 300 GB of RAM is a lot of information to hold in memory, and thus without the system approximations that are made in this chapter many of the problems in question would be numerically intractble. Systems of this size that require solving without further system simplification are managed by changing the model implementation: providing a generally less accurate

implementation of the calculation of the demagnetising field.

Niceties of computational efficiency can be included, such as fixing spins in the region you are not interested in the dynamics, but the non-local demagnetising field still updates its system-wide values with the contributions from all of the points in the simulation. One method that can remove this bit of obscurity is to identify the region of the sample you are interested in measuring. A single iteration of the solver could then be used to generate a demagnetising field for the device. This is performed by removing the central interesting section, to ensure that no dynamics or magnetisation changes add to the local magnetic field. The measured field at where the central section used to be is the effective demagnetising field from the edge regions. The simulation can then be inverted, i.e. only simulate the central region.

The saved demagnetising field from the large system can then be added as an external perturbative field. Within the OOMMF framework,these is an option to perturb a simulation using a scalar or vector field obtained from a file. The demagnetising field can be output to a file from the results of the convergence runs, and then loaded back in to the simulation once suitably modified for the following simulations without the extra experimental regions that just perturb the local system by affecting the global demagnetising field calculation. Convergence of this field is shown in figure 5-2. From this graph it can be seen that, either: (a) 3 microns of extra nanowire either side of the central region is included in the simulation, or (b) a nanowire of 6 + 'X' microns is used to generate a demagnetising field that is then included in any future calculations that require it.

When attempting to model experimental length scale systems in micromagnetics we can use initiative, experience, and convergence calculations to ensure only the regions that need to be simulated are included in the final computational models. The above description of removing the need to simulate the entire nanowire by simply simulating the nanowire without the region of interest is a good example of this. Another popular technique is to run the model to determine the preferred domain structure prior to any current calculations. Further efficiencies implemented are the

reduction in the problems in to different phenotypes. The domain moving along a nanowire, and the domain moving through a hall cross are quite different problems exhibiting unique phenomena. In this thesis the steady state of propagation (subject to Walker Breakdown [75]) is quite predictable and well-modelled, whereas the transition in to the cross region is studied in this chapter. The methods of experimentally measuring the transit of the domain wall using the extraordinary Hall effect efficacy will be much better understood if the bar transit is made less opaque.

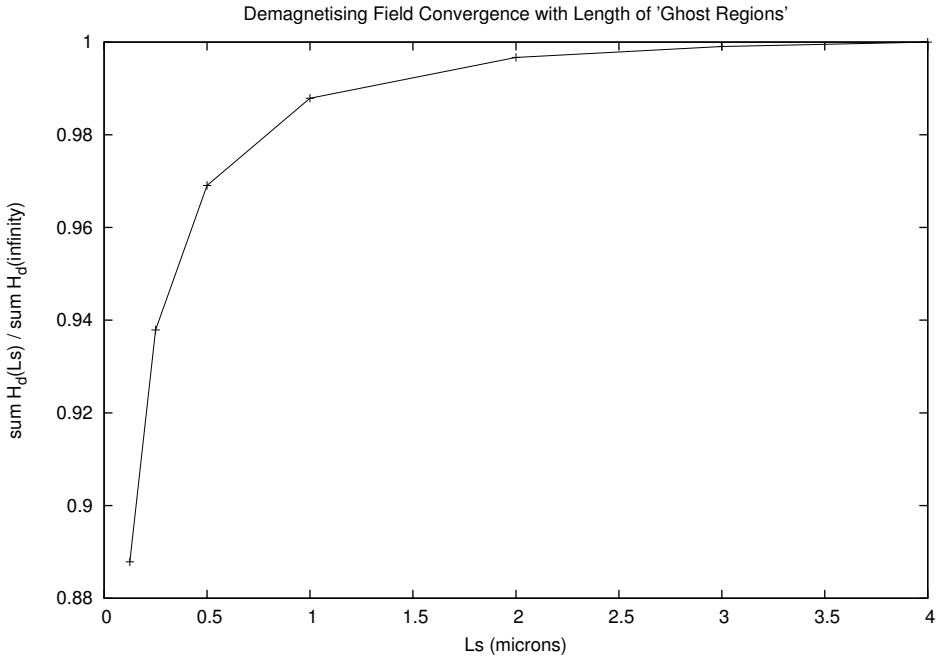


Figure 5-2: Convergence of demagnetising field of a central cut-out section of a nanowire with respect to the length of the nanowire adjacent to it.

### 5.2.3 Field-Driven Motion

Due to the Zeeman interaction an external magnetic field can be used to induce domain wall motion. This motion, however, does not genearally retain the size of the domains involved. The direction by which the domain wall travel would be entirely dependent on the polarities of the applied field and the internal polarity of

the domain wall. The regions with polarity similar to the field would get larger, and the opposite would get smaller.

The analytical and numerical solution of this problem was first undertaken by Walker and Schryer [75]. Field driven motion is much simpler to model, but is of little use in memory applications. This is because quite large fields of roughly a tesla are required to move the domains in hard and pinned materials. On a nanoscale with other components nearby it is easier to provide a large electronic current for motion that a particularly large magnetic field. Typically large currents are used to generate sizeable electromagnetic solenoids, thus making this technology of little use for direct motion on the nanoscale. If the idea were to globally transfer the polarity of the domains then this would be useful, much like an urgent format feature for sensitive data.

## 5.3 Applied Micromagnetics in Nanowires

Non-ideal geometries, variations in parameters, and the problematic non-local demagentising field usually make the LLG equation unsolvable analytically. However, if assumptions similar to section 2.4 are made, then the LLG equation can be solved in the dynamical regime analytically.

### 5.3.1 Field Driven Motion

#### 1D Dynamical Solution

Although previously stated that system is not particularly useful for the difficulties present in using translatable magnetic domains in memory, the theory and existence

of an indicative analytical solution make a short study attractive for understanding the basic phenomena that are present in the more complicated current driven domain wall motion.

Under an applied magnetic field the energy in the sample will be changed, and if applied suitably the domain wall can be translated. An analysis of this motion was first performed by Walker & Schryer in 1974 [75] in a 1D model. Firstly, two equations for the motion of the domain wall were formulated from the LLG equation, utilising the definition of the effective field and transforming in to 1D coordinates:

$$\frac{\partial\theta}{\partial t} + \alpha \sin\theta \frac{\partial\phi}{\partial t} = \frac{-\gamma}{\mu_0 M_s \sin\theta} \frac{\delta E}{\delta\phi} \tag{5.3}$$

$$\sin\theta \frac{\partial\phi}{\partial t} - \alpha \frac{\partial\theta}{\partial t} = \frac{\gamma}{\mu_0 M_s} \frac{\delta E}{\delta\theta}\,. \tag{5.4}$$

Substituting in the energy terms in the functional derivative, using the trial solution found for the static case, leads to the following solution for the domain wall profile

$$\ln\left(\tan\frac{\theta}{2}\right) = (x - vt)\sqrt{\frac{K}{A} + \frac{K_D}{A}\cos^2\phi_0}\,, \tag{5.5}$$

where $v$ and $H_c = \alpha M_s/2$ are the velocity of the domain wall, and the critical field respectively. $K_D = \frac{1}{2}\mu_0 M_s^2$ is a parameter quantifying the demagnetising field. The velocity is given by

$$v = \frac{\gamma H_{app}}{\alpha}\left(\frac{K}{A} + \frac{K_D}{A}\cos^2\phi_0\right)^{-\frac{1}{2}}\,, \tag{5.6}$$

with the following constraint on $\phi$

$$\sin 2\phi_0 = \frac{2H_{app}}{\alpha M_s} = \frac{H_{app}}{H_c}\,. \tag{5.7}$$

The model can be extended to allow the in-plane angle $\phi$ is allowed to vary with

time. Regarding the previous equations gives

$$H_{app} < H_c \quad : \quad \phi(t) = \arctan\left(\frac{H_c}{H_{app}} - \sqrt{\left(\frac{H_c^2}{H_{app}^2} - 1\right)} \coth \frac{\gamma\sqrt{H_c^2 - H_0^2}}{1+\alpha^2} t\right)$$
$$H_{app} > H_c \quad : \quad \phi(t) = \arctan\left(\frac{H_c}{H_{app}} - \sqrt{\left(1 - \frac{H_c^2}{H_{app}^2}\right)} \cot \frac{\gamma\sqrt{H_0^2 - H_c^2}}{1+\alpha^2} t\right) \quad (5.8)$$

for a wall that started in the Bloch wall state.

From this equation we can see that the out of plane magnetisation can be rotated by the applied field. This effect is of a constant rotation at fields less than the critical field. Furthermore, the critical field is a field at which above this any motion of the domain wall cannot be described linearly. The magnetisation cannot cant at sufficient speed in order to equate the motion and twisting of the domain wall - a transition into a region called Walker breakdown [75]. Therefore, for the motion of a domain wall to be stable, the applied fields must be below the critical field. An understanding of the effect of a static applied field and the reporting of Walker breakdown for certain applied field criteria allows us to investigate the current-driven case with more known information.

### 5.3.2 Magnetisation Reversal In Multilayer Systems

An application of field-driven motion that has formed the cornerstone of magnetic experiments are magnetisation loops. A micromagnetic framework implementation such as OOMMF can be used to investigate and confirm standard experimental techniques in magnetism, performing hysteresis measurements and recording magnetisation loops. The value at which the switching of the magnetisation starts to occur, the coercitivity, can be used under certain conditions to measure the anisotropy of a sample. A range of magnetisation loops of cobalt platinum trilayers for thicknesses of cobalt in a cobalt platinum trilayer is shown in figure 5-3. As

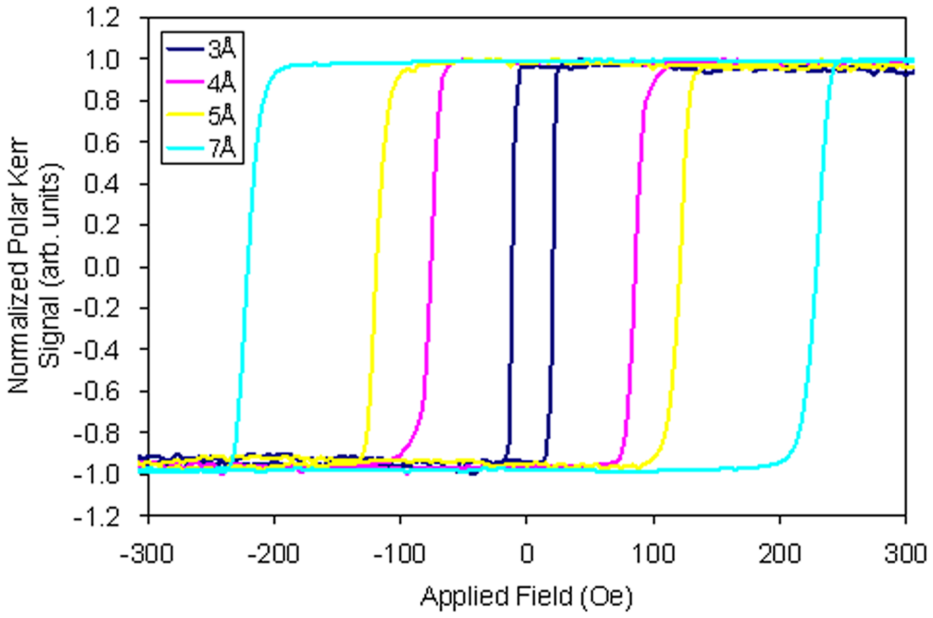


Figure 5-3: MOKE results from an experiment showing the change in the magnetic anisotropy and hence coercitivity with the thickness of the cobalt layer. Experiment performed by Ming-Che Wu while at the University of Bath, and is unpublished.

we have discussed in the previous chapter it is the alloying of the cobalt and platinum surfaces which cause perpendicular magnetic anisotropy (PMA) in the system. However, bulk cobalt will have in-plane anisotropy. Therefore, if the conditions of the individual samples were of similar quality and state, then the change in coercitivity will hint at the change in anisotropy/easy axis of the trilayer as the thickness changes.

OOMMF can be used model magnetisation loops, but careful preparation must first be made. If the switching mechanism is via domain wall motion, then the domain wall has to be 'born' somewhere. If a sample is fully magnetised in a specific direction, then there will not be any magnetic domains with the opposite polarity. For a simulation method like OOMMF this poses problems. The domain walls would have to be formed on the edges of a sample, as OOMMF has no mechanism for a new magnetic domain to spontaneously appear. Contrastingly, real systems could possibly have small but finite magnetic defects or regions with different material properties within it. These regions could be small enough so that the experiment

need not know they exist, merely that they do exist and act as domain/domain wall nucleation sites.

The high anisotropy in these systems poses computational problems. The reason a domain wall would nucleate at an edge in an OOMMF simulation, is that this is the place the exchange energy will be the weakest. Certainly there will be contributions from magnetostatic energy, but all that needs to occur is for the symmetry to break, and then configuration changes might occur. To quantify the energy required to overcome the anisotropy we just need to input the parameters in to our micromagnetic energy densities defined in chapter 2. The Zeeman interaction must overcome the exchange and anisotropy holding the magnetisation along the easy axis. That is, the following equation must be satisfied:

$$-\mu_0 \mathbf{M}.\mathbf{H} \approx K + A(\nabla m_z)\,. \tag{5.9}$$

Inputting typical material parameters of $K = 1.6 \times 10^5, A = 3 \times 10^{-11}$ taken from [4] and are indicative parameters for a highly uniaxial material used in OOMMF simulations for cobalt systems, with $m_z = cos\theta$ yields

$$H \approx 8 \times 10^4 \mathrm{A/m} \approx 1000 \text{ Oe}\,. \tag{5.10}$$

The aforementioned materials are different to those estimated in the previous chapter, from table 4.6 we can see that the generic value for $K$ is an order of magnitude less than the value obtained ( $K = 1.7 \times 10^6 Jm^{-3}$). The discrepancy will be discussed forthwith. Comparing the calculated figure of 1000 Oe to the switching field for the 3 nm thick cobalt layer in figure 5-3, this is approximately two orders of magnitude higher. Therefore, special methods need to be used to correctly model the switching [88, 189, 86].

The number of nucleation sites in the sample poses the question, what density do we require to accurately model the magnetisation loop? This is difficult in practice, as the physical experiment will undoubtedly be conducted with different parameters to any computational experiment. A simple but effective method for

treating this problem would be to increase the number of nucleation sites until the switching fields match. The computation would still need to know the magnitude of the anisotropy to converge to its final solution. When the switching does finally happen, the magentisation reversal happens in one magnetic field increment. This is because the switching field was so high that when symmetry finally was broken, the equilibrium low-energy state is the opposite polarity device.

Another trick used in OOMMF computations to better examine magnetisation loops is including a *free layer*. The numerical simulation is only performed for the region of interest, but extra regions which do not contribute to the measure magnetisation can be included. The magnetisation of extra regions can be pinned in specific or random orientations, greatly reducing the large energy cost of creating a new domain wall of the edge of a device. Specifically, the magnetisation cannot change for the pinned regions. They might be put in place to mimic a region that is harder and thus more opposed to switching. Otherwise, the demagnetising and exchange term (if any - only would there be any near a boundary) are counted from the fixed regions, with no rotation of the fixed regions. These fixed regions can be a source of domain wall nucleation in the free layers, acting as some sort of spin bath.

Each arm of the magnetisation loop is conducted separately, as otherwise the magnetic field to switch the magnetisation could also switch the nucleation site, making them unusable for the next arm. One method that can be used to achieve operation of a full magentisation sweep would be to fix the spins in the nucleation sites. The switching field of approximately 15 Oe is not reproducable using the current parameter set. The method of fixing a layer for domain walls to nucleate is generally used in the literature [88].

## 5.4 Domain Wall Pinning

### 5.4.1 Introduction

The pinning of a domain wall on impurities is not always a desired effect. Enhanced pinning and unfavourable pinning caused by system impurities and system properties in an uncontrollable manner would be best avoided. The excess energy and torque required to move a domain wall away from a pinning site could be one reason for the higher current densities that are generally observed in experiments than what emanate from heavily parametrised computer simulations [190, 191].

For the application of racetrack memory pinning sites can be used favourably. That is, a pinning effect can be used to ensure that domain wall do not meander about the nanowire under a small applied residual magnetic field or current. The types of pinning that have been investigated are caused by: (a) structural patterning of the nanowire, (b) sharp changes in anisotropy caused by material deformation or ion bombardment. Case (a) can be directly modelled in OOMMF by comparing the simulation of a system with and without the cross geometry and comparing the wall deformation.

### 5.4.2 OOMMF Hall Cross Implementation

Under the original OOMMF model spin transfer torque implementation the 2D geometry had a substantive effect on the transition of the domain wall. Figure (5-4) shows how the 1D applied current can initially be pinned to the corners of the nanowire. The domain wall does not spread in to the upper or lower nanowire regions, but eventually 'pops' away from the pinning sites. The elongated size of

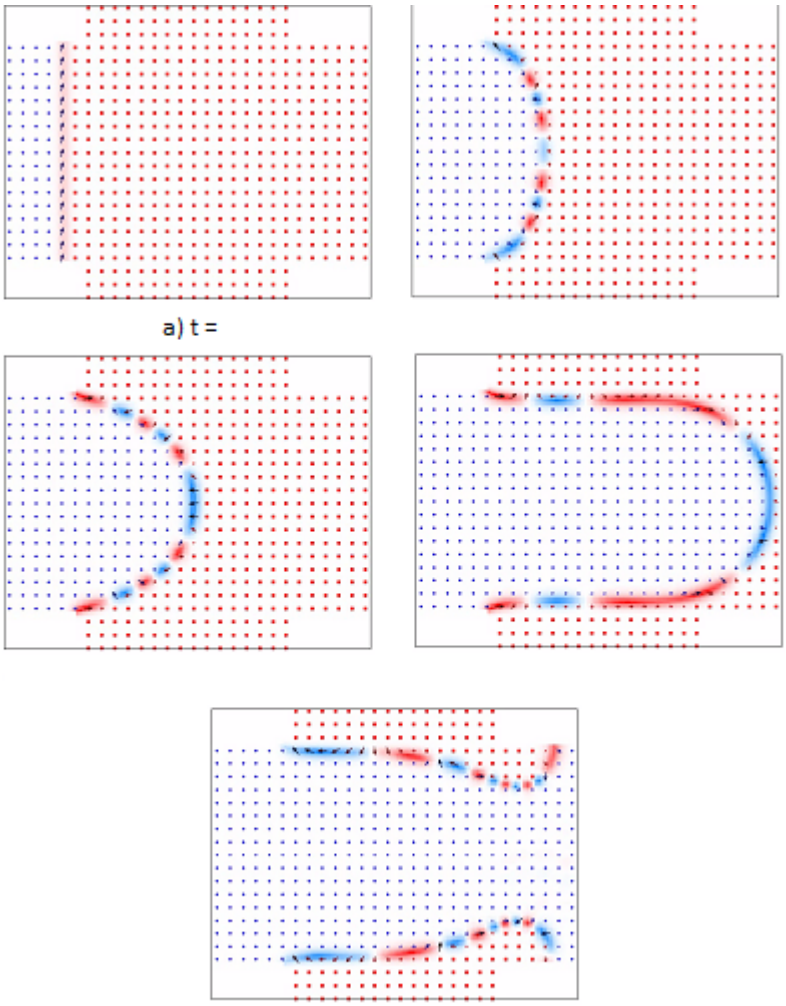


Figure 5-4: The domain wall profile and evolution of magnetic domains within a hall bar of central geometry 500 nm × 500 nm with typical material parameters for cobalt platinum multilayers. This simulation only has electron flow from left to right (1D current flow).

the domain wall prior to the pinning collapse suggests that there may be a formal relationship between the depinning current and the size of the domain wall.

It was estimated that the pinning is most likely exacerbated by the fact that (a) in figure (5-4) the spin torque can only occur in the central region, (b) there is no Oersted field attached to the spin current, and (c) the edges of nanowires where they

meet are abrupt, which was imagined to be converse to the experimental system. To this end, further investigations were then performed in order to estimate which cases are important, and if any are simulation artefacts caused by the model set-up not being fit for purpose.

### 5.4.3 OOMMF Extension to 2D Currents

In order to provide a qualitative insight in to the origin of the pinning in the hall cross the LLG implementation of STT was extended by myself to account for two-dimensional electron flow throughout the computation through the use of an electronic vector field. This is a grid specified prior to the commencement of the simulation to include all of the cells used in the simulation and a three vector for the normalised current density within that cell. This parametrisation was performed through the use of a standalone fortran code written to compute the current flow, along with the, somewhat sweeping, assumption that the domain wall's presence and motion does not affect the current distribution. Remember that the domain's effect on the electron is not typically studied in this thesis, however the author would like to cite Aziz [37, 4] and Hayashi [192] for significant contributions to the knowledge and effect of anisotropic magnetoresistance.

The code that was written to understand the steady state spin-polarised current within the Hall bar geometry was written in fortran and implemented the Gauss-Seidl relaxation method in order to estimate the current flow [186]. The equations iteratively solved in the current flow calculation were Maxwellian and classical:

$$\mathbf{E} = \sigma \mathbf{J} \quad , \nabla \times \mathbf{E} = 0 \quad , \text{and} \, \mathbf{E} = \nabla \phi \, . \tag{5.11}$$

That is, the electric field is the conductivity (tensor) times the current density, there are no time-varying magnetic fields so there is no rotational source of the electric field, and that as the electric field can be written as the gradient of the scalar potential $\phi$. Altogether the problem is the Laplace equation with hall bar

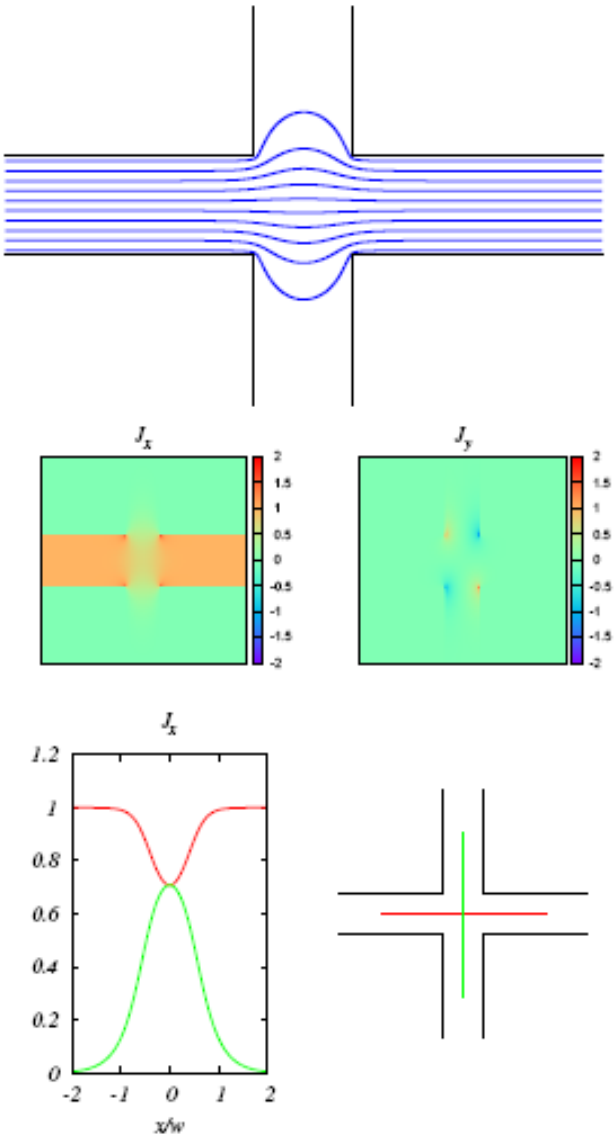


Figure 5-5: Top: Current density streamlines for straight Hall bar edge geometry and rounded edges. Middle: Current density values as ratios of the specified current density. Bottom: The x-component of the current density modelled across the center of the nanowire channel.

geometry boundary conditions dictated by the presence or lack of a spin-polarised current.

A Hall bar, or Hall cross, is an experimental design consisting of two perpendicular nanowires with voltage contacts to measure resistance between x and y directions.

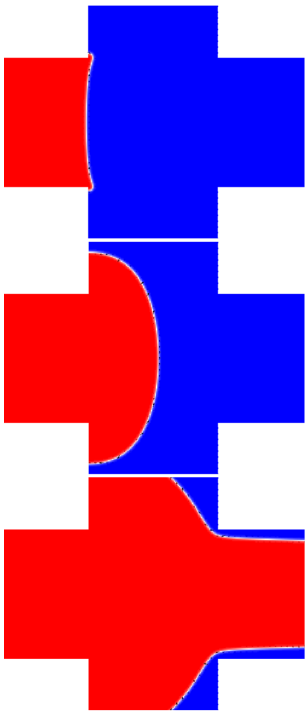

Figure 5-6: The domain wall profile and evolution of magnetic domains within a hall bar of central geometry 500 nm × 500 nm with typical material parameters for cobalt platinum multilayers. This simulation only has electron flow from left to right in the nanowire, but the current is allowed to spread as long as it recombines in the end nanowire section (2D current flow).

Simple simulations can be conducted for the traversal of a domain wall across a Hall bar and these are shown in figure 5-8 in the left hand column. When performing the simulations it was noted that the motion of the domain wall just looked unphysical, the wall was not deviating in to the other nanowire even though the parameters were identical.

Figure (5-5) shows the initial investigatory work performed by Dr. Simon Crampin of Bath University (*unpublished*). This streamlines show how the current would indeed bulge in to the top and bottom nanowire sections due to the Hall bar geometry. The middle diagram shows how the current density is significantly enhanced at the corners. The bottom diagram illustrates the drop in the current density at the centre of the nanowire due to the current spreading out. The latter two diagrams aid greatly in the estimations for how the domain wall pinning would be affected

by the Hall bar geometry. Due to the enhanced STT it would be expected that the domain wall would depin for much lower currents than would be exhibited in the 1D model previously discussed. The drop in current density for the central region suggests that the middle of the domain wall might not race ahead of the rest of wall as was previously thought in the 1D model. Figure (5-6) shows the divergence of the wall with the new 2D current density implemented.

To implement the new 2D current density in the OOMMF model the existing STT implementation had to be modified. The STT term in for the x-only direction is and can be easily modified to include y terms:

$$(\frac{d\mathbf{m}}{dt})^{STT} = \left[\alpha\gamma\mathbf{m}\times(\mathbf{m}\times\mathbf{H}) + \left(\frac{\beta-\alpha}{1+\alpha^2}\right)\mathbf{m}\times\frac{\partial\mathbf{m}}{\partial x} - \frac{1+\alpha\beta}{1+\alpha^2}\mathbf{m}\times\left(\mathbf{m}\times\frac{\partial\mathbf{m}}{\partial x}\right)\right] \tag{5.12}$$

where $\alpha$ is the micromagnetic damping parameter $\beta$ is the adiabaticity. The overall derivation stems from the Thiaville equation in chapter 2 equation 2.53. Typically $\mathbf{u}$ is approximated as only having an x-component, but it is trivial to include the y-component in the deduction of the LLG STT add-on. That is, replace

$$u = (u_x, 0, 0) \quad \text{with} \quad u = (u_x, u_y, 0)\,. \tag{5.13}$$

Preliminary results for this new 2D current functionality in OOMMF are shown in figure 5-6. It is easy to see an immediate penetration in to the top and bottom nanowire regions for the domain wall, as expected from the enhanced current density in the corners of the region. The unwanted effect of the new current distribution and simple OOMMF implementation is the final graph in figure 5-6. This diagram shows that the wall finds it difficult to repin on the other side of the Hall cross. The positive reason for depinning on the start of the channel is the negative addition stopping the wall from recombining with the opposite wall. This is due to the enhanced current density running parallel to the wall profile - only perpendicular contribution would enable the wall to repin effectively.

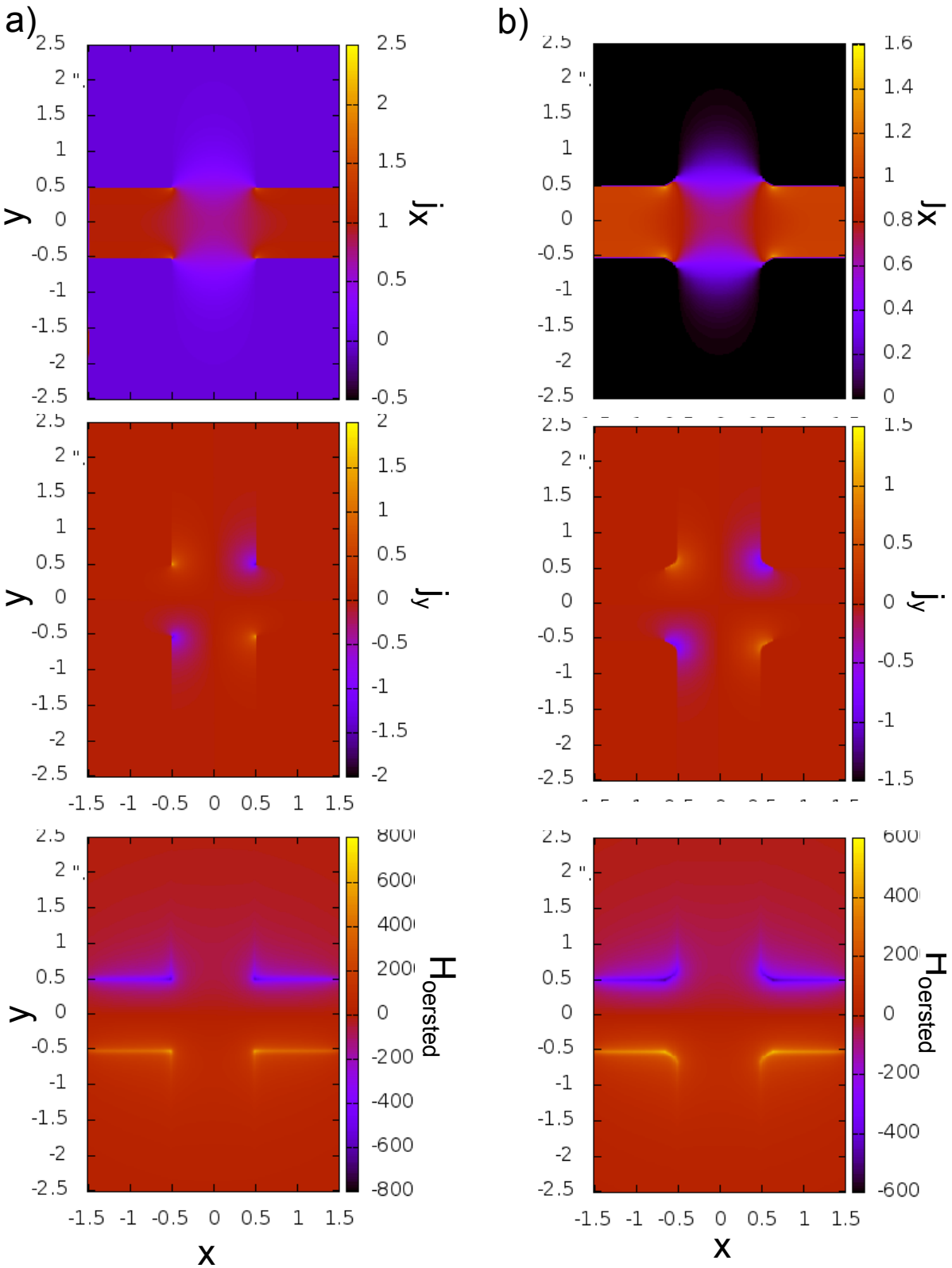


Figure 5-7: Current density and Oersted field for the cobalt layer. Case a) / b) is for straight / rounded edged Hall bars. The current density x-component and y-component are plotted separately demonstrating how the is spread more evenly in the rounded case. The Oersted field contributions localised to the surface of the system is shown in the bottom row.

### 5.4.4 Introducing Experimental Features

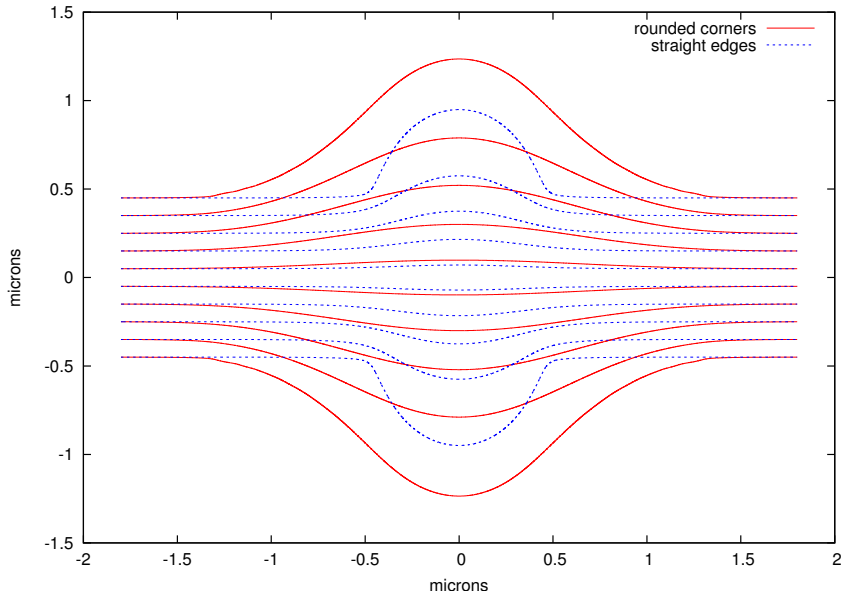


Figure 5-8: Current density streamlines for straight Hall bar edge geometry and rounded edges. The effect of the rounded edges can be seen on the streamlines. The currently is much more gently varying compared to the straight edge case.

The next issue noted was that the corners of the straight edge Hall cross demonstrated extremely high concentrations of current density. The current densities pushing the samples are already of the amount that could demagnetise the sample. It was decided that more accurate simulations could be performed (and more physical ones) if the edges were rounded. Experimentalists have confirmed that the edges would not be abrupt anyway. The rounding required the cellsize of OOMMF to be reduced further, as rectangular grids are not sufficient for modelling curves.

Further simulations performed are shown in figures 5-7 and 5-9. Streamlines of the current flow in a the Hall cross region are demonstrated in 5-8. These simulation also included the Oersted field. The Oersted field was directly calculable from the derived current density calculations. The contribution from this field is shown in figure 5-7 with, naturally, the only noticeable contributions being near the sample edges. Within the simulation parameters the system is broken up in to cells. The Oersted field within that cell would perform a clockwise magnetic field about the moving electrons. This field will always occur and have positive polarity one side of

the cell, and negative the other. This means that with the generally slowly varying current density the Oersted field will be mostly cancelled out by the neighbouring cell.

The effect of rounding the edges of the Hall cross are shown in figures 5-7, 5-8, and 5-9. We can see that the rounded edges alleviate some of the current build up at the corners of the Hall cross. The current does not penetrate much further in to the up-down channel, but the left-right channel is more slowly varying. This should and does account for much smoother domain wall motion between the left and right nanowire sections across the Hall cross. The intention with this situation was to display a range of methods for computationally modelling an experimental system and showing what effects all of the approximations that are routinely made in the literature can dictate what happens in a simulation.

Other effects that could have influenced the pinning in the nanowire but aren't presented in this thesis were surface roughness and anisotropy disorder and or anisotropy patterning. Thiaville's work was the first to attempt to include surface roughness and led to the verification of the critical current density due to pinning [91, 193]. Large scale surface roughness with good variation is more well-suited to FEM solvers in order to get the resolution high enough to model the surface. In FDM the surface is constrained by the cell size. Anisotropy disorder was included through the use of a random vector field modifying the anisotropy by a random number about a desired value. This would be interesting further work, as systems modelled by OOMMF are generally extremely clean and don't mimic experiment. Further work in to discovering the accuracy of micromagnetic simulations would benefit greatly by including experimental properties to help identify where the inconsistency is. Anisotropy steps caused by ion bombardment in order to artificially produce pinning and or nucleation sites would be straightforward to model.

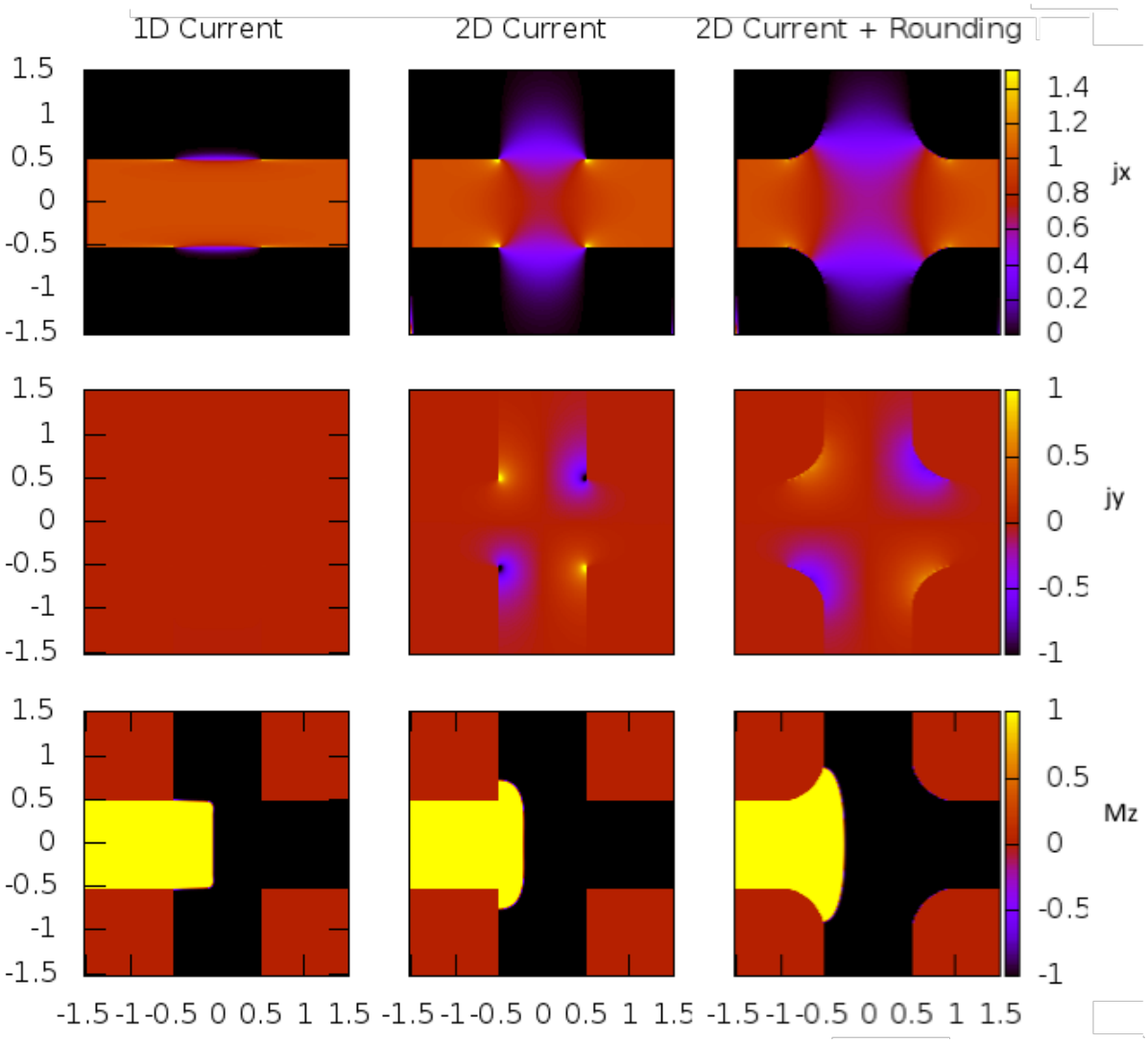


Figure 5-9: Current density and magnetisation for the cobalt layer in a Hall bar geometry with straight and rounded edges. Summary figure run with the material parameters discussed in this chapter for sample cobalt platinum systems.

## 5.5 EHE Measurements with CDDWM in Co/Pt Trilayers

### 5.5.1 Introduction

The extraordinary, or anomalous Hall effect is the contribution to the Hall effect that dominates in ferromagnets. In semiconductors the Hall effect is induced by an externally applied magnetic field, and in ferromagnets it is the magnetisation that causes it. The Hall resistivity for a general system can be written

$$\rho_{xy} = R_0 H_z + R_s M_z \,, \tag{5.14}$$

where $R_s$ is a function of the normal longitudinal resistivity. Consider that the anisotropic magnetoresistance is neglected, and there is zero applied magnetic field. Then, in the simplest regime the Hall resistivity will be directly proportional to the out-of-plane magnetisation.

In terms of the origin of EHE there are three broad regimes which have been identified from experiments, although the definitive proof is not available at the time of publication [131]. The regimes comprise a bad-metal, high conductivity, and a scattering dependent regime. Crystalline metallic cobalt would certainly fall in to the high conductivity regime from a simplistic point-of-view, but it is unclear how good a conductor the experimentally produced systems will be, and could therefore sit near the high conductivity border.

The EHE is used to measure the change in magnetisation of a region by experimentalists. From the above qualitative discussion a reasonable assumption can be made than in the absence of applied magnetic fields then the Hall resistivity will be directly proportional to the magnetisation. Using a micromagnetic solver such

as OOMMF it should be possible to invert the problem: plot EHE signals from modelling domain wall dynamics.

### 5.5.2 Summary and Discussion

Dynamical simulations were performed of Hall Crosses in the micromagnetic regime. It was shown that the shape of the domain wall passing through the Hall cross region is affected by the shape of the Hall cross. Current density calculations were performed to evaluate the effect that the Hall geometry has on a spin polarised current.

Figure 5-10 shows how the impact of the one dimensional implementation and two dimensional implementation of the spin transfer torque in the OOMMF package. The 1D current moves almost as if no Hall bar is present, an idea suggested in figure 5-4 earlier in the section. Although there are other systemic insights that would need to be evaluated in order to understand the EHE signal completely, the shape of the received EHE signal, might lead in to an idea of whether or not the spin current is transferring in to the Hall probe region. The further work could involve systematic calculations to provide profiles for all roundedness, and also the effect of surface roughness and micromagnetic parameter disorder, in order to better model the more natural systems use din experiment.

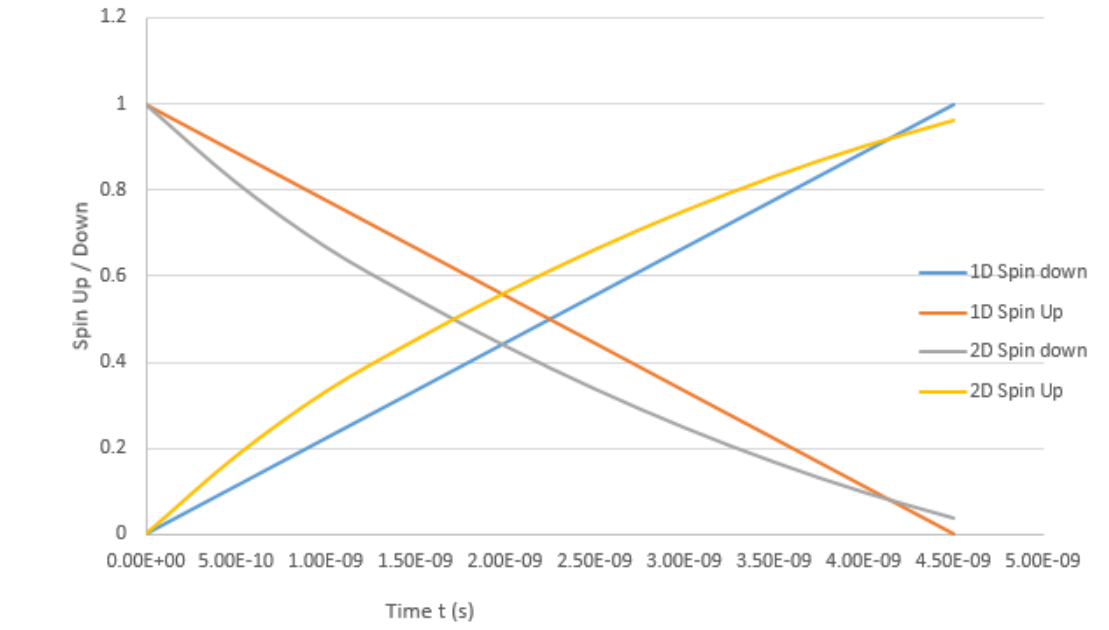


Figure 5-10: Plots showing the magnetisation reversal within the central Hall cross region that has been taken to be directly proportional to the EHE signal. Within the plot both 1D and 2D representations of the movement of the magnetic domains with applied current.

# Chapter 6

# Conclusions

Investigations in to different yet related fields of physics have been undertaken in this thesis. The common link is magnetism. The motivation was to model and understand materials which could be used as a new type of computer memory. This type of memory uses the position and polarity of magnetic domains to store information. Moving the domains and understanding where these domains will form, why they will form, how they will move are thus all important questions. Chapter 2 laid the foundation of a solid state understanding on magnetism, drawing information from quantum mechanics and classical physics and presenting micromagnetics. Chapter 3 transferred the problem in to the realm of condensed matter physics, attempting to understand the properties of magnetic systems from their electronic structure. Chapter 4 applied these concept to the cobalt platinum multilayers in particular that exhibit the high perpendicular uniaxial magnetic anisotropy. Finally, chapter 5 performed longer length scale modelling in systems approximating those used in experiments. This chapter-by-chapter short summary highlights the multi-scale modelling approach that was undertaken in this thesis and that is becoming increasingly popular.

The choice of magnetic material to investigate - cobalt platinum multilayers - was made because of its interesting magnetic properties [37]. Thin layers of cobalt have in-plane magnetisation. When sandwiched by platinum in the multilayer structure, the interaction of the platinum atoms with the cobalt causes a perpendicular anisotropy. If the cobalt layers are sufficiently thin, then this interfacial anisotropy dominates the crystalline anisotropy. Investigations are performed using density functional theory to understand the anisotropy energy origin. Table 4.6 demonstrates the anisotropy constants found for cobalt, cobalt platinum alloys, and multilayer structures. The easy axis in the thin film of cobalt is verified to be intraplanar, with the anisotropy switching to extraplanar upon the application of platinum surfaces.

Further work in this area might be regarding an interesting simulation that froze the system outside of equilibrium, and attempted to model the rearrangement of the spin orbit coupling dominated anisotropy change with the proximity of the platinum layers to the cobalt layers. In the simulations in this thesis, it was assumed that monatomic and diatomic cobalt layers would relax to match the in-plane lattice constant of the surrounding platinum atoms. The experimental systems are deposited at high speeds for finite amounts of time in the hope that an even coverage of cobalt would occur on the platinum substrate. The roughness and assumed polycrystallinity were not modelled in chapter 4, and could possibly be a cause of the systematic error between the DFT model and expected values. It is all too easy to blame any deficiencies in the DFT framework upon the poor implementation of the exchange-correlation potential that is estimated in most DFT models to date. The obtained material parameters for the simple cobalt platinum systems shown in table 4.6 are in reasonable accordance with the experimentally measured values. However, performing measurements for the magnetocrystalline anisotropy were not as precise. The experimentally measure easy axis was however confirmed in all cases, with the anisotropy energies sometimes up to an order of magnitude different.

The simulated micromagnetic parameters that were possible to directly compare shown in table 4.6 were not used in the final chapter toy system. This is because

the magnetocrystalline anisotropy was estimated as an order of magnitude larger than expected. This either systemic or modelling error would lead to extremely hard magnetic domains with extremely high switching fields and or threshold currents. The saturation magnetisation was similar to the bulk value and is most important in controlling the magnitude of the demagnetising field interaction. The micromagnetic constituents described within the LLG in 5.4 such as Walker breakdown field in a perfect nanowire linearly depends on the saturation magnetisation, whereas the shape anisotropy approximation depends on its square.

From electronic structure calculations in chapter 4 an enhancement in the local saturation magnetisation was predicted due to the breaking of symmetry and lack of direct exchange that could occur between the cobalt and much higher quantum number platinum electrons. This was expected as the bulk value of isolated cobalt magnetisation is closer to $2 \times 10^6 Am^{-1}$ whereas the bulk value and monolayer values are $1.6 \times 10^6 Am^{-1}$ and $1.8 \times 10^6 Am^{-1}$ respectively. This enhancement of approximately 10 percent is highly localised, as the induced magnetic moment on the platinum atoms was at most 15 percent of the bulk cobalt value. The exchange parameter was not modelled from first principles due to the difficulty in finding an accurate implementation within the density functional framework that was being utilised.

The phenomenological micromagnetic damping parameter was found to be an order of magnitude smaller than expected, as shown in table 4.6. The possible reason given for this was that the exchange correlation effects in DFT are not properly modelled. Another identified cause could be that the experimental system does not match the simulated version: due to the breaking of symmetry and lack of direct exchange that could occur between the cobalt and much higher quantum number platinum electrons. However, the test cases against the "pure" metals were also abject, implying that there is possibly a systemic issue in the model, or that another contribution has not been identified. Therefore, more work is required in this field, as it doesn't appear to have been solved in this area. Due to the discrepancies in the simulated micromagnetic parameters and the experimentally measured values, this thesis could no longer justify the parametrisation of a whole

host of micromagnetic simulations. The author redirects the reader to the whole host of exciting micromagnetic simulations of phenomena in the literature.

The effect of a Hall cross on the motion of a domain wall was studied. This was original work and involved simulating the effect a Hall geometry has on an applied current, and then using these values to parametrise a micromagnetic simulation. Initial investigations were aimed at understanding the effect of the actual Hall cross geometry on the domain wall motion. It was found that in the first instance and OOMMF implementation there was little or no effect on the transit of the domain wall by the Hall cross, as shown in figure 5-4. This was predicted to be unphysical, and further investigation yielded the realisation that OOMMF was not interested in any other components that were x-related for the motion.

To solve the deficiency of only being able to model 1D current flows, classical electrodynamics was implemented in order to estimate the 2D spin polarised current density in the Hall cross. This was then used to parametrise an extended spin torque evolver in OOMMF that could now parse vector field values for current densities. These investigations showed double concentrations of current near the corners which led to undesired effects (figure 5-7) - a domain could unpin quickly but struggled to repin. This may have been resolved by attempting to create a feedback loop within the systems to account for the anisotropic magnetoresistance between the current and the wall. A simpler approach involved introducing some small experimental rounding, as it was imagined that a beam would have produced the Hall bar geometry, and thus the join would most probably not be abrupt. This simple change smoothed out the current densities and provided a different transit profile for the domain wall. The rounded edges distinctly spread out the extreme current densities leading to much more natural domain wall profiles. Analyses showed that the extraordinary Hall effect was directly proportional to the out of plane magnetisation, and thus a qualitative comparison could be made with any experimental work that follows. The application of racetrack memory is still an exciting prospect, but one which this work only hints at elucidating.

It is envisaged that the plethora of micromagnetic modelling will be able to guide

experimentalists, and when working in collaboration exhibit consistent results. The EHE method for determining the transit of a domain wall is problematic, and received signal are noisy and most likely greatly affected by the rough polycrystalline material and arbitrary pinning sites. Future computational efforts could be put forward in order to create a list of schematics of domain wall transit profiles. Certain points of curvature or discontinuities in the experimental profile could be matched to a theoretical calculation. Ideally, future work would involve performing time-of-flight measurements on the domain wall in collaboration with experimental groups, in order to understand the principles of domain wall motion and pinning in racetrack memory.

# Bibliography


[1] L. Berger. Exchange interaction between ferromagnetic domain wall and electric current in very thin metallic films. *Journal of Applied Physics*, 55(6):1954–1956, 1984.

[2] L. Berger. Low-field magnetoresistance and domain drag in ferromagnets. *Journal of Applied Physics*, 49(3):2156–2161, 1978.

[3] L. Berger. Dragging of domains by an electric current in very pure, non-compensated, ferromagnetic metals. *Physics Letters A*, 46(1):3 – 4, 1973.

[4] A. Aziz, S. J. Bending, H. Roberts, S. Crampin, P. J. Heard, and C. H. Marrows. Artificial domain structures realized by local gallium focused ion-beam modification of pt/co/pt trilayer transport structure. *Journal of Applied Physics*, 98(12):124102, 2005.

[5] A. Aziz, S. J. Bending, H. G. Roberts, S. Crampin, P. J. Heard, and C. H. Marrows. Angular dependence of domain wall resistivity in artificial magnetic domain structures. *Phys. Rev. Lett.*, 97(20):206602, Nov 2006.

[6] Stuart S. P. Parkin, Masamitsu Hayashi, and Luc Thomas. Magnetic domain-wall racetrack memory. *Science*, 320(5873):190–194, 2008.

[7] Gen Tatara, Toshihiko Takayama, Hiroshi Kohno, Junya Shibata, Yoshinobu Nakatani, and Hidetoshi Fukuyama. Threshold current of domain wall motion under extrinsic pinning, $\beta$-term and non-adiabaticity. *Journal of the Physical Society of Japan*, 75(6):064708, 2006.

[8] A. Thiaville, Y. Nakatani, J. Miltat, and N. Vernier. Domain wall motion by spin-polarized current: a micromagnetic study. *Journal of Applied Physics*, 95(11):7049–7051, 2004.

[9] BBC. Ibm scientists unveil racetrack memory chip prototype.

[10] R. Heap and S. Greaves. The magnetic structure of platinum-cobalt multilayers. *J. Phys. D: Appl. Phys.*, 27, 1994.

[11] G. Hadjipanayis and P. Gaunt. An electron microscope study of the structure and morphology of a magnetically hard ptco alloy. *Journal of Applied Physics*, 50:2358, 1979.

[12] C.-J. Lin, G.L. Gorman, C.H. Lee, R.F.C. Farrow, E.E. Marinero, H.V. Do, H. Notarys, and C.J. Chien. Magnetic and structural properties of co/pt multilayers. *Journal of Magnetism and Magnetic Materials*, 93:194 – 206, 1991.

[13] D. Weller, H. Brandle, and C. Chappert. Magnetic and magneto-optical properties of cobalt-platinum alloys with perpendicular magnetic anisotropy. *Journal of Magnetism and Magnetic Materials*, 61:1600, 1994.

[14] D. Weller, H. Brandle, G. Gorman, C.-J Lin, and H.Notarys. Magnetic and magneto-optical properties of cobalt-platinum alloys with perpendicular magnetic anisotropy. *Applied Physics Letters*, 61:1600, 1992.

[15] C Haas A Kootte and R A de Groot. The electronic structure of ordered binary co-pt compounds. *Journal of Physics: Condensed Matter*, 3 : 9:1113, 1991.

[16] L. Alvarez, K.-Y Wang, S. Landi, S. Bending, and C. Marrows. Spin-transfer torque acceleration of domain walls in a co/pt multilayer wire. *Preprint*, 2009.

[17] H. Berg and J. B. Cohen. Long-range order and ordering kinetics in copt3. *Metallurgical and Materials Transactions B*, 3:1797–1805, 1972.

[18] P. F. Carcia. Perpendicular magnetic anisotropy in pd/co and pt/co thin-film layered structures. *Journal of Applied Physics*, 63(10):5066–5073, 1988.

[19] G. S. Chang, Y. P. Lee, J. Y. Rhee, J. Lee, K. Jeong, and C. N. Whang. Realization of a large magnetic moment in the ferromagnetic copt bulk phase. *Phys. Rev. Lett.*, 87(6):067208, Jul 2001.

[20] G. H. O. Daalderop, P. J. Kelly, and M. F. H. Schuurmans. First-principles calculation of the magnetic anisotropy energy of $(\mathrm{co})n/(\mathrm{x})m$ multilayers. *Phys. Rev. B*, 42(11):7270–7273, Oct 1990.

[21] Keith Gilmore, Y. U. Idzera, and M. D. Stiles. Identification of the dominant precession-damping mechanism in fe, co, ni by first-principles calculations. *Phys. Rev. Lett.*, 99:027204, 2007.

[22] Keith Gilmore, M. D. Stiles, Jonas Seib, Daniel Steiauf, and Manfred Fähnle. Anisotropic damping of the magnetization dynamics in ni, co, and fe. *Phys.*

*Rev. B*, 81:174414, May 2010.

[23] Arti Kashyap, K. B. Garg, A. K. Solanki, T. Nautiyal, and S. Auluck. Electronic structure, fermi surface, and curie temperature calculations for the co-pt system. *Phys. Rev. B*, 60(4):2262–2267, Jul 1999.

[24] E. T. Kulatov, Yu. A. Uspenskii, and S. V. Halilov. Spin, orbital moments and magneto-optical properties of mpt3 (m = cr, mn, fe, co) compounds. *Journal of Magnetism and Magnetic Materials*, 163(3):331 – 338, 1996.

[25] Kentaro Kyuno, Ryoichi Yamamoto, and Setsuro Asano. Theoretical study on the magnetocrystalline anisotropy of x/co
(x=pd, pt, cu, ag, au) multilayers. *Journal of the Physical Society of Japan*, 61(6):2099–2103, 1992.

[26] B. Van Laar. The magnetic structure of copt. *J. Phys. France*, 25:600–603, 1964.

[27] R. J. Lange, S. J. Lee, D. W. Lynch, P. C. Canfield, B. N. Harmon, and S. Zollner. Ellipsometric and kerr-effect studies of $pt3-x$ $(x = mn, co)$. *Phys. Rev. B*, 58(1):351–358, Jul 1998.

[28] B. Lazarovits, L. Szunyogh, and P. Weinberger. Magnetic properties of finite co chains on pt(111). *Phys. Rev. B*, 67:024415, Jan 2003.

[29] W.W. Lin and H. Sang. A novel temperature-induced magnetization transition in pt/co/pt sandwiches. eprint arXiv:0812.2512, 2008.

[30] J.M. Maclaren. First principle calculations of fept, copt, co3pt and fe3pt alloys. In *Magnetics Conference, 2005. INTERMAG Asia 2005. Digests of the IEEE International*, pages 1913–1914, April 2005.

[31] Alexander B. Shick and Oleg N. Mryasov. Coulomb correlations and magnetic anisotropy in ordered $l1$ copt and fept alloys. *Phys. Rev. B*, 67(17):172407, May 2003.

[32] D. Weller, H. Brändle, G. Gorman, C.-J. Lin, and H. Notarys. Magnetic and magneto-optical properties of cobalt-platinum alloys with perpendicular magnetic anisotropy. *Applied Physics Letters*, 61(22):2726–2728, 1992.

[33] S. D. Willoughby, R. A. Stern, R. Duplessis, J. M. MacLaren, M. E. McHenry, and D. E. Laughlin. Electronic structure calculations of hexagonal and cubic phases of co[sub 3]pt. *Journal of Applied Physics*, 93(10):7145–7147, 2003.

[34] C. C. Yu, Y. C. Chu, F. L. Chang, D. H. Wei, S. C. Chou, Y. Liou, Y. D. Yao, W. C. Cheng, and T. S. Chin. Structure and magnetic properties of co/pt single- and bi-crystal multilayers. *Journal of Magnetism and Magnetic*

*Materials*, 282:65 – 68, 2004. International Symposium on Advanced Magnetic Technologies.

[35] Charles Kittel. *Introduction To Solid State Physics*. Wiley, 1996.

[36] S. S. A. Razee, J. B. Staunton, and F. J. Pinski. First-principles theory of magnetocrystalline anisotropy of disordered alloys: Application to cobalt platinum. *Phys. Rev. B*, 56:8082–8090, Oct 1997.

[37] A Aziz, SJ Bending, H Roberts, S Crampin, PJ Heard, and CH Marrows. Investigation of artificial domains realized by local gallium focused ion-beam modification of Pt/Co/Pt trilayer structures. *JOURNAL OF APPLIED PHYSICS*, 99(8), APR 15 2006. ref 29 proposal.

[38] C. Vieu, J. Gierak, H. Launois, T. Aign, P. Meyer, J. P. Jamet, J. Ferré, C. Chappert, T. Devolder, V. Mathet, and H. Bernas. Modifications of magnetic properties of pt/co/pt thin layers by focused gallium ion beam irradiation. *Journal of Applied Physics*, 91(5):3103–3110, 2002.

[39] L. Berger. Emission of spin waves by a magnetic multilayer traversed by a current. *Phys. Rev. B*, 54(13):9353–9358, Oct 1996.

[40] L. Berger. Exchange interaction between electric current and magnetic domain wall containing bloch lines. *Journal of Applied Physics*, 63(5):1663–1669, 1988.

[41] L. Berger. Possible existence of a josephson effect in ferromagnets. *Phys. Rev. B*, 33(3):1572–1578, Feb 1986.

[42] B. D. Cullity. *Introduction to Magnetic Materials*. Addison-Wesley, Reading Massachusetts, 1972.

[43] W. Heisenberg. ?zur theorie des ferromagnetismus? (on the theory of ferromagnetism). *Zeitschrift für Physik A*, 49:619–636, 1928.

[44] J. C. Slater. The theory of ferromagnetism: lowest energy levels. *Physical Review*, 52:198–214, 1937.

[45] J. C. Slater. The ferromagnetism of nickel ii: temperature effects. *Physical Review*, 49:931–937, 1936.

[46] J. C. Slater. The ferromagnetism of nickel. *Physical Review*, 49:537–545, 1936.

[47] E.C. Stoner. Collective electron ferromagnetism ii: energy and specific heat. *Proceedings of the Royal Society London -Series A*, x(169):339–371, 1939.

[48] E.C. Stoner. Collective electron energy and specific heat. *Philosophical Magazine*, 25(171):899–926, 1938.

[49] E.C. Stoner. Collective electron ferromagnetism. *Proceedings of the Royal Society London -Series A*, x(165):372–414, 1938.

[50] J. Friedel, G. Leman, and S. Olszewski. Metals and alloys: on the nature of magnetic couplings in transitional metals. *Journal of Applied Physics*, 32:S325–S330, 1961.

[51] B. D. Cullity. *Introduction To Magnetic Materials*. Addison Wesley, 1972.

[52] P. Weiss. L?hypothèse du champ molèculaire et de la propriété ferromagnétique (the hypothesis of the molecular field and the property of ferromagnetism). *Journal de Physique et le Radium*, 6:1136–1139, 1907.

[53] P. Weiss. La variation du ferromagnétisme avec la temperature (the variation of ferromagnetism with temperature). *Comptes Rendus*, 143:1136–1139, 1906.

[54] Amikam Aharoni. *Introduction to the Theory of Ferromagnetism*. Clarendon Press, 1996.

[55] A. Hubert and R. Schafer. *Magnetic domains: the analysis of magnetic microstructures*. Springer-Verlag, Berlin, 2000.

[56] R.C. O'Handley. *Modern Magnetic Materials: Principles and Applications*. Wiley and Sons, New York, 2000.

[57] H. Barkhausen. Zwei mit hilfe der neuen verstärker entdeckte erscheinungen (two phenomena, discovered with the help of the new amplifiers). *Zeitschrift für Physik*, 20:401–403, 1919.

[58] K. J. Sixtus and L. Tonks. Propagation of large barkhausen discontinuities. *Physical Review*, 37:930–958, 1931.

[59] F. Bloch. Zur theorie des austauschproblems und der remanenzerscheinung der ferromagnetika (on the theory of the exchange problem and the remanence phenomenon of ferromagnets). *Zeitschrift für Physik*, 74:295–335, 1932.

[60] R. Becker. Elastische spannungen und magnetische eigenschaften (flexible tensions and magnetic characteristics). *Zeitschrift für Physik*, 33:905–913, 1932.

[61] K. Honda and S. Kaya. On the magnetisation of single crystals of iron. *Scientific Reports of Tohoku Imperial University*, 15:721–754, 1926.

[62] D.A. Allwood, G. Xiong, M. D. Cooke, and R. P. Cowburn. Magneto-optical kerr effect analysis of magnetic nanostructures. *Journal of Physics D: Applied Physics*, 36:2175 – 2182, 2003.

[63] M. Faraday. On the magnetisation of light and the illumination of magnetic lines of force. *Philosophical Transactions of the Royal Society (London)*, 136:1 – 20, 1846.

[64] T. Miyahara and M. Takahashi. The dependence of the longitudinal kerr magnetooptic effect on saturation magnetisation in nife films. *Japanese Journal of Applied Physics*, 15:291 – 298, 1976.

[65] V N Antonov P M Oppeneer. Calculated magneto-optical kerr spectra of xpt3 compounds (x = v, cr, mn, fe and co). *Journal of Physics: Condensed Matter*, 8:5769 – 5780, 1996.

[66] S Blundell. *Magnetism in Condensed Matter*. Oxford University Press, 2001.

[67] W. Heisenberg. Zur theorie der magnetostriktion und der magnetisierungskurve (on the theory of magnetostriction and the magnetisation curve). *Zeitschrift fur Physik*, 69:287–297, 1931.

[68] Jr. W. F. Brown and A. E. LaBonte. Structure and energy of one-dimensional domain walls in ferromagnetic thin films. *Journal of Applied Physics*, 36(4):1380–1386, 1965.

[69] G. H. O. Daalderop. *Magnetic Anisotropy from First Principles*. PhD thesis, Philips Research Laboratories, 1991.

[70] R. J. Joenk. Second anisotropy constant in cubic ferromagnetic crystals. *Phys. Rev.*, 130:932–938, May 1963.

[71] Amikam Aharoni. Demagnetizing factors for rectangular ferromagnetic prisms. *Journal of Applied Physics*, 83(6):3432–3434, 1998.

[72] Alex Hubert and Rudolf Schafer. *Magnetic Domains*. Springer, 1998.

[73] A. Omari, K. and J. Hayward, T.˙ Chirality-based vortex domain-wall logic gates. *Phys. Rev. Applied*, 2:044001, Oct 2014.

[74] M.J. Donahue and D.G. Porter. Oommf user's guide, version 1.0. *National Institute of Standards and Technology*, 6376, 1999.

[75] N. L. Schryer and L. R. Walker. The motion of 180[degree] domain walls in uniform dc magnetic fields. *Journal of Applied Physics*, 45(12):5406–5421, 1974.

[76] G V Skrotskii. The landau-lifshitz equation revisited. *Soviet Physics Uspekhi*, 27:977, 1984.

[77] T.L. Gilbert. A phenomenological theory of damping in ferromagnetic mate-

rials. *Magnetics, IEEE Transactions on*, 40(6):3443 – 3449, nov. 2004.

[78] J. S. Parker, S. M. Watts, P. G. Ivanov, and P. Xiong. Spin polarization of *cro*2 at and across an artificial barrier. *Phys. Rev. Lett.*, 88(19):196601, Apr 2002.

[79] C. H. Marrows. Spin-polarised currents and magnetic domain walls. *Advances in Physics*, 54(8):585–713, 2005.

[80] E. B. Myers, D. C. Ralph, J. A. Katine, R. N. Louie, and R. A. Buhrman. Current-Induced Switching of Domains in Magnetic Multilayer Devices. *Science*, 285(5429):867–870, 1999.

[81] J. C. Slonczewski. Current-driven excitation of magnetic multilayers. *Journal of Magnetism and Magnetic Materials*, 159(1-2):L1 – L7, 1996.

[82] J. C. Slonczewski. Currents and torques in metallic magnetic multilayers. *Journal of Magnetism and Magnetic Materials*, 247(3):324 – 338, 2002.

[83] Z. Li and S. Zhang. Domain-wall dynamics driven by adiabatic spin-transfer torques. *Phys. Rev. B*, 70(2):024417, Jul 2004.

[84] J. Grollier, P. Boulenc, V. Cros, A. Hamzić, A. Vaurès, A. Fert, and G. Faini. Switching a spin valve back and forth by current-induced domain wall motion. *Applied Physics Letters*, 83(3):509–511, 2003.

[85] Z. Li, J. He, and S. Zhang. Effects of spin current on ferromagnets (invited). In *Handbook of Spin Transport and Magnetism*, volume 99, page 08Q702. AIP, 2006.

[86] A. Thiaville, Y. Nakatani, J. Miltat, and Y. Suzuki. Micromagnetic understanding of current-driven domain wall motion in patterned nanowires. *Europhysics Letters*, 69:990, 2005.

[87] M. Kläui, C. A. F. Vaz, J. A. C. Bland, W. Wernsdorfer, G. Faini, E. Cambril, L. J. Heyderman, F. Nolting, and U. Rüdiger. Controlled and reproducible domain wall displacement by current pulses injected into ferromagnetic ring structures. *Phys. Rev. Lett.*, 94(10):106601, Mar 2005.

[88] N. Vernier, D. A. Allwood, D. Atkinson, M. D. Cooke, and R. P. Cowburn. Domain wall propagation in magnetic nanowires by spin-polarized current injection. *Europhys. Lett.*, 65(4):526–532, 2004.

[89] A. Yamaguchi, S. Nasu, H. Tanigawa, T. Ono, K. Miyake, K. Mibu, and T. Shinjo. Effect of joule heating in current-driven domain wall motion. *Applied Physics Letters*, 86(1):012511, 2005.

[90] W. Doring. (inertial mass of a domain wall). *Z. Naturf*, 3:373, 1948.

[91] Y. Nakatani, A. Thiaville, and J. Miltat. Faster magnetic walls in rough wires. *Nature Materials*, 2:521 – 523, 2003.

[92] M. Born and R. Oppenheimer. Zur quantentheorie der molekeln. *Annalen der Physiks*, 389:457, 1927.

[93] V. Fock. Naherungsmethode zur losung des quantenmechanischen mehrkörperproblems. *Z. Phys. A.L Hadrons Nucl.*, 61:126, 1930.

[94] D. R. Hartree. The wave mechanics of an atom with a non-coulmob central field. i. theory and methods. *Proceding Cambidge Philosophy*, 24:89, 1928.

[95] Richard Martin. *Electronic Structure*. Cambridge, 2004.

[96] P. Hohenberg and W. Kohn. Inhomogeneous electron gas. *Phys. Rev.*, 136(3B):B864–B871, Nov 1964.

[97] W. Kohn and L. J. Sham. Self-consistent equations including exchange and correlation effects. *Phys. Rev.*, 140(4A):A1133–A1138, Nov 1965.

[98] U von Barth and L Hedin. A local exchange-correlation potential for the spin polarized case. *Solid State Physics*, 5:1629, 1972.

[99] Edmund C. Stoner. The analysis of magnetization curves. *Rev. Mod. Phys.*, 25(1):2, Jan 1953.

[100] John P. Perdew, Kieron Burke, and Matthias Ernzerhof. Generalized gradient approximation made simple. *Phys. Rev. Lett.*, 77(18):3865–3868, Oct 1996.

[101] N. F. Mott. The electrical conductivity of transition metals. *Proceedings of the Royal Society*, 153(6):699 – 717, 1936.

[102] E. Engel and R. Dreizler. Relativistic density functional theory. *Topic in Current Chemistry*, 181: Density Functional Theory II:1, 2996.

[103] V.I. Anisimov, J. Zaanen, and O.K. Andersen. Band theory and mott insulators. *Phys. Rev. B*, 44:943, 2005.

[104] M. Richter. *Density Functional Theory applied to 4f and 5f elements and Metallic Compounds*, volume 13. Elsevier, 2001.

[105] O.K. Andersen. Simple approach to the band-structure problem. *Solid State*, 13:133, 1973.

[106] O. K. Andersen. Linear methods in band theory. *Phys. Rev. B*, 30:3060, 1975.

[107] J. Korringa. On the calculation of the energy of a bloch wave in a metal.

*Phsyica*, 13:392, 1947.

[108] N. Kohn and W. Rostoker. Solution of the schrodinger equation in periodic llattice with an application to metallic lithium. *Phys. Rev.*, 94:1111, 1954.

[109] A. R. Williams, J. Kubler, and C.D. Gelatt. Cohesive properties of metallic compounds: Augmented-spherical wave calculations. *Phys. Rev. B*, 19:6094, 1979.

[110] A Messiah. *Quantum mechanics. Vol. 1.* Amsterdam ; Oxford : North-Holland, 1991.

[111] J. P. Perdew and Alex Zunger. Self-interaction correction to density-functional approximations for many-electron systems. *Phys. Rev. B*, 23(10):5048–5079, May 1981.

[112] P. A. M. Dirac. The quantum theory of the electron. *Proceedings of the Royal Society of London. Series A*, 117(778):610–624, 1928.

[113] A Messiah. *Quantum mechanics. Vol. 2.* Amsterdam ; Oxford : North-Holland, 1991.

[114] A H MacDonald and S H Vosko. A relativistic density functional formalism. *Journal of Physics C: Solid State Physics*, 12(15):2977, 1979.

[115] A. K. Rajagopal. Inhomogeneous relativistic electron gas. *Journal of Physics C: Solid State Physics*, 11(24):L943, 1978.

[116] A. K. Rajagopal and J.Callaway. Inhomogeneous electron gas. *Phys. Rev. B*, 7(5):1912, 1973@articlePhysRevB.77.165107, title = Hybrid exchange-correlation functional for accurate prediction of the electronic and structural properties of ferroelectric oxides, author = Bilc, D. I. and Orlando, R. and Shaltaf, R. and Rignanese, G.-M. and Íñiguez, Jorge and Ghosez, Ph., journal = Phys. Rev. B, volume = 77, issue = 16, pages = 165107, numpages = 13, year = 2008, month = Apr, publisher = American Physical Society, doi = 10.1103/PhysRevB.77.165107, url = http://link.aps.org/doi/10.1103/PhysRevB.77.165107 .

[117] P. Strange. *Relativistic Quantum Mechanics.* Cambridge University Press, Cambridge, 1998.

[118] http://www.castep.org/.

[119] http://www.castep.org/castep/mailinglist.

[120] R. M. Martin. *Electronic Stucture: Basic Theory and Practical Methods.* Cambridge University Press, Cambridge, 2004.

[121] Chris J Pickard and RJ Needs. Ab initio random structure searching. *Journal of Physics: Condensed Matter*, 23(5):053201, 2011.

[122] D Singh. *Planewaves, Pseudopotentials, and the LAPW Method*. Cambridge University Press, Cambridge, 2nd edition, 2006.

[123] J. C. Slater. Wave functions in a periodic potential. *Phys. Rev.*, 51(10):846–851, May 1937.

[124] L. Petit, Z. Szotek, M. Lueders, W. M. Temmerman, and A. Svane. First-principles study of valence and structural transitions in euo under pressure. *Phys. Rev. B*, 90:035110, Jul 2014.

[125] Guntram Fischer, Markus Däne, Arthur Ernst, Patrick Bruno, Martin Lüders, Zdzislawa Szotek, Walter Temmerman, and Wolfram Hergert. Exchange coupling in transition metal monoxides: Electronic structure calculations. *Phys. Rev. B*, 80:014408, Jul 2009.

[126] M. J. Donahue and R. D McMichael. Exchange energy representations in computational micromagnetics. *Physica B*, 233:272 – 278, 1997.

[127] F. Garcia-Sanchez, O. Chubykalo-Fesenko, O. Mryasov, R. W. Chantrell, and K. Yu. Guslienko. Exchange spring structures and coercivity reduction in fept/ferh bilayers: A comparison of multiscale and micromagnetic calculations. *Applied Physics Letters*, 87(12):122501, 2005.

[128] G. H. O. Daalderop, P. J. Kelly, and M. F. H. Schuurmans. First-principles calculation of the magnetocrystalline anisotropy energy of iron, cobalt, and nickel. *Phys. Rev. B*, 41(17):11919–11937, Jun 1990.

[129] M. Asato, A. Settels, T. Hoshino, T. Asada, S. Blügel, R. Zeller, and P. H. Dederichs. Full-potential kkr calculations for metals and semiconductors. *Phys. Rev. B*, 60(8):5202–5210, Aug 1999.

[130] C. Chappert and P. Bruno. Magnetic anisotropy in metallic ultrathin films and related experiments on cobalt films (invited). *Journal of Applied Physics*, 64(10):5736–5741, 1988.

[131] V. Korenman and R. E. Prange. Anomalous damping of spin waves in magnetic metals. *Phys. Rev. B*, 6(7):2769–2777, Oct 1972.

[132] M. D. Stiles, S. V. Halilov, R. A. Hyman, and A. Zangwill. Spin-other-orbit interaction and magnetocrystalline anisotropy. *Phys. Rev. B*, 64:104430, Aug 2001.

[133] L. Neel. Le journal de physique et le radium. *Le Journal de Physique et le Radium*, 15:225, 1954.

[134] Harvey Brooks. Ferromagnetic anisotropy and the itinerant electron model. *Phys. Rev.*, 58:909–918, Nov 1940.

[135] H. Brooks. Ferromagnetic anisotropy and the itinerant electron model. *Phys. Rev.*, 58:909, 1940.

[136] A.J. Bennett and B.R. Cooper. Origin of the magnetic "surface anisotropy" of thin ferromagnetic films. *Phys. Rev. B.*, 3:1642, 1971.

[137] P. Strange, H. Ebert, J.B. Staunton, and B.L. Gyorffy. J. phys. condensed matter. *Phys. Rev. B*, 1:3947, 1989.

[138] J. G. Gay and Roy Richter. Spin anisotropy of ferromagnetic films. *Phys. Rev. Lett.*, 56(25):2728–2731, Jun 1986.

[139] P. Bruno. Tight-binding approach to the orbital magnetic moment and magnetocrystalline anisotropy of transition-metal monolayers. *Phys. Rev. B.*, 39:865, 1989.

[140] M. Jamet, W. Wernsdorfer, and C. Thirion. Magnetic anisotropy in single clusters. *Phys Rev. B.*, 69:024401, 2004.

[141] X. Batlle and A. Labarta. Finite-size effects in fine particles: magnetic and transport properties. *J. Phys. D: Appl. Phys.*, 35:R15, 2002.

[142] M.B. Stearns and H.P.J. Wijn. *3d, 4d, and 5d Elements, Alloys and Compounds*, volume 19 Part a. Springer, Berlin, 1986.

[143] Keith Gilmore, M. D. Stiles, Jonas Seib, Daniel Steiauf, and Manfred Fähnle. Anisotropic damping of the magnetization dynamics in ni, co, and fe. *Phys. Rev. B*, 81(17):174414, May 2010.

[144] J. Trygg, B. Johansson, O. Eriksson, and J.M. Wills. Total energy calculation of the magnetocrystalline anisotropy energy in the ferromagnetic metals. *Phys. Rev. Lett.*, 75:2871, 1995.

[145] S.V. Halilov, A.Y. Perlov, P.M. Oppeneer, A.N. Yaresko, and V.N. Antonov. Adiabatic spin dynamics from spin-density-functional theory: Application to fe, co, and ni. *Phys. Rev. B*, 57:9557, 1998.

[146] S.V. Beiden, W.M. Temmerman, Z. Szotek, G.A. Gehring, G.M. Stocks, Y. Wang, D.M.C. Nicholson, W.A. Shelton, and H. Ebert. Real-space approach to the calculation of magnetocrystalline anisotropy in metals. *Phys Rev. B*, 57:14247, 1998.

[147] G. Schneider and H.J.F. Jansen. Role of orbital polarization in calculations of the magnetic anisotropy. *J. Appl. Phys.*, 87:5875, 2000.

[148] V. Kambersky and C. E. Patton. Spin-wave relaxation and phenomenological damping in ferromagnetic resonance. *Phys. Rev. B*, 11(7):2668–2672, Apr 1975.

[149] V. Kamberský. On ferromagnetic resonance modelling damping in metals. *Czechoslovak Journal of Physics*, 26:1366, 1976.

[150] V. Kamberský. Spin-orbital gilbert damping in common magnetic materials. *Phys. Rev. B.*, 76:134416, 2007.

[151] J. Kunes and V. Kamberský. First-principles investigation of the damping of fast magnetization precession in ferromagnetic 3d metals. *Phys. Rev. B.*, 65:212411, 2002.

[152] S.M. Bhagat and P. Lubitz. Temperature variation of ferromagnetic relaxation in the transition metals. *Phys. Rev. B.*, 10:179, 1974.

[153] John P. Perdew, J. A. Chevary, S. H. Vosko, Koblar A. Jackson, Mark R. Pederson, D. J. Singh, and Carlos Fiolhais. Atoms, molecules, solids, and surfaces: Applications of the generalized gradient approximation for exchange and correlation. *Phys. Rev. B*, 46(11):6671–6687, Sep 1992.

[154] John P. Perdew. Density-functional approximation for the correlation energy of the inhomogeneous electron gas. *Phys. Rev. B*, 33(12):8822–8824, Jun 1986.

[155] Arti Kashyap, K. B. Garg, A. K. Solanki, T. Nautiyal, and S. Auluck. Electronic structure, fermi surface, and curie temperature calculations for the co-pt system. *Phys. Rev. B*, 60(4):2262–2267, Jul 1999.

[156] W.B. Pearson. *Lattice Spacings and Structure of Metals and Alloys*. Pergamon, Oxford, 1967.

[157] C Haas A Kootte and R A de Groot. The electronic structure of ordered binary co-pt compounds. *Journal of Physics: Condensed Matter*, 3 : 9:1113, 1991.

[158] V. N. Antonov, B. N. Harmon, and A. N. Yaresko. Electronic structure and x-ray magnetic circular dichroism in $cu3au$-type transition metal platinum alloys. *Phys. Rev. B*, 64(2):024402, Jun 2001.

[159] W. Grange, I. Galanakis, M. Alouani, M. Maret, J.-P. Kappler, and A. Rogalev. Experimental and theoretical x-ray magnetic-circular-dichroism study of the magnetic properties of $co50pt50$ thin films. *Phys. Rev. B*, 62(2):1157–1166, Jul 2000.

[160] R.W. Newman and J.J. Hren. The effect of crystal symmetry on field ion images of ordered alloys. *Surface Science*, 8(4):373 – 380, 1967.

[161] I. Galanakis, M. Alouani, and H. Dreyssé. Perpendicular magnetic anisotropy of binary alloys: A total-energy calculation. *Phys. Rev. B*, 62(10):6475–6484, Sep 2000.

[162] Y Ohta T Tohyama and M Shimizu. Tight-binding calculations of the electronic structure and magnetic properties in ordered tpt3 (t=ti, v, cr, mn, fe and co) alloys. *J. Phys.: Condens. Matter*, 1:1789 – 1798, 1987.

[163] B. Van Laar. The magnetic structure of copt. *J. Phys. France*, 25:600–603, 1964.

[164] F. Menzinger and A. Paoletti. Magnetic moments and unpaired-electron densities in co*pt*3. *Phys. Rev.*, 143(2):365–372, Mar 1966.

[165] R. J. Lange, S. J. Lee, D. W. Lynch, P. C. Canfield, B. N. Harmon, and S. Zollner. Ellipsometric and kerr-effect studies of $pt3 - x$ $(x = mn, co)$. *Phys. Rev. B*, 58(1):351–358, Jul 1998.

[166] V N Antonov P M Oppeneer. Calculated magneto-optical kerr spectra of xpt3 compounds (x = v, cr, mn, fe and co). *Journal of Physics: Condensed Matter*, 8:5769 – 5780, 1996.

[167] E. T. Kulatov, Yu. A. Uspenskii, and S. V. Halilov. Spin, orbital moments and magneto-optical properties of mpt3 (m = cr, mn, fe, co) compounds. *Journal of Magnetism and Magnetic Materials*, 163(3):331 – 338, 1996.

[168] H. Berg and J. B. Cohen. Long-range order and ordering kinetics in copt3. *Metallurgical and Materials Transactions B*, 3:1797–1805, 1972.

[169] Kenji Iwashita, Tamio Oguchi, and Takeo Jo. Orbital and spin magnetic moments of t*pt*3 (t=v, cr, mn, fe, and co). *Phys. Rev. B*, 54(2):1159–1162, Jul 1996.

[170] W. Kohn and N. Rostoker. Solution of the schrödinger equation in periodic lattices with an application to metallic lithium. *Phys. Rev.*, 94:1111–1120, Jun 1954.

[171] Fumiko Yonezawa and Kazuo Morigaki. Coherent potential approximation. basic concepts and applications. *Progress of Theoretical Physics Supplement*, 53:1–76, 1973.

[172] B. Velicky. Theory of electronic transport in disordered binary alloys: Coherent-potential approximation. *Phys. Rev.*, 184:614–627, Aug 1969.

[173] B. L. Gyorffy. Coherent-potential approximation for a nonoverlapping-muffin-tin-potential model of random substitutional alloys. *Phys. Rev. B*, 5:2382–2384, Mar 1972.

[174] N. D. Mermin and H. Wagner. Absence of ferromagnetism or antiferromagnetism in one- or two-dimensional isotropic heisenberg models. *Phys. Rev. Lett.*, 17:1133–1136, Nov 1966.

[175] S. Y. Zhou, G.-H. Gweon, A. V. Fedorov, P. N. First, W. A. de Heer, D.H. Lee, F. Guinea, A. H. Castro Neto, and A. Lanzara. Substrate-induced bandgap opening in epitaxial graphene. *Nature Materials*, 6:770–775, 2007.

[176] R. Miranda, D. Chandesris, and J. Lecante. Electronic structure of a cobalt monolayer on cu(100). *Surface Science*, 130(2):269 – 281, 1983.

[177] Felix O. Kannemann and Axel D. Becke. Van der waals interactions in density-functional theory: Rare-gas diatomics. *Journal of Chemical Theory and Computation*, 5(4):719–727, 2009.

[178] Ikutaro Hamada. van der waals density functional made accurate. *Phys. Rev. B*, 89:121103, Mar 2014.

[179] Jiri Klimes and Angelos Michaelides. Perspective: Advances and challenges in treating van der waals dispersion forces in density functional theory. *The Journal of Chemical Physics*, 137(12):–, 2012.

[180] Alde M., S. Mirbt, H. L. Skriver, N. M. Rosengaard, and B. Johansson. Surface magnetism in iron, cobalt, and nickel. *Phys. Rev. B*, 46(10):6303–6312, Sep 1992.

[181] D Kodderitzsch, S Mankovsky, and H Ebert. Ab initio calculation of the gilbert damping parameter via linear response formalism. *Magnetics, IEEE Transactions on*, 49(3):1041–1046, 2013.

[182] I. Barsukov, S. Mankovsky, A. Rubacheva, R. Meckenstock, D. Spoddig, J. Lindner, N. Melnichak, B. Krumme, S. I. Makarov, H. Wende, H. Ebert, and M. Farle. Magnetocrystalline anisotropy and gilbert damping in iron-rich fe 1-x si x thin films. *Phys. Rev. B*, 84:180405, Nov 2011.

[183] D Thonig and J Henk. Gilbert damping tensor within the breathing fermi surface model: anisotropy and non-locality. *New Journal of Physics*, 16(1):013032, 2014.

[184] http://magpar.net/.

[185] http://nmag.soton.ac.uk/.

[186] K.E. Atkinson. *An Introduction to Numerical Analysis*. Wiley, 1989.

[187] http://math.nist.gov.uk.

[188] Jr Brown, W. F. *Micromagnetics*. Interscience Publishers, New York, 1963.

[189] G. Finocchio, M. Carpentieri, B. Azzerboni, L. Torres, E. Martinez, and L. Lopez-Diaz. Micromagnetic simulations of nanosecond magnetization reversal processes in magnetic nanopillar. Number 8, page 08G522. AIP, 2006.

[190] D. Atkinson, D. S. Eastwood, and L. K. Bogart. Controlling domain wall pinning in planar nanowires by selecting domain wall type and its application in a memory concept. *Applied Physics Letters*, 92(2):022510, 2008.

[191] J.H. Franken, M Hoeigmakers, and R Lavrijsen. Domain-wall pinning by local control of anisotropy in pt/co/pt strips. *Journal of Physics: Condensed Matter*, 24:024216, 2012.

[192] M. Hayashi, L. Thomas, Ya. B. Bazaliy, C. Rettner, R. Moriya, X. Jiang, and S. S. P. Parkin. Influence of current on field-driven domain wall motion in permalloy nanowires from time resolved measurements of anisotropic magnetoresistance. *Phys. Rev. Lett.*, 96(19):197207, May 2006.

[193] A. Thiaville, J. M. García, and J. Miltat. Domain wall dynamics in nanowires. *Journal of Magnetism and Magnetic Materials*, 242-245(Part 2):1061 – 1063, 2002.